Influences of Tropical Deep Convection on Upper Tropospheric Humidity

A Thesis
Presented to
The Academic Faculty

by

Jonathon S. Wright

In Partial Fulfillment
of the Requirements for the Degree
Doctor of Philosophy

School of Earth and Atmospheric Sciences
Georgia Institute of Technology
August, 2006

Influences of Tropical Deep Convection on Upper Tropospheric Humidity

Approved by:

Professor Rong Fu, Adviser
School of Earth & Atmospheric Sciences
Georgia Institute of Technology

Professor Robert Dickinson
School of Earth & Atmospheric Sciences
Georgia Institute of Technology

Professor Athanasios Nenes
School of Earth & Atmospheric Sciences
School of Chemical & Biomolecular Engineering
Georgia Institute of Technology

Professor Andrew Dessler
Department of Atmospheric Sciences
Texas A&M University

Date Approved: July 3, 2006

ACKNOWLEDGEMENTS

I acknowledge the immeasurable contributions of Dr. Rong Fu to this study and to my graduate experience. I express appreciation for the Goddard Earth Science and Technology Center's Graduate Student Summer Program, which supported the work that grew into this study. I also thank Dr. Andy Dessler for serving as my mentor in the aforementioned program and for productive dialogue since. I thank Drs. Andy Heymsfield and Walt Petersen for provision of and useful discussions regarding relationships between radar reflectivity and ice water content, Drs. Annmarie Eldering, Ed Olsen, and Eric Fetzer for clarifying aspects of the AIRS data, and Dr. Mark Schoeberl for providing assistance with the trajectory model. Finally, I thank Drs. Robert Dickinson, Thanos Nenes, and Andy Dessler for agreeing to read this thesis. This work has been supported by a National Defense Science and Engineering Graduate Fellowship, a Georgia Institute of Technology President's Fellowship, the School of Earth and Atmospheric Sciences at the Georgia Institute of Technology, the NASA Global Energy and Water Cycle Program, and the NASA Terra and Aqua Project.

TABLE OF CONTENTS

LIST OF TABLES

LIST OF FIGURES

LIST OF SYMBOLS OR ABBREVIATIONS

AIRS	Atmospheric Infrared Sounder.
AMJ	April-June; boreal spring.
CO_2	carbon dioxide.
$e^{\#}$	saturation vapor pressure with respect to ice.
$\hat{\omega}$	intrinsic frequency.
hPa	hectoPascals, a unit of pressure.
ITCZ	intertropical convergence zone.
IWC	ice water content.
JAS	July-September; boreal summer.
JFM	January-March; austral summer.
MLS	Microwave Limb Sounder.
MODIS	Moderate Resolution Infrared Spectroradiometer.
NASA	National Aeronautics and Space Administration.
OLR	Outgoing Longwave Radiation.
OND	October-December; austral spring.
PDF	probability density function.
PR	Precipitation Radar.
PSD	particle size distribution.
$\mathbf{r}_{\mathrm{ei}}$	ice effective radius.
$\mathbf{RH}_{\mathrm{i}}$	relative humidity with respect to ice.
ρ	density of air.
T_{det}	temperature at the level of detrainment.
θ	potential temperature, an indicator of the internal potential energy of the atmosphere.
T_{low}	the coldest temperature along the trajectory between convection and the present position.
TRMM	Tropical Rainfall Measuring Mission.
UKMO	United Kingdom Meteorological Office.

UT upper troposphere.

UTH upper tropospheric humidity.

$w^{\#}$ saturation mass mixing ratio with respect to ice.

Z_e equivalent radar reflectivity factor [$\mathrm{mm}^6\ \mathrm{m}^{-3}$].

SUMMARY

The distribution of upper tropospheric humidity in the tropics and subtropics exerts a profound influence on the Earth's climate, and remains one of the largest sources of uncertainty in climate simulations. This uncertainty stems in large part from the relatively unknown factors that govern moist convective outflow into the tropical upper troposphere. This study examines the relative roles of detrainment temperature, convective ice water content, ice cloud effective radius, and ambient relative humidity in regulating the efficiency of convective moistening in the tropical upper troposphere. The spatial and temporal limits of these interactions are investigated for both continental and maritime convection between 15°S and 15°N using observational data from the Tropical Rainfall Measuring Mission, Terra, and Aqua satellite missions together with a sophisticated trajectory model.

In the global tropics, we find that cloud ice water content explains less than 1% of the downstream water vapor content variance within the initial twenty-four hours following convection. The influence of ice cloud effective radius is estimated to be less than 5%. Much of the influence of these two variables appears to be applied via dehydration, and the evidence suggests that influences on hydration are small. The amount of variance in the downstream water vapor explained by detrainment temperature varies from over 60% within the first 12 hours following convection, to about 20% after 24 hours of trajectory evolution. The correlation between water vapor content and coldest previous temperature along the trajectory accounts for 40-60% of water vapor variance when only the large-scale temperature distribution is considered, and is not significantly altered by the artificial imposition of small-scale temperature perturbations broadly consistent with convectively generated internal gravity waves. These relationships appear to be fairly robust regardless of season or convective source region. It remains unclear to what extent the uncertainties in the ice quantities used here contribute to the weakness of the observed relationship to water vapor.

Ambient relative humidity along the trajectory path is shown to be an important factor in determining the degree of moistening both in the vicinity and away from convection. Increases in water vapor mixing ratio are typically larger in areas with low ambient relative humidity, while convective detrainment tends to dehydrate regions of high ambient relative humidity. The limits of this interaction are estimated to be about 36 hours and 600 km removed from convection, when the amount of condensate remaining in the air has almost certainly dwindled to a small fraction of its initial value. Differences are identified between continental and maritime convective regimes, and this variability is traced to fundamental differences in their typical detrainment profiles.

Observations of water vapor from the Atmospheric Infrared Sounder are compared with the output of a simple advection-condensation model. The model and the observations are generally in good qualitative agreement, but the model is found to overpredict the occurrence of high humidities at all levels of detrainment. The sensitivity of this disagreement to a variety of possible dehydration mechanisms is investigated. The inclusion of ice properties, the choice of a more realistic condensation threshold, and improvements in the characterization of the temperature field are all judged to incrementally improve the agreement. The totality of these adjustments does not seem sufficient to explain the observed discrepancy.

CHAPTER I

INTRODUCTION

Water vapor is widely recognized as the dominant atmospheric greenhouse gas, due both to its continuum absorption over much of the infrared spectrum and its abundance relative to other greenhouse gases. As such, a clear understanding of the ways in which it feeds back to anthropogenic increases of other greenhouse gases is a vital prerequisite to accurate projections of future climate change. At present, however, this feedback remains one of the largest sources of uncertainty in climate models, resulting in wide variability within forecasts of future temperature change (*Held and Soden*, 2000; *Stocker et al.*, 2001).

The atmospheric greenhouse effect arises because the Earth's atmosphere is relatively translucent to incoming solar radiation, yet relatively opaque to outgoing thermal infrared radiation. This imbalance traps energy and increases temperature near the surface. Water vapor and clouds account for the bulk of the atmospheric greenhouse, along with contributions from various trace gases such as carbon dioxide (CO_2) and methane (*Moller*, 1963; *Manabe and Wetherald*, 1967; *Schneider*, 1972; *Warren and Thompson*, 1983; *Stephens and Greenwald*, 1990a,b). The radiative properties of water vapor are briefly summarized in Appendix A.

The theoretical basis regarding the water vapor feedback stems primarily from the increase in water vapor carrying capacity, or saturation mixing ratio, as temperature rises (the Clausius-Clapeyron relation). A simplified schematic of the process is shown in Figure 1. The burning of fossil fuels during the industrial age (smokestack) has led to increases in anthropogenic greenhouse gases such as CO_2 (black arrow) in the atmosphere. These increased greenhouse gases render the atmosphere more opaque (black dots) to outgoing longwave radiation (dark blue and green arrows). This raises the effective level of emission, and since energy in (yellow arrow) must equal energy out (dark blue arrow), temperatures

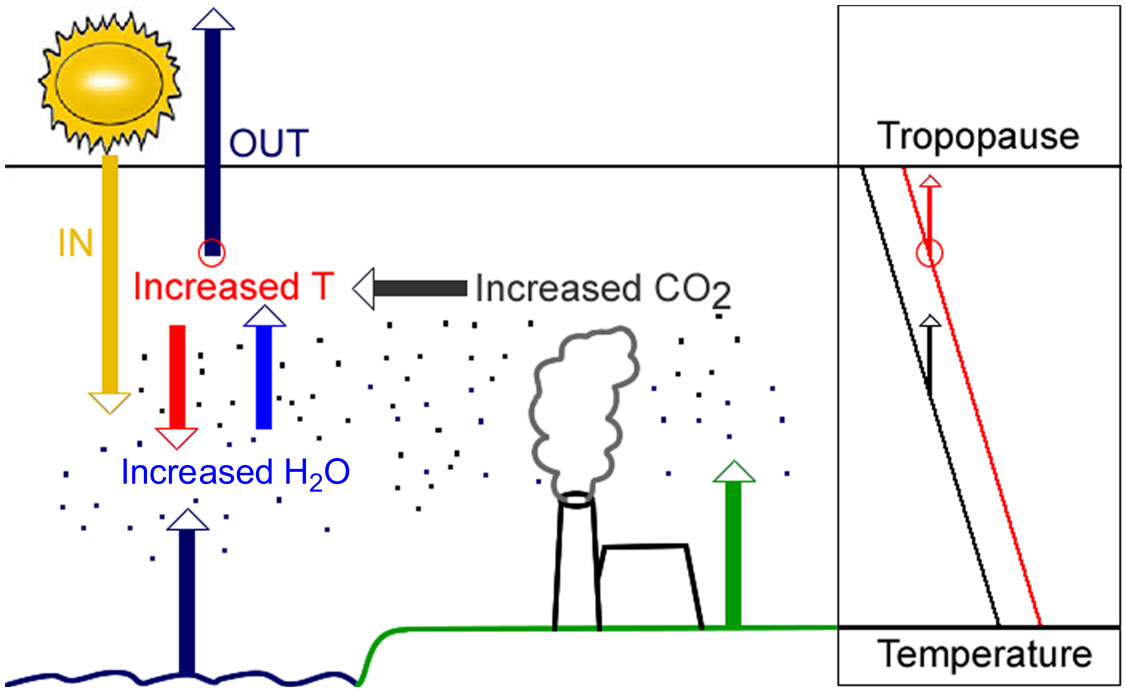

Figure 1: A schematic illustration of the water vapor feedback.

increase throughout the troposphere to compensate (right panel), This increase in temperature raises saturation mixing ratios (red arrow). Assuming that relative humidity remains approximately constant (*Moller*, 1963; *Manabe and Wetherald*, 1967), the temperature dependence of the Clausius Clapeyron relation implies that the water vapor content of the atmosphere will increase with temperature (light blue arrow). Since water vapor is itself a greenhouse gas, a further amplification of the warming results, potentially increasing water vapor, and so on.

There is of course no guarantee that the atmospheric water vapor content *will* increase simply because it *could*, and the constant relative humidity assumption is likewise controversial. As a result, the magnitude of the water vapor feedback remains a vigorous area of research. Estimates of its strength vary widely, from zero feedback (*Lindzen*, 1990), in which the radiative warming due to increased CO_2 is not further exacerbated by water vapor, to the constant relative humidity case discussed above, in which the estimated warming is about 1.6 times that due to CO_2 alone (*Held and Soden*, 2000). Most climate model simulations of the water vapor feedback find a result close to the constant relative

humidity case (*Stocker et al.*, 2001).

Climate models estimate that about 35% of the water vapor feedback is due to water vapor in the tropical upper troposphere (UT), with the remaining 65% spread across the extratropics, subtropics, and tropical troposphere below 500 mb (*Held and Soden*, 2000). Outgoing longwave radiation (OLR) in the tropics is frequently at a minimum in convectively active regions, and radiative transfer calculations indicate that about one third of this minimum is due solely to humidity (*Warren and Thompson*, 1983). Tropical OLR further exhibits the strongest sensitivity to fractional humidity changes between 300 mb and 200 mb, a condition that results from the contribution of a number of factors. First, the temperatures at these levels are quite cold, particularly in contrast to the surface—radiation absorbed and re-emitted at this level thus has a more drastic effect on OLR than that absorbed and re-emitted at lower levels in the atmosphere (*Pierrehumbert et al.*, 2006). Second, much of the outgoing energy in the tropics is carried above the portion of the troposphere that is most opaque to infrared by convection (*Lindzen*, 1990)—UT water vapor is in a unique position to trap this energy. Third, the low saturation mixing ratios that result from cold temperatures and the logarithmic dependence of the water vapor greenhouse parameter (Figure 45; or see, e.g., *Chou et al.*, 1993) mean that the water vapor absorption bands at this level are relatively unsaturated (*Shine and Sinha*, 1991; *Spencer and Braswell*, 1997; *Pierrehumbert et al.*, 2006)—in other words, a small increase in the total amount of water vapor would induce a relatively large decrease in OLR.

The general upper tropospheric humidity (UTH) distribution in the tropics can be understood as a balance between outflow from upward convective motion and large scale subsidence (e.g., *Sherwood*, 1996a). Deep convection constitutes the source, rapidly transporting moist near-surface air upward to the UT and above on highly localized spatial scales (*Betts*, 1990; *Danielsen*, 1993; *Holton et al.*, 1995; *Soden and Fu*, 1995; *Soden*, 2000). Dynamically and radiatively induced subsidence then returns the air to the boundary layer more slowly and over a larger area. Areas of high UTH tend to be collocated with areas of strong convective activity (e.g., *Chen et al.*, 1999; *Sassi et al.*, 2001; *Tian et al.*, 2004), and increased convection leads to increased UTH both within localized regions (e.g., *Chung*

et al., 2004) and when averaged over the whole of the tropics and subtropics (*Soden and Fu*, 1995).

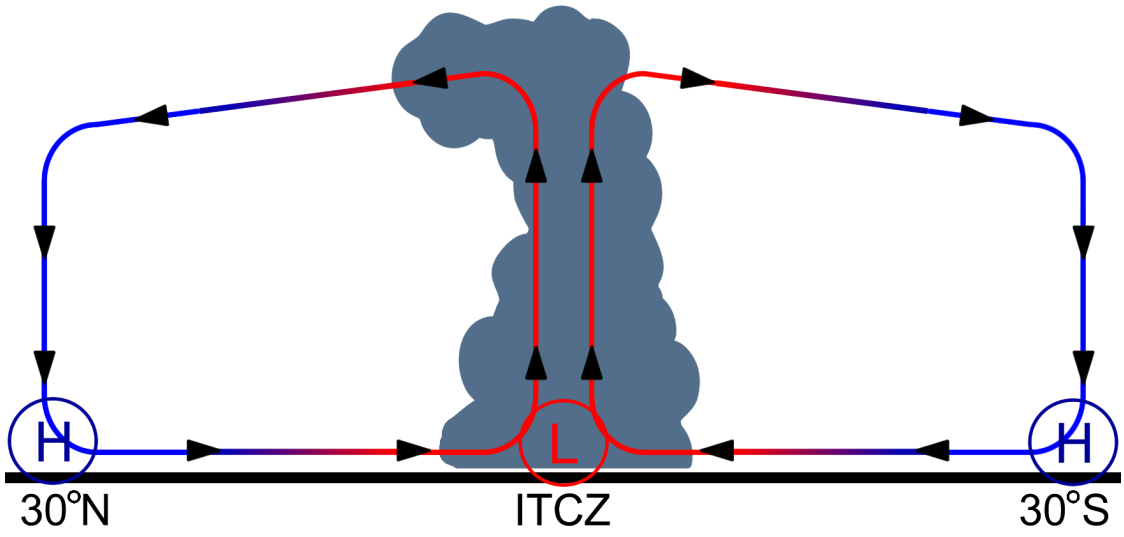

Figure 2: A schematic representation of the Hadley cell. Low and high surface pressures are marked with L and H, respectively, and differences in surface temperature are designated as warm (red) or cool (blue) by the color of the circulation path.

The horizontal distribution of convection in the tropics is generally arranged according to the rising branches of the Hadley (meridional) and Walker (zonal) circulations (*Riehl*, 1979). The Hadley cell (Figure 2) consists of two closed loops roughly symmetrical to the equator. Its circulation is characterized by rising motion in the intertropical convergence zone (ITCZ), poleward transport in the UT, sinking motion in the subtropics, and equatorward motion near the surface. The ITCZ is defined as the area where the tropical trade winds converge, located near the equator with a local minimum of surface pressure and maximum of surface temperature. Its meridional position migrates with the seasonal solar cycle, and is generally located slightly south of the equator in January and near 15°N in July (*Riehl*, 1979). Due to dense cloud cover, OLR is at a local minimum over the ITCZ. The Walker circulation describes the zonal distribution of tropical convection, and is generally characterized by rising motion over the continents and western Pacific warm pool, and sinking motion over most of the oceans (Figure 3).

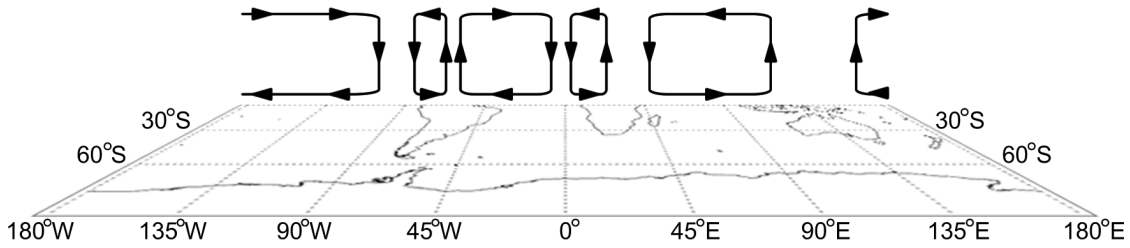

Figure 3: A schematic representation of the equatorial Walker circulation.

Outflow from deep convective towers is at a maximum near 200 hPa (*Sassi et al.*, 2001; *Folkins et al.*, 2002), and convective penetration in the tropics appears to be largely capped at about 14-15 km (θ∼360K; p∼150hPa) (*Selkirk*, 1993; *Highwood and Hoskins*, 1998; *Folkins et al.*, 1999; *Alcala and Dessler*, 2002). The latter level roughly corresponds to the level of zero net radiative heating (cf. *Dopplick*, 1972), and is often considered to be the top of the UT and the base of the tropical tropopause layer. Air detrained from tropical convection above this boundary undergoes radiative heating and will typically rise slowly toward the tropopause (e.g., *Folkins et al.*, 1999; *Sherwood and Dessler*, 2000). Conversely, air detrained below this boundary will typically radiatively cool and subside toward the boundary layer (e.g., *Mapes*, 2001).

To first order, the influence of convective detrainment of moisture into the tropical upper troposphere is governed by the temperature of the detraining layer, and current climate models parameterize it accordingly. The primary moisture source in the UT is traditionally believed to be the sublimation and evaporation of convective anvil cirrus spreading outward from the deep convective core (*Betts*, 1990; *Sun and Lindzen*, 1993; *Soden and Fu*, 1995; *Soden*, 1998, 2000; *Held and Soden*, 2000; *Tian et al.*, 2004). Taken to the logical next step, this view suggests that microphysics within the anvil may also play a pivotal role in determining UTH downstream. This hypothesis is indirectly supported by several studies. For instance, *Sun and Lindzen* (1993) successfully simulated the tropical tropospheric water vapor distribution with a model that parameterized convection based on surface temperature and included microphysical effects but not the large-scale circulation. *Soden* (2000) and *Tian et al.* (2004) observe that the diurnal cycle of UTH lags that of convection by about 2-12 hours in geostationary satellite observations, implying that significant moistening is in fact

due to sublimation and evaporation of anvil ice, rather than solely due to water vapor detrained from the convective tower. *Price* (2000) observed a strong correlation (r = 0.9) between NASA Water Vapor Project UTH and global lightning frequency, a variable closely related to ice microphysics. The modeling results of *Del Genio et al.* (2005) indicate that an assumption that convective detrainment consists of large ice particles leads to a drier and less cloudy UT, resulting in a stronger longwave cooling consistent with the "iris hypothesis" proposed by *Lindzen et al.* (2001); conversely, if small ice particles are assumed, an enhanced water vapor feedback is observed in the UT, as would be expected based on the "thermostat hypothesis" proposed by *Ramanathan and Collins* (1991).

In addition to the impact of ice in close proximity to convective towers, the detrainment and advection of anvil ice can lead to sublimation and moistening, an effect that is largely unaccounted for in most current climate models (*Del Genio et al.*, 2005). Detrainment cirrus typically last between 19-30 $\pm$ 16 hours, and can advect up to 1000 km during their lifetimes (*Luo and Rossow*, 2004). While these cirrus do not typically contain sufficient water to significantly moisten the UT, the atmospheric motions that maintain them can pump water vapor from moister levels below, leading to pockets of elevated UTH that can persist long after the cirrus have dissipated (*Sherwood*, 1999; *Luo and Rossow*, 2004).

Dessler and Sherwood (2004) present the idea of "convective contrast", which refers to the difference between the abundance of a constituent in the convective outflow and the abundance of that same constituent in the ambient air. Their results indicate that the influence of convective detrainment of water vapor and ice on the local specific humidity may be intrinsically dependent upon the ambient relative humidity. Because convective regions tend to be saturated, this idea implies that the advection of anvil ice away from the convective center and into regions of lower relative humidity may be a particularly efficient mechanism for moistening the upper troposphere, so long as sufficient condensate remains in the advected parcel.

Climate models are often poorly equipped to handle the evolution and microphysics of anvil clouds, preferring instead to detrain a fixed fraction of convective condensate (*Tian et al.*, 2004; *Del Genio et al.*, 2005). As a result, an improved understanding of the spatial

and temporal limits of the influence of detrained ice may yield improvements in the parameterization of interactions between deep convective anvils and the UTH distribution in climate models.

Numerous studies have used satellite data to investigate the relationship between deep convection and UTH in the tropics. These studies generally fall into two main categories: those that use the 6.7 μm water vapor absorption band (e.g., *Soden and Fu*, 1995; *Udelhofen and Hartmann*, 1995; *Soden*, 2000; *Tian et al.*, 2004), and those that rely on microwave observations (e.g., *Chen et al.*, 1999; *Dessler and Sherwood*, 2000; *McCormack et al.*, 2000; *Zhu et al.*, 2000; *Sassi et al.*, 2001; *Chung et al.*, 2004). The former class of studies is limited by the sensitivity of the 6.7μm channel to a broad altitude range in the UT (500-100 hPa; *Soden and Bretherton*, 1993) and clear-sky requirements. The latter allows for improved vertical resolution in the UT and reduces the clear-sky requirement (*Read et al.*, 2001), but has traditionally been limited by coarse horizontal and time resolutions.

The water vapor distribution in the UT has also been observed by *in situ* instruments, such as radiosondes (e.g., *Jordan*, 1958), and more recently by instruments onboard aircraft (e.g., *Bortz et al.*, 2006); however, these observational platforms are highly localized in space and time, and their applicability to studying the evolution of convective detrainment is limited. Relationships between convection and UTH can also be simulated using parameterizations ranging from simple conceptual models (e.g., *Sun and Lindzen*, 1993; *Folkins et al.*, 2002; *Dessler and Sherwood*, 2004) to general circulation models (e.g., *Del Genio et al.*, 2005); however, these techniques necessarily require simplified physics, and cannot replicate the totality of natural processes.

The occurrence of convection has typically been defined in the above studies by cold brightness temperatures in the 11 μm band on geostationary satellites (e.g., *Soden*, 2000; *Sassi et al.*, 2001). This technique provides little information other than where and when the cloud exists, and certainly is unable to observe the vertical profile within the convective tower. Aircraft observations of clouds provide much more information about the structure and composition of the cloud (e.g., *Heymsfield et al.*, 2005), and trajectories from these

locations used in conjunction with satellite data could provide information about the evolution of convective detrainment with regard to ice microphysical parameters in the detraining layer; however, these observations are highly localized and cannot be used to characterize relationships throughout the global tropics.

Recent advances in satellite technology provide the means to remove some of the limitations that bound previous studies. In particular, the Atmospheric Infrared Sounder (AIRS) retrieves vertical profiles of temperature and water vapor throughout the troposphere during both day and night, and in the presence of up to 70% cloud cover (*Aumann et al.*, 2003). The Tropical Rainfall Measuring Mission (TRMM) Precipitation Radar (PR) provides the first spaceborne rain radar observations, allowing the vertical characterization of convective systems throughout the global tropics (*Kummerow et al.*, 1998). The Moderate Resolution Imaging Spectroradiometer (MODIS) allows further characterization of cloud top properties (*King et al.*, 2003).

We evaluate the spatial and temporal limits of the influences of temperature, cloud ice water content (IWC), mean ice effective radius (r_{ei}), and ambient relative humidity on the distribution of water vapor in the tropical UT. Chapter 2 introduces the data and method; Chapter 3 explores the evolution of convective detrainment in the tropical UT; Chapter 4 investigates the regulatory role of ambient relative humidity; Chapter 5 performs comparisons with a simple model; and Chapter 6 provides concluding remarks and discusses future work.

CHAPTER II

DATA AND METHOD

2.1 Data

Several recent satellites have begun to observe aspects of the hydrological system in ways that are both innovative and unprecedented. This study undertakes to combine several advances in remote sensing into a consistent and useful method for analyzing the relationships between tropical deep convection and upper tropospheric humidity.

2.1.1 Precipitation Radar

Convective location, depth, and intensity are determined using observations from the TRMM Precipitation Radar (PR) (*Kummerow et al.*, 1998, 2000). The TRMM satellite was launched in 1997, and carries a suite of three instruments designed to observe the diurnal cycle of rainfall and energy exchange throughout the tropics and subtropics (35°S to 35°N). The primary purpose of the TRMM PR instrument is to determine the amount and three-dimensional distribution of rainfall; however, it also allows for the identification and characterization of the properties of deep convective clouds (e.g., *Petersen and Rutledge*, 2001; *Alcala and Dessler*, 2002).

Spaceborne radar systems offer significant advantages over networks of airborne and ground-based radars due to both increased areal coverage and a consistent calibration across regions. In addition, the near-nadir vantage point provides a much better vertical profile of convective systems on average than ground-based radars. For the purposes of this study, it is also worth noting that a spaceborne instrument will provide improved observations at high altitude, simply because it views the system from above.

The TRMM PR operates at two frequencies straddling 13.8 GHz, and scans a 215 km swath every 0.6 seconds. We use the 2A25 algorithm volumetric radar reflectivities, which represent the amount of precipitation-sized hydrometeors within the observed volume. The

horizontal resolution of the observations is 4.3 km at nadir, increasing to about 5 km at the maximum incidence angle of 17°, and the vertical resolution ranges from 250 m to about 1.6 km. Reflectivity profiles from the TRMM PR have been shown to agree well with high resolution aircraft and ground-based measurements for precipitating systems larger than the footprint size, even at outer incidence angles (*Heymsfield et al.*, 2003),

Radar reflectivity is a useful proxy of convective intensity; it is not, however, directly relevant to studies of climate. As a result, we convert the TRMM PR observations from equivalent radar reflectivity factor (Z_e), expressed in units of mm^6 m^{-3}, to ice water content (IWC) , expressed in units of g m^{-3}. Ice water content is a fundamental aspect of clouds and has been shown to be important to the Earth's radiation budget (e.g., *Stephens and Greenwald*, 1990b). The conversion is accomplished using an empirical relationship built on aircraft measurements of IWC and particle size distributions in low latitude convectively-generated anvil ice cloud layers (*Heymsfield et al.*, 2006):

$$\mathrm{IWC} = 0.0778 Z_e^{0.513} \tag{1}$$

Direct measurements of both IWC and coincident particle size distributions (PSDs) during the Cirrus Regional Study of Tropical Anvils and Cirrus Layers Florida Area Cirrus Experiment (CRYSTAL-FACE) were used to develop mass-dimension relationships (*Heymsfield et al.*, 2004). The additional PSDs used to derive the algorithm summarized in equation (1) were obtained in Hurricane Humberto (2001) during the fourth Convection and Moisture Experiment (CAMEX) using Droplet Measurement Technologies Particle Measurement Systems 2D-C and 2D-P imaging probes on board a DC-8 aircraft (*Heymsfield et al.*, 2006). The sampling interval of the instruments is 5 s, and the probes cover a size range from 50 μm to 1 cm. Distributions of particles larger than 1 cm are included using the particle reconstruction technique of *Heymsfield and Parrish* (1978).

These PSDs are used to estimate the radar reflectivity that would be observed by the TRMM PR. The PSD thus acts as a conversion factor of sorts between radar reflectivity and ice water content. The derivation of Equation (1) incorporates Mie scattering calculations for spherical particles; at the TRMM radar wavelength the associated errors are typically not

large. The derived radar reflectivities have been evaluated according to direct measurements of radar reflectivity at the *in-situ* aircraft position (*Heymsfield et al.*, 2005).

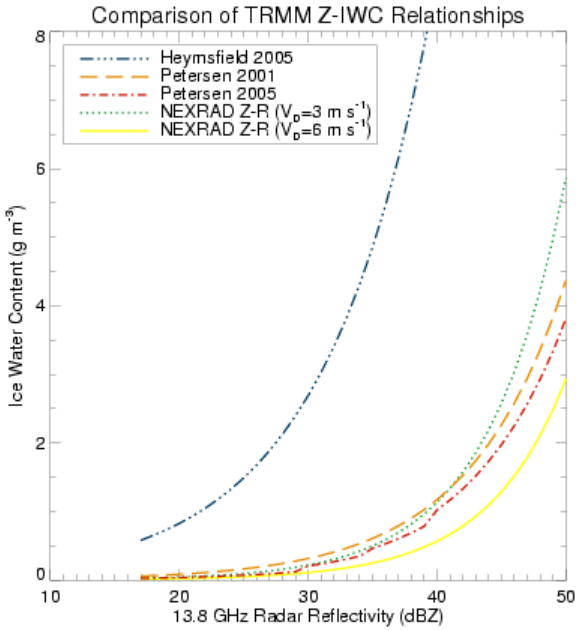

Figure 4: A comparison of five methods for computing IWC from Z_e.

Previous studies have noted that several Z_e-IWC relationships exist, and that applying one relationship to the entire tropics is potentially problematic (e.g., *Petersen and Rutledge*, 2001; *Heymsfield et al.*, 2005). An evaluation of several different algorithms (Figure 4) indicates that quantitative IWC estimates can differ by up to a factor of 10. While the four curves clustered toward lower IWCs in Figure 4 use an array of methodologies, each computes only the portion of IWC due to precipitation-sized ice. Since this study focuses on hydration of the UT, we are primarily concerned with smaller ice that will not precipitate quickly. Accordingly we apply the method described in (1),which relates the precipitation ice signal to a particle size distribution, thus considering the contribution of smaller ice as well. This method is shown as a blue dash-dot-dot-dot curve in Figure 4. We note that the quantitative differences between methods are primarily a matter of scale, and find that the choice of method does not significantly affect the qualitative nature of our results.

2.1.2 Moderate Resolution Imaging Spectroradiometer

The mean cloud ice particle effective radius (r_{ei}) at the point of detrainment is estimated using data from the MODIS instrument onboard NASA's Terra satellite. MODIS uses six visible and near-infrared spectral bands to detect r_{ei} (weighted toward cloud top) at individual pixels with a resolution of 1 km (*King et al.*, 2003). These pixel-level products are aggregated at $1^\circ \times 1^\circ$ spatial resolution on a daily basis, producing a level 3 histogram of r_{ei}. We attach the daily mean value of the gridbox containing each selected TRMM observation point to the resulting trajectory.

The lifetime of many tropical deep convective clouds is short ($\sim$3 hours) compared to the temporal resolution of the MODIS data (1 day), and known biases exist in the MODIS observations (*Platnick et al.*, 2003). The two primary sources of bias are: i) the observed values are weighted toward cloud top where updrafts usually promote larger particles; ii) the plane parallel model for radiative transfer used by MODIS consistently overestimates the droplet size by 25%-50% (*Rawlins and Foot*, 1990; *Nakajima et al.*, 1991; *Kaufman and Nakajima*, 1993; *Reid et al.*, 1999). These biases are systematic in nature, and do not greatly impact the relative size distribution. Additionally, recent comparisons with droplet size distribution measurements from Polarization and Directionality of the Earth's Reflectances onboard the Advanced Earth Observation Satellite indicate that MODIS does well at characterizing the qualitative nature of ice PSDs over oceans, but that the occurrence of small particles may be underestimated over land fields of view (*Brèon and Doutriaux-Boucher*, 2005). On the other hand, the spectral method employed by MODIS is expected to generate better statistics over both land and ocean than the polarization method. Accordingly, we do not attempt to interpret the data in a quantitative way, but instead work to develop a general and qualitative picture of how the mean effective radius of cloud ice in and near convection may influence UTH.

2.1.3 Atmospheric Infrared Sounder

Humidity observations are taken from the AIRS instrument onboard NASA's Aqua satellite (*Aumann et al.*, 2003). These observations represent the synthesis of both infrared and

microwave radiances, allowing the retrieval of full temperature and water vapor profiles in up to 70% cloud cover. The initial profile is retrieved using the water vapor or temperature channels of the Atmospheric Microwave Sounding Unit (AMSU). The microwave profile is then used as an initial guess for the infrared retrieval, which is based on an optimal fit to a subset of 2378 AIRS spectral channels, 66 for water vapor and 147 for temperature. The visible and near infrared photometer provides diagnostic support during the daytime, flagging clouds and surface changes within the field of view.

We use water vapor and temperature observations from version 4.0.9 of the standard and support products. The horizontal resolution of the orbital products is 40.5 km at nadir, corresponding to nine gridded and spatially averaged infrared spectrometer measurements and one AMSU measurement, and near global coverage is provided twice daily. Standard product water vapor mass mixing ratio (g kg^{-1}) profiles are retrieved at 12 standard pressure levels between the surface and 100 hPa with a vertical resolution of 1-3 km, and are matched with a climatological profile above 100 hPa.

Support product water vapor column densities are reported on one hundred levels between the top of the atmosphere and the surface. This study makes use of nine levels between 300 hPa and 200 hPa, which roughly correspond to 201, 212, 223, 235, 247, 260, 273, 286, and 300 hPa. The weighting functions for these vertical levels are not necessarily mutually independent (*E. Olsen*, personal communication); however, we are interested in the local humidity surrounding a parcel rather than the vertical structure of the profile. Column densities (molecules cm^{-2}) are converted to mass mixing ratio (g kg^{-1}) for ease of comparison to the standard product.

Relative humidity with respect to ice (RH_i) is calculated for the two standard product layers between 300 hPa and 200 hPa (300-250 hPa; 250-200 hPa) using the AIRS standard water vapor and support temperature products. An average temperature is derived for each layer assuming piecewise linearity in the support product temperature profile (5 levels ranging from 300 hPa to 247.4 hPa for the lower layer; 6 levels ranging from 260 hPa to 190.3 hPa for the upper), and the layer mean saturation vapor pressure with respect to ice ($e^{\#}$) is estimated using the modified Clausius Clapeyron equation:

$$\ln e^{\#} = 23.33086 - \frac{6111.72784}{T} + 0.15215 \ln T, \tag{2}$$

where T is the layer mean temperature. This relationship has been shown to be accurate to within 0.14% for 193 K $\leq T \leq$ 273 K (*Emanuel*, 1994). The computed saturation vapor pressure is then converted to saturation mass mixing ratio with respect to ice ($w^{\#}$), in units of g kg^{-1}:

$$w^{\#} = \varepsilon \left(\frac{e^{\#}}{p - e^{\#}} \right) * 10^3 \tag{3}$$

where p is the layer mean pressure and $\varepsilon = 0.622$ is the ratio of the mean molecular weights of water vapor and dry air. Relative humidity with respect to ice is calculated as the ratio of AIRS mass mixing ratio to saturation mass mixing ratio, $w/w^{\#}$. These data are averaged and aggregated into a 1° × 1° grid, and both the orbital product and the gridded product are used.

Comparison with dedicated radiosondes suggest that AIRS temperature is within ± 1 K and AIRS water vapor is within 20% on 2km levels throughout the troposphere (*Fetzer et al.*, 2005). Temperature profiles have been evaluated globally against European Centre for Medium-Range Weather Forecasting reanalyses, and indicate agreement to within ±0.5 K over ocean and between -0.5 and 1.5 K over land. In addition, *Hagan et al.* (2004) and *Gettelman et al.* (2004) have independently evaluated AIRS water vapor and temperature between 500 hPa and 100 hPa using Pre-Aura Validation Experiment aircraft measurements taken over Costa Rica and Houston, Texas. Both studies indicate that AIRS upper tropospheric water vapor profiles agree with aircraft measurements to within 25% for measurements matched within one hour in time and 100 km in space. *Gettelman et al.* (2004) further reports that AIRS temperature measurements are generally within ± 1.5 K, and concludes that relative humidity products derived from AIRS are reliable through 200 hPa.

2.1.4 Meteorological Data

The meteorological data are taken from United Kingdom Meteorological Office (UKMO) reanalyses (*Swinbank and O Niell*, 1994). This data is the product of an assimilation system first operated for diagnostic support during the Upper Atmosphere Research Satellite mission in 1991, and was developed with a focus toward providing accurate reanalysis data in the upper troposphere-stratosphere system. Satellite and radiosonde data are assimilated into a stratosphere-troposphere configuration of the UKMO Unified Model, which has also been used for climate simulations and numerical forecasting.

UKMO winds and temperatures are updated daily at 12 UTC on a 2.5° latitude × 3.75° longitude grid on 18 pressure surfaces (1000, 850, 700, 500, 400, 300, 250, 200, 150, 100, 70, 50, 30, 10, 5, 2, 1, 0.4 hPa).

2.2 Trajectory Model

Lagrangian trajectory models have gained widespread traction in the atmospheric research community due to their low computational expense and broad applicability. The basic purpose of an atmospheric trajectory model is to describe the motion of an air parcel in space and time. A typical model formulation in two spatial dimensions accomplishes this by applying information about the local wind field $[u(x, y, t), v(x, y, t)]$, in a system of ordinary differential equations:

$$\frac{dx}{dt} = u(x, y, t), \frac{dy}{dt} = v(x, y, t) \tag{4}$$

subject to initial conditions $[x(0), y(0)] = (x_0, y_0)$ with x and y the zonal and meridional positions, respectively.

The extension of this formulation to three dimensions is done by defining a vertical coordinate and an associated rate of change. The formulation used here uses θ, equal to the potential temperature of the parcel. Changes in θ are described by the diabatic heating rate, $\dot{\theta}$, which encompasses estimates of the radiative and latent heating experienced by the parcel.

2.2.1 Formulation

We use the Goddard fast trajectory model (*Schoeberl and Sparling*, 1995), which has been used successfully for diagnostic studies in both the upper troposphere (e.g., *Dessler and Sherwood*, 2000) and stratosphere (e.g., *Schoeberl and Morris*, 2000; *Morris et al.*, 2003). Meteorological fields are interpolated vertically from isobaric to isentropic surfaces for the integration of the model, and the horizontal position at each timestep is computed via a fourth order Runge-Kutta numerical integration of the UKMO winds.

Vertical motions along the trajectory are estimated from daily diabatic heating rates The radiative component is calculated according to the radiative transfer model of *Rosenfield et al.* (1994), with UKMO temperatures as the primary input, The model also incorporates a broadband parameterization of infrared heating and cooling along with a solar absorption routine, and includes absorption and emission by carbon dioxide, ozone, and water vapor. The latent heating component is represented by monthly mean estimates of latent heating from UKMO.

2.2.2 Criteria and Application

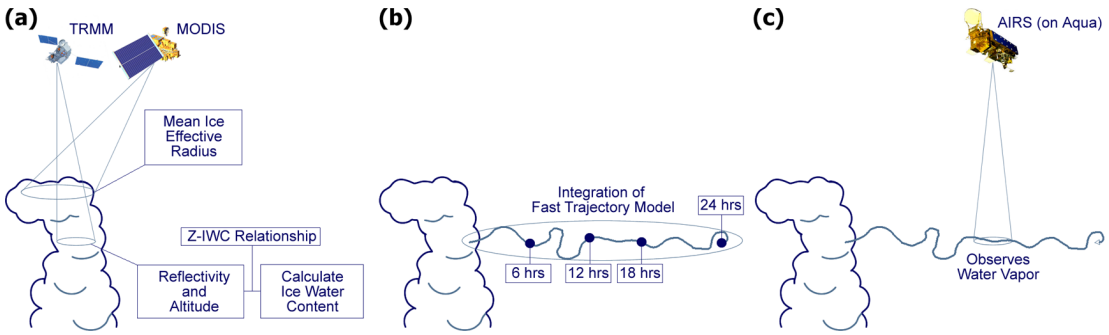

Figure 5: Schematic illustration of the method used in this study. (a) Tropical deep convective events are identified and categorized; (b) the position is integrated forward in space and time using a trajectory model; and (c) the calculated positions are matched to observations of water vapor wherever possible.

We identify tropical deep convection as TRMM PR "rain-certain" observations for the entire tropics between 15°S and 15°N with altitudes above 10 km and radar reflectivities greater than 20 dBZ (see Figure 5a). The altitude threshold allows us to focus on the convective systems most likely to impact upper tropospheric humidity, while the reflectivity

threshold is chosen to exceed the TRMM PR noise threshold of ∼17 dBZ. We associate each observation with the daily mean MODIS ice cloud effective radius, and further classify the convective event as continental or maritime according to the $1^\circ \times 1^\circ$ land-sea mask provided with the AIRS Level 3 gridded product.

The locations of TRMM PR reflectivities meeting our thresholds are used as inputs to the trajectory model described in 2.2.1 and integrated forward in space and time for five days (Figure 5b). Here, we have analyzed only the initial twenty-four to forty-eight hours following convection. The trajectory integration is performed on a timestep of one fiftieth of a day, or about 30 minutes, and winds and heating rates are interpolated to the trajectory point at each timestep. The UKMO temperature at the point of parcel injection (corresponding to the altitude and horizontal position of the TRMM PR observation) is hereafter referred to as the detrainment temperature (T_{det}) of the trajectory.

Upon completion of trajectory integration, we attempt to match each trajectory point spatially and temporally to AIRS water vapor observations (Figure 5c). In keeping with the existing validation (*Gettelman et al.*, 2004; *Hagan et al.*, 2004; *Fetzer et al.*, 2005), we select our matching criteria for water vapor mass mixing ratio to include only those AIRS retrievals within a $1^\circ \times 1^\circ$ box centered on the trajectory point and within 1 hour following the trajectory passage. These criteria are relaxed slightly for the relative humidity analysis (Chapter 4) to include observations up to 24 hours prior to trajectory passage; however, the requirements following trajectory passage remain the same.

2.2.3 Advection-Condensation Model

Our trajectory analysis can also double as an advection-condensation model for comparison to the matched observations. The basic advection-condensation model formulation begins with a saturated parcel detraining from convection. That parcel is then advected through the large-scale circulation and temperature field using a Lagrangian trajectory model. Any time the temperature reaches the dewpoint, the water vapor content of the parcel is assumed to condense, the condensate is removed, and the humidity is reset to the new saturation mixing ratio. In this way, the large-scale humidity distribution can be largely reproduced

without any explicit parameterization of convection or cloud microphysics (*Sherwood*, 1996b; *Salathè and Hartmann*, 1997; *Pierrehumbert and Roca*, 1998; *Dessler and Sherwood*, 2000, 2004).

We store the interpolated UKMO temperature and pressure at each timestep along the trajectory. Saturation mixing ratios with respect to ice are calculated according to equations (2) and (3), and condensation is considered to occur any time the Lagrangian parcel mixing ratio exceeds the local saturation mixing ratio. All condensate is considered to precipitate out of the parcel. Accordingly, the parcel mixing ratio at any timestep is precisely equal to the lowest saturation mixing ratio encountered previously along the trajectory.

2.2.4 Imposed Temperature Perturbations

Convection induces gravity waves that propagate in both the horizontal and vertical direction. For our purposes we are primarily interested in the former, which are typically approximately hydrostatic and have a vertical group velocity near zero (*Lane and Reeder*, 2001). *Lane and Reeder* (2001) estimate that the spectrum of convectively forced gravity waves that meet these conditions is characterized by intrinsic frequencies ($\hat{\omega}$) between 3.5×10^{-3} s^{-1} and 5.2×10^{-3} s^{-1}.

We have calculated the temperature variance for four flights at constant altitude within the 300-200 hPa layer during the Tropical Ocean Global Atmosphere Coupled Ocean Atmosphere Response Experiment (TOGA-COARE) mission. Temperatures are sampled from a DC-8 aircraft at a time resolution of 1 s. Although the flights are moving much faster than the background wind speed, and are typically not moving in the Lagrangian direction, these provide a crude first estimate of temperature fluctuations in the vicinity of tropical deep convection. The minimum variance was approximately 0.1 K, while the maximum was approximately 1.2 K. We conservatively scale the upper limit down by approximately one fourth to account for possible changes in large scale temperature along the aircraft flight track. We then apply a method similar to that of *Jensen and Pfister* (2004) to each trajectory.

First, a spectrum of eighteen intrinsic frequencies is defined, evenly spaced in $\hat{\omega}$ between

3.5×10^{-3} s^{-1} and 5.2×10^{-3} s^{-1}. The temperature perturbation along the trajectory is then defined as

$$\Delta T = \sum_{\hat{\omega}} \mid T \mid \sin(\hat{\omega}t + mz + \phi) \tag{5}$$

where $\mid T \mid$ is a random temperature variance between 0.1 and 0.3 K, ϕ is a random phase on $\hat{\omega}$, m is a randomly defined vertical wavenumber in the range 0.13-0.4 km^{-1}, and z is the geometric detrainment altitude of the trajectory. An arbitrary time series of temperature perturbations derived using this method is shown in Figure 6.

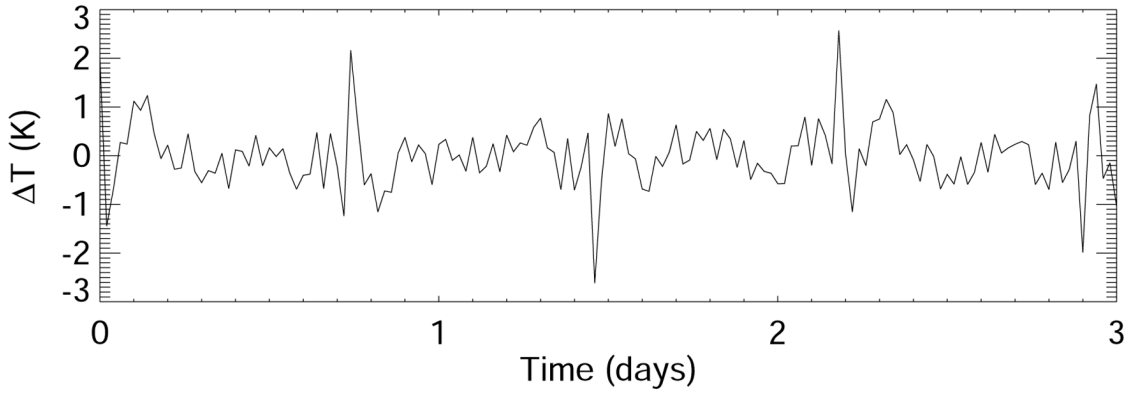

Figure 6: Arbitrary temperature perturbation, such as might be imposed on a time series of trajectory temperature.

A similar time series of temperature fluctuations is applied to each trajectory individually. The resulting temperature variability is consistent with the 1-4 K reported by *Boehm and Verlinde* (2000).

2.3 Analysis Domains

The analysis domain for this study is shown in Figure 7 (dashed lines), along with the distribution of deep convective events that meet the selection criteria (filled contours; see Subsection 2.2.2). The number densities of deep convection shown in this figure count all instances of $dBZ_e \geq 20$ dBZ at altitudes ≥ 10 km, and thus weight deeper and broader convective events more heavily. In other words, we do not attempt to aggregate disparate observations into coherent systems. Although we constrain our analysis to convective events within 15°S-15°N, the trajectories originating from these events can, and often do, cross

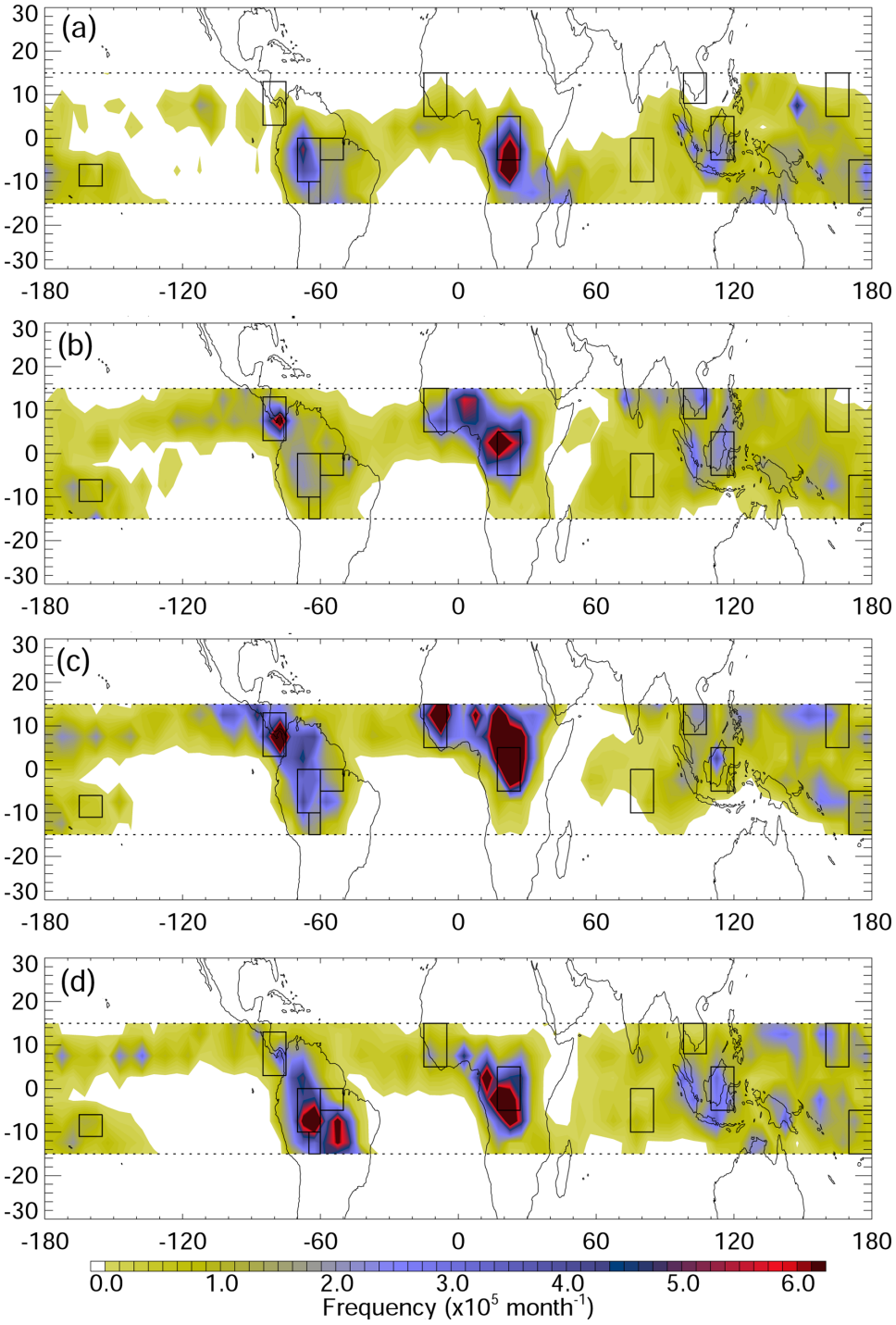

Figure 7: Frequency of TRMM PR 2A25 volumetric radar reflectivities greater then 20 dBZ and above an altitude of 10 km (filled contours) for (a) January 1-March 31 (JFM); (b) April 1-June 30 (AMJ); (c) July 1-September 30 (JAS); and (d) October 1-December 31, 2004 (OND). The 15°S and 15°N boundaries for the observation of deep convection are marked as dashed lines. Regions selected for further study are marked as solid boxes. See Table 1 for region definitions and further explanation.

beyond these boundaries. Figure 8 shows the distribution of trajectory points that are matched to AIRS observations (filled contours) within the initial 24 hours following convection.

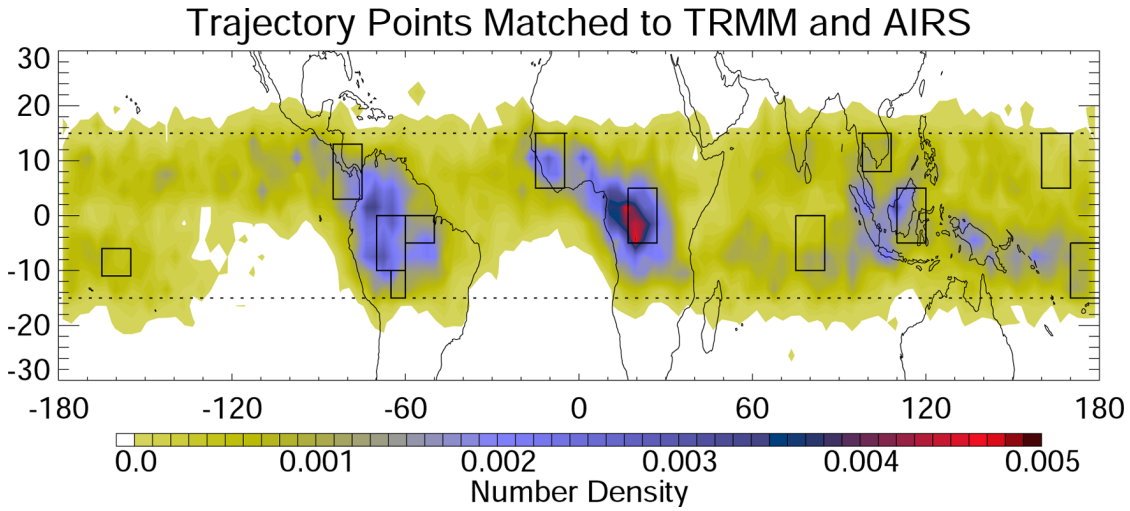

Figure 8: Normalized number density of points that are connected to both TRMM via trajectory integration and AIRS via spatial and temporal matching during the first 24 hours following convection (See Subsection 2.2.2 for details). Grid values are normalized relative to the total number of trajectory points that are successfully matched to AIRS throughout this time period.

Twelve subregions within the tropics encompassing a variety of convective regimes are selected for additional study. These regions are defined in Table 1, and their locations are shown in Figures 7 and 8 as boxes bounded by solid lines.

2.4 Statistical Treatment

Probability density functions are a useful tool for describing the inherently chaotic nature of hydrological processes, as well as for processing the large volumes of data used in this analysis into concise and descriptive formats. In particular, we will compute probability densities to describe the chance of observing a given water vapor mass mixing ratio, or change in water vapor mass mixing ratio, provided we have information about some other variable. Much of the statistical formulation described here follows from *Wilks* (2006).

Empirical two dimensional probability density functions (PDFs) are derived by smoothing the dataset using the nonparametric kernel density estimator

Table 1: Definition and general classification of the thirteen tropical regions chosen for study.

Region	Abbreviation	Boundaries
Global Tropics	GLB	180°W-180°E/15°S-15°N
	Continental	
Congo	CNG	17°-27°E/5°S-5°N
Central Amazon	AMZ	60°-70°W/0°-10°S
East Amazon	EAZ	50°-60°W/0°-5°S
Southwest Amazon	SWA	60°-65°W/10°-15°S
	Coastal	
Maritime Continent	MCN	110°-120°E/5°S-5°N
Southeast Asia	SEA	98°-108°E/8°-15°N
Central America	CAM	75°-85°W/3°-13°N
Coastal Africa	AFR	5°-15°W/5°-15°N
	Maritime	
Western Pacific Warm Pool	WPW	170°-180°E/5°-15°S
West Central Pacific	WCP	160°-170°E/5°-15°N
Indian Ocean	INO	75°-85°E/0°-10°S
Central Equatorial Pacific	CEP	155°-165°W/6°-11°S

$$Pr(x,y) = \sum_{i=1}^{n} \frac{1}{\sigma_x \sigma_y} \left[K\left(\frac{x - x_i}{\sigma_x}\right) K\left(\frac{y - y_i}{\sigma_y}\right) \right], \tag{6}$$

where n is the sample size, σ_x and σ_y are the smoothing parameters, and

$$K(t) = \frac{1}{\sqrt{2\pi}} \exp\left[\frac{-t^2}{2}\right]. \tag{7}$$

The choice of the Gaussian smoothing kernel (7) implicitly assumes that the probability of a given point provides information about the probability of nearby points, thus lessening the impact of both satellite measurement uncertainties and trajectory position uncertainty (cf. *Brooks et al.*, 2003).

Composite means are estimated using a histogram counting mechanism and the arithmetic mean. When an observation falls precisely on the boundary between two counting bins, it is counted in both bins. Normalized number densities are defined as a composite mean of ones.

Multiple linear regression is performed as a first estimate on the correlation between water vapor mass mixing ratio downstream from convection and several parameters. In this

case, we have a predictand, water vapor mass mixing ratio (w), and we want to express it in terms of several preditor variables. Specifically, these predictor variables are the detrainment temperature (T_{det}), the lowest temperature along the trajectory between convection and the current position (T_{low}), the lowest temperature along the trajectory when including imposed temperature perturbations (T'_{low}), the ice water content at the point of detrainment (IWC), and the ice cloud effective radius associated with the convective source region ($\mathrm{r_{ei}}$). The relationship is then determined by minimizing the sum of squared residuals for the equation

$$w = b_0 + b_1 T_{det} + b_2 T_{low} + b_3 T'_{low} + b_4 IWC + b_5 r_{ei} \tag{8}$$

The coefficient of determination R^2 between each variable and downstream water vapor is used as a measure of the correlation to w. R^2 is defined as the ratio of the sum of the square residuals in the observed water vapor to the sum of the square residuals in the predicted water vapor. In fact, as the five predictor variables are physically expected to act on the water vapor field, rather than the water vapor field acting on the predictor variables, R^2 can be considered a measure of the downstream water vapor variance explained by each parameter.

CHAPTER III

A TRAJECTORY ANALYSIS OF THE EVOLUTION OF CONVECTIVE DETRAINMENT

The importance of ice microphysics within the convective tower to downstream water vapor remains controversial. Here we explore the tendencies of downstream humidity relative to several variables that pertain either directly or indirectly to the bulk properties of clouds. In particular, we investigate the relative correlations of detrainment temperature, ice water content (IWC), ice effective radius (r_{ei}), and convective frequency to observed water vapor. Section 3.1 presents the relationships observed over the global tropics and investigates seasonal variability. Section 3.2 examines the regional dependence of those relationships.

3.1 Downstream Water Vapor in the Global Tropics

3.1.1 Comparison of Detrainment Temperature and Ice Water Content

Ice water content serves as a proxy for convective intensity, and largely determines the radiative characteristics of clouds above the freezing level (∼7 km; *Petersen and Rutledge*, 2001). In addition, and more pertinent for this analysis, the ice water content at the point of detrainment may help to predict the relative amount of ice remaining aloft at some point in the future. Here we explore the relationships between IWC at the point of detrainment and water vapor evolution during the initial 24 hours following convection.

Figure 9 shows composite means of AIRS water vapor observations binned according to estimated detrainment temperature (T_{det}) and IWC derived from TRMM PR radar reflectivity at the point of detrainment. It is readily apparent in all four panels of Figure 9 that the influence of T_{det} on humidity downstream from convection dominates that of IWC. Further, the influence of IWC is hardly noticable at all, particularly within the first 12 hours after detrainment. The influence of convection detraining above the 200 hPa level is visible beginning in Figure 9b, where relatively moist air can be seen near T_{det} = 215-220

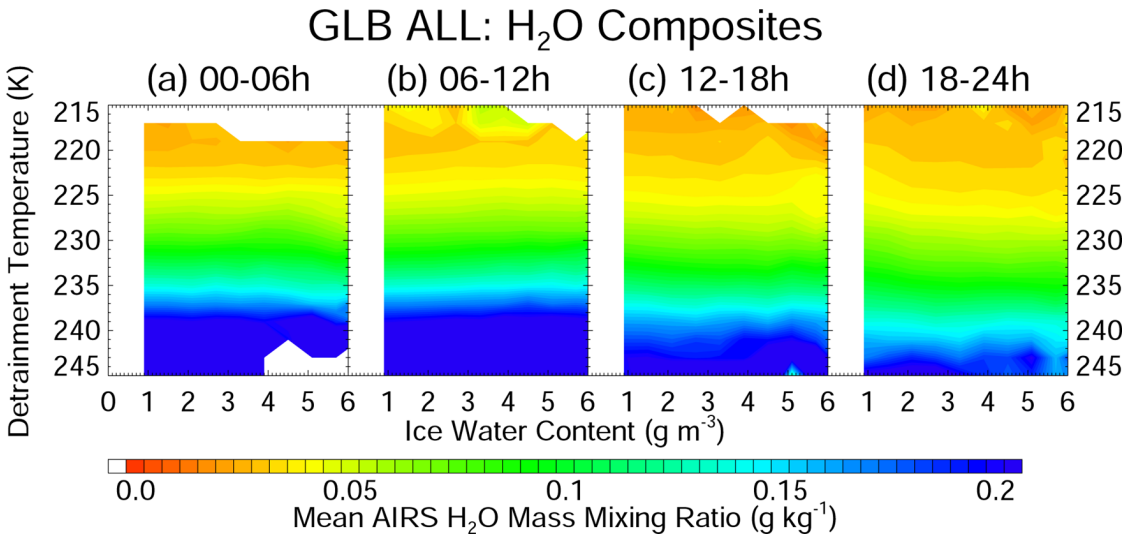

Figure 9: Composite means of AIRS water vapor observations matched to TRMM deep convection throughout the global tropics during (a) hours 0-6 following convection, (b) hours 6-12, (c) hours 12-18, and (d) hours 18-24. Observations are binned according to estimated detrainment temperature and IWC derived from TRMM PR radar reflectivity at the point of detrainment.

K. The relatively high mixing ratio of this air may be a result of swift trajectory descent to warmer temperatures with lower relative humidities, along with the concurrent evaporation of ice detrained above 200 hPa. This has potential implications for water vapor evolution at detrainment temperatures throughout the 300-200 hPa level, and we will return to this later.

The lack of an apparent relationship between the IWC of a convective layer and water vapor content downstream is actually completely logical, particularly if air detraining from convection is assumed to be saturated. In fact, while the assumption of saturated detrainment may be flawed (cf. *Tompkins and Emanuel*, 2000; *Pierrehumbert et al.*, 2006), it is not required to explain this result. Consider an air parcel detraining at a temperature of 230 K and 250 hPa, and assume (unrealistically) that it contains no water vapor whatsoever. The density of the parcel ρ can then be calculated by the equation of state for dry air as 0.38 kg m^{-3}. Further, the saturation mass mixing ratio $w^{\#}$ =0.223 g kg^{-1} can be derived using equations (2) and (3). The saturation water vapor content of the parcel is thus $\rho w^{\#}$ =0.085 g m^{-3}, about one order of magnitude less than the minimum sensitivity of the TRMM PR

Table 2: Evolution of mean humidity in 10 K detrainment temperature bins

T_{det}	00-06 h	06-12 h	12-18h	18-24h	24-36h
210-220 K	0.031 g kg^{-1}	0.042 g kg^{-1}	0.029 g kg^{-1}	0.033 g kg^{-1}	0.028 g kg^{-1}
220-230 K	0.048 g kg^{-1}	0.054 g kg^{-1}	0.047 g kg^{-1}	0.043 g kg^{-1}	0.048 g kg^{-1}
230-240 K	0.135 g kg^{-1}	0.148 g kg^{-1}	0.118 g kg^{-1}	0.100 g kg^{-1}	0.093 g kg^{-1}
240-250 K	0.275 g kg^{-1}	0.250 g kg^{-1}	0.221 g kg^{-1}	0.213 g kg^{-1}	0.154 g kg^{-1}
Overall	0.118 g kg^{-1}	0.121 g kg^{-1}	0.107 g kg^{-1}	0.103 g kg^{-1}	0.082 g kg^{-1}

to IWC (0.826 g m^{-3} using the empirical relationship described in equation (1)). If we instead consider a parcel detraining near the bottom of the layer at a pressure of 300 hPa and temperature of 245 K, the saturation water vapor content is about 0.41 g m−3, still only half the minimum IWC sensitivity. Thus, we should not expect the IWC of the detraining layer as reported in this analysis to be highly correlated with water vapor, particularly in close proximity to convection—saturation water vapor concentrations essentially preclude any such relationship down to IWC $\ll$ than the concentrations resolvable using the TRMM PR.

To take this one step further, this simple conceptual analysis actually provides a crude validation on the magnitude of IWC estimated by equation (1). If we were noting a significant correlation between IWC and downstream water vapor at these proximities to convection, we could then conclude that the algorithm drastically overpredicts the IWC.

The gradual dehydration of air leaving convection can be observed for each of four detrainment altitude bins by jointly viewing Figure 9 and Table 2. Air detraining at lower altitudes (higher temperatures) is observed to dehydrate steadily beginning at around 6 hours and continuing through 36 hours. Detrainment from higher altitudes, however, hydrates between lag times of 0-6 hours and 6-12 hours, and appears to reach a relatively stable moisture level more quickly (about 18 hours). The humidity of air detraining in the next highest altitude bin levels off next, at around 24 hours, while the lowest two detrainment bins in altitude do not appear to reach this threshold until after at least 30 hours. In the overall mean, the trajectories moisten between hours 0-6 and hours 6-12. This result is consistent with the analyses of *Soden* (2000) and *Tian et al.* (2004), who estimated that the

diurnal peak in water vapor lags that of convection by about 3-12 hours. Also considering all levels, we observe a water vapor mass mixing ratio of about 0.082 g kg^{-1} during the 24-36 hour lag time bin. This is generally consistent with the annual mean for the 300-200 hPa layer during 2004, which is estimated from AIRS gridded monthly means to be in the 0.08-0.1 g kg^{-1} range. This relaxation time to the approximate environmental mean is consistent with the estimate of 30 hours computed by *McCormack et al.* (2000), who focused only on the tropical Pacific.

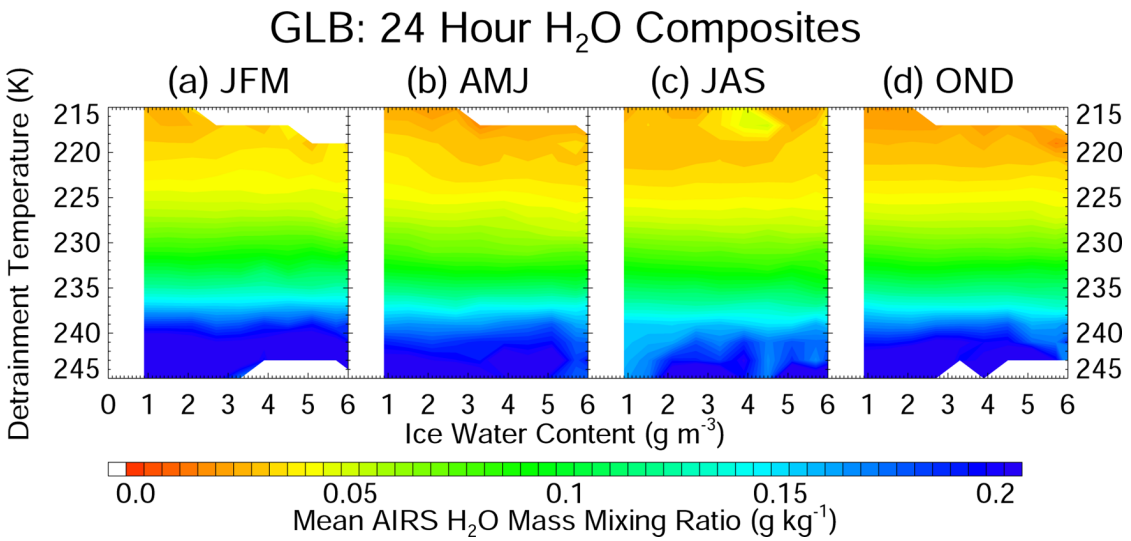

Figure 10: Seasonal composite means of AIRS water vapor observations matched to TRMM deep convection within 24 hours throughout the global tropics during (a) January-March, (b) April-June, (c) July-September, and (d) October-December. Observations are binned according to estimated detrainment temperature and IWC derived from TRMM PR radar reflectivity at the point of detrainment.

The seasonal cycle of the T_{det}-IWC-w relationship is shown in Figure 10. As in Figure 9, the dominance of T_{det} on downstream humidity is clear. The shift toward a greater percentage of deep continental convection can be observed in JAS (Figure 10c; cf. Figure 7c), by comparing the proportion of detrainment that traces back to low T_{det} to that observed in JFM (Figure 10a).

The seasonal cycle of water vapor detrainment into the UT can also be observed, with a maximum in JFM and a minimum in JAS (Figure 10c). This relationship is much more remarkable at higher T_{det} ($\sim$ 235 K), however, is hardly apparent at 220 K $\leq T_{det} \leq$ 230 K, and appears to be reversed for $T_{det} \leq$ 220 K. This relationship might be explained by

the shift from predominantly oceanic convection in JFM to more continental convection, and particularly more intense continental convection, during JAS (cf. Figures 7a and c). Continental convection is usually deeper and more vigorous than oceanic convection, and frequently exhibits larger radar reflectivities at altitudes of 12 km and above (*Petersen and Rutledge*, 2001). These differences imply that more precipitation-sized hydrometeors exist more frequently in high level anvil clouds resulting from continental convection than in those resulting from oceanic convection. If some of this ice melts or sublimates during precipitation, as the relatively high composite mean water vapor mixing ratios at low T_{det} in Figures 9b and 10c suggest, then the surrounding air would undergo latent cooling. This could lead to the formation of unsaturated downdrafts (*Squires*, 1958; *Emanuel*, 1994), which would in turn dehydrate the air that detrains at lower levels (e.g., *Tompkins and Emanuel*, 2000). Therefore, the shift toward deeper, more intense continental convection that accompanies the seasonal migration of the ITCZ in JAS (Figure 7c) could raise the vertical level at which unsaturated downdrafts can effectively dehydrate convective detrainment, which could then at least partially explain the seasonal cycle in composite mean water vapor mixing ratio at both high and low T_{det} as observed in Figure 10.

As the trajectory progresses downstream, we may expect to begin to observe a relationship between IWC and water vapor. The ice crystal number density of a parcel moving in the UT can be parameterized as an exponential decay (e.g., *Gettelman et al.*, 2002). If a constant half life is assumed for all IWCs that the TRMM PR is sensitive to (i.e., if the particle size distribution is assumed to be similar), then one would expect more ice to remain in a parcel detrained at higher IWC than in a parcel detrained at low IWC at the same lapse time from convection. Theoretically, this ice might either hydrate or dehydrate the parcel, and in fact we observe both of these modes in the results that follow.

First, we show that IWC at the point of detrainment does appear to play a substantial role in determining the normalized dehydration rate of the trajectory (filled contours in Figure 11). The normalized dehydration rate is computed for each T_{det} and IWC bin as:

$$\frac{d\bar{w}}{dt}(T_{det}, \mathrm{IWC}) = \frac{\bar{w}_{24}(T_{det}, \mathrm{IWC}) - \bar{w}_{12}(T_{det}, \mathrm{IWC})}{(12\mathrm{h}) * \bar{w}_{12}(T_{det}, \mathrm{IWC})} \tag{9}$$

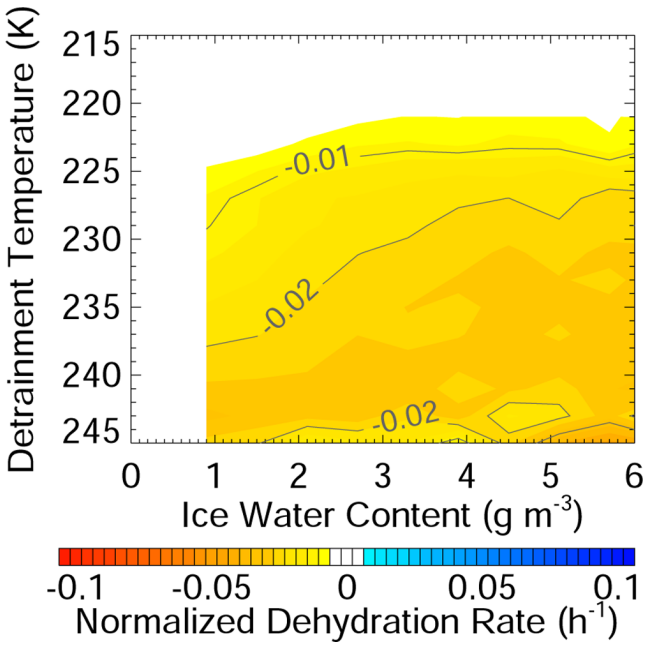

Figure 11: Composite mean dehydration rate of AIRS water vapor matched to TRMM deep convection throughout the global tropics. Observations are binned according to estimated detrainment temperature and IWC derived from the TRMM PR radar reflectivity at the point of detrainment. Contours corresponding to dehydration rates of 1% and 2% per hour are plotted in solid gray and labeled.

where w_{12} and w_{24} are the composite mean mass mixing ratio for lag times of 0-12 hours and 12-24 hours following convection, respectively. A twelve hour time interval is chosen to account for the twice-daily time resolution of AIRS. Dehydration rates for $T_{det} \leq 220$ K are removed because these trajectories typically enter the 300-200 hPa layer at later lag times (see the temporal evolution of Figure 9a-d). As a result, equation (9) introduces essentially meaningless results at these T_{det}.

Figure 11 indicates that a higher IWC generally corresponds to a faster dehydration rate throughout the temperature range. The physical basis for this arises from the microscale nature of condensation and deposition, which typically take place at the droplet or hydrometeor interface. In particular, ice and mixed phase particles lower the microscale saturation vapor pressure in their immediate environment, thus allowing condensation to take place at relative humidities in the resolved volume that are well below 100% (*Emanuel*, 1994). A larger IWC corresponds to either larger quantities of ice or larger ice particles. The former case would provide more surfaces for water vapor to condense upon, effectively spreading

the lowered saturation vapor pressure through a broader volume; the latter would lead to an even lower saturation vapor pressure at each surface. As a result, either interpretation of IWC supports the observed relationship between IWC and dehydration rate.

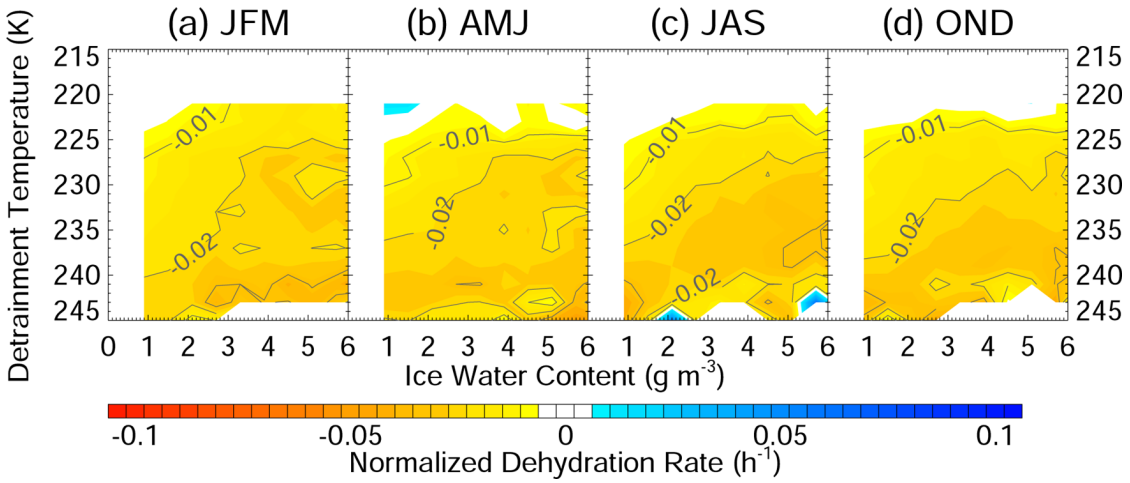

Figure 12: Seasonal composite means of dehydration rate along the trajectory during (a) January-March, (b) April-June, (c) July-September, and (d) October-December. Observations are binned according to estimated detrainment temperature and IWC derived from TRMM PR radar reflectivity at the point of detrainment. Contours corresponding to dehydration rates of 1% and 2% per hour are plotted in solid gray and labeled.

A seasonal examination of the composite mean normalized dehydration rate (Figure 12 indicates relatively little variability on a seasonal scale, although the dehydration rate does appear to be slightly stronger in JAS as compared to JFM. The solid gray contours correspond to hourly dehydrations of 1% and 2% h^{-1}. For reference, air dehydrating at a rate of 1% h^{-1} will retain about 79% of its original humidity after one day, while air dehydrating at 2% h^{-1} will retain only about 62%. Contours are also plotted for a dehydration rate of 3% h^{-1}; however, dehydration rates that strong are not observed in Figures 11 and 12.

3.1.2 Comparison of Detrainment Temperature and Ice Effective Radius

Ice cloud effective radius is an intrinsic microphysical parameter that is expected to exert a noticable influence on the downstream water vapor. For relatively large values of r_{ei}, the microphysical dehydration processes mentioned in the previous section could be expected to play a significant role, particularly at higher relative humidities. On the other end of the spectrum, small ice particles are expected to be particularly efficient for hydrating the

UT (e.g., *Sherwood*, 2002; *Del Genio et al.*, 2005). The following analysis examines the qualitative correlation between mean ice cloud effective radius and downstream water vapor.

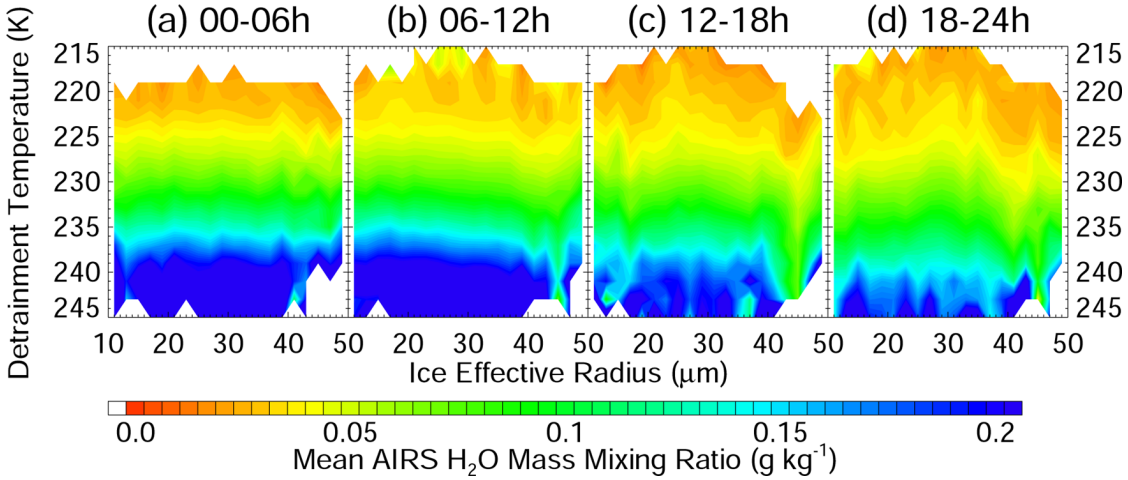

Figure 13: As in Figure 9, but observations are binned according to estimated detrainment temperature and MODIS mean r_{ei} at the point of detrainment.

Figure 13 shows composite means of AIRS water vapor observations binned according to estimated T_{det} and mean r_{ei} at the point of detrainment. A comparison with Figure 9 indicates that, although T_{det} again dominates, r_{ei} plays a more influential role in regulating water vapor detrainment than does IWC. The relationship between r_{ei} and downstream humidity appears to be neither linear nor monotonic, however. At lag times from convection of 0-6 hours (Figure 13a) the distribution exhibits very little dependence on r_{ei}. During hours 6-12 (Figure 13b) the relationship appears to be approximately monotonic, with larger r_{ei} corresponding to lower humidity. Water vapor mixing ratios are highest in the middle of the r_{ei} spectrum (20-35 μm) and lower for both low (15-20 μm) and high r_{ei} ($> 40\mu$m) during hours 12-18 (Figure 13c). During hours 18-24 (Figure 13d), the peak water vapor remains at r_{ei} between 25 and 35 μm, falls off again for $r_{ei} > 40$ μm, and remains fairly constant through the low end of the range.

These general relationships may be explained by considering the spectrum of MODIS daily mean effective radii as a proxy for a spectrum of particle size distributions. For PSDs skewed toward large ice, the tendency is toward deposition and precipitation—a net drying. For PSDs skewed toward small ice, the amount of water volume contained in the

detrainment ice may be insufficient to offset other drying influences. Together, these would explain why the peak water vapor tends to be situated in the middle of the range of r_{ei}, as well as why the observed dehydration is less for small r_{ei} than for large. Water vapor is more often maintained along trajectories with r_{ei} in the middle range because the water content is both sufficient to offset the drying tendency, and not concentrated in hydrometeors so large that they precipitate out quickly.

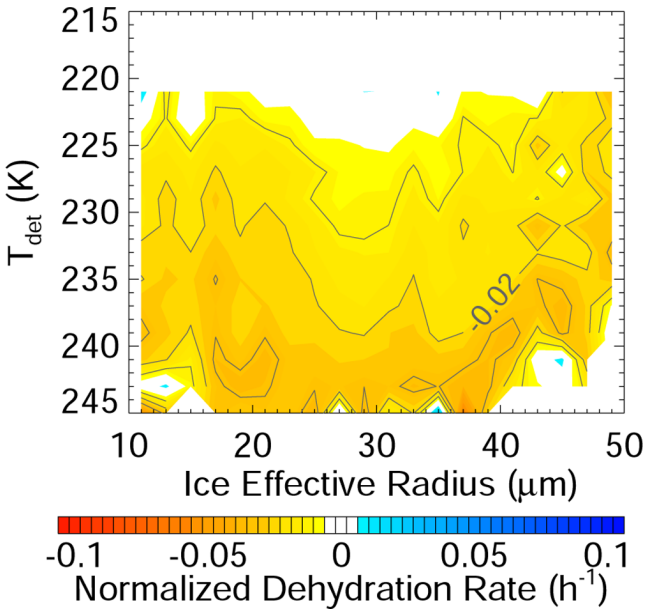

Figure 14: As in Figure 11, but observations are binned according to estimated detrainment temperature and MODIS mean r_{ei} at the point of detrainment.

The water vapor peak near the center of the ice effective radius distribution is further confirmed by Figure 14, in which the minimum dehydration rate is observed at $r_{ei} \sim 28$ μm, and the maximum dehydration rates are observed at the ends of the spectrum, particularly toward large r_{ei}. We also note that there is a local minimum in dehydration rate toward ice effective radii that are particularly small in the context of the MODIS values ($r_{ei} \sim 15\mu$m).

The signature of effective radius appears to grow with distance from convection, and is barely noticable within the initial 12 hours of convection when the bulk of the condensate is present. This is most likely a result of the air being nearly saturated at this proximity to the convective tower. Ice is unlikely to sublimate in such conditions, therefore the role of ice effective radius is minimized relative to that of detrainment temperature. This relative

influence appears to grow with the expected reduction in relative humidity as the trajectory moves away from convection, as evidenced by the growth of significant and coherent structures along the abscissa.

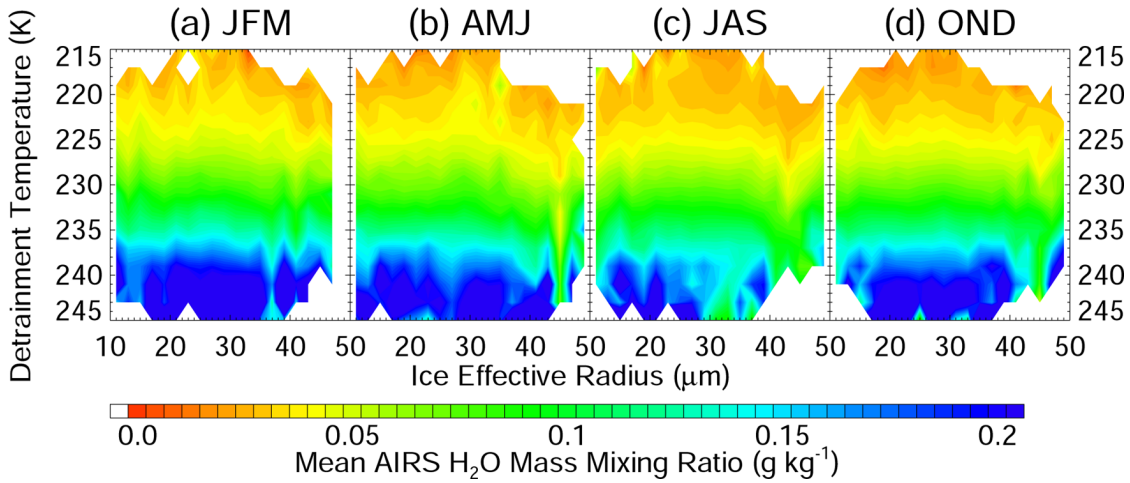

Figure 15: As in Figure 10, but observations are binned according to estimated detrainment temperature and MODIS mean r_{ei} at the point of detrainment.

Figure 15 examines seasonal variability in the observed relationship between r_{ei} and water vapor. In all four seasons, we observe a tendency toward peak water vapor at a fixed Tdet when r_{ei} is in the 20-35 μm range, particularly when T_{det} is below ~230K. The exact location of this peak varies, however, and the shift toward more continental convection that marks JAS is observed in the shift of the peak water vapor to lower r_{ei} in JAS relative to the other seasons. Although the 24-hour means shown in Figure 15 do not explicitly show it, the drop in water vapor for large ice ($r_{ei} \geq 40$ μm) is seasonally robust when we examine the time evolution along the trajectory as in Figure 13 (not shown).

This relationship is confirmed by Figure 16, which depicts seasonal variability in the normalized dehydration rate. As in Figure 14, the minimum dehydration rate is observed in the middle of the distribution, while the largest dehydration rates, some of which are even more than 3% h^{-1}, are seen at large r_{ei}. At this dehydration rate, less than 50% of the water vapor at detrainment will remain after 24 hours of trajectory evolution.

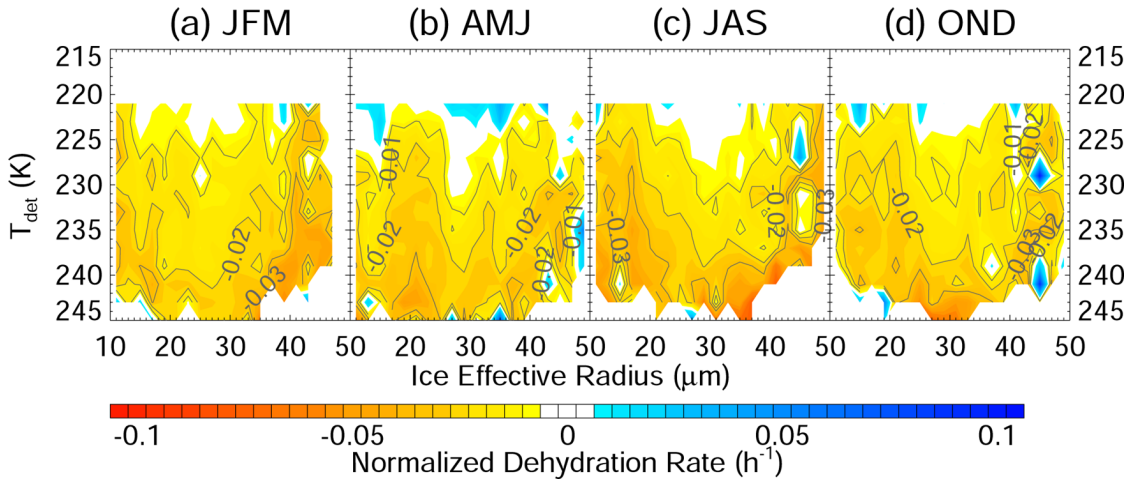

Figure 16: As in Figure 12, but observations are binned according to estimated detrainment temperature and MODIS mean r_{ei} at the point of detrainment.

Table 3: Coefficient of determination between downstream water vapor and the designated parameter.

Parameter	00-06 h	06-12 h	12-18h	18-24h	24-36h	All
T_{det}	61.5%	62.0%	38.4%	30.5%	19.1%	42.1%
IWC	0.11%	0.07%	0.001%	0.38%	0.023%	0.039%
r_{ei}	0.17%	0.004%	1.55%	0.52%	0.52%	0.44%
T_{low}	58.6%	63.0%	44.2%	39.5%	51.3%	49.3%
T'_{low}	57.6%	63.6%	46.0%	39.7%	49.1%	49.3%

3.1.3 Coefficients of Determination

The coefficient of determination between downstream water vapor mass mixing ratio and each of the analysis parameters has been examined using a multivariate linear regression (see Section 2.4). The results are presented in table 3. The contribution of detrainment temperature is, unsurprisingly, maximum near the convective source, where it appears to explain approximately 60% of the variance. This reduces to less than 20% after 24 hours. The influence of IWC is low, as might be expected from Figure 9 and the discussion above, with values of less than 1%.The influence of r_{ei} is low as well, at less than 2%; however, since the observed relationship is neither linear nor monotonic, the multivariate linear regression technique most likely underestimates the correlation. We have also examined the η^2 coefficient of determination for polynomial and nonlinear least-squares fits, and we performed

a linear regression piecewise by 10 and 5 μm bins. None of these approaches yields a value higher than 10%, and valyes higher than 5% only in four isolated instances.

We have also examined how the observations correlate with the minimum temperature experienced along the trajectory between detrainment and the parcel's present position, T_{low}. This variable appears to explain about 50% of the water vapor variability, ranging from ∼60% near the convective source to ∼40% in hours 12-24. The coefficients of determination for T_{low} remain essentially the same when temperature perturbations are imposed along the trajectory as described in 2.2.4 (T'_{low}).

3.2 Regional Variations

There exists some basis for examining the correlation of water vapor and ice parameters not only for the global tropics, but for specified regions as well. In particular, *Petersen and Rutledge* (2001) showed significant regional variability in the typical convective profile, particularly between isolated oceanic regimes and regimes that are located in coastal or continental areas. We have identified twelve regions—four continental, four coastal, and four isolated oceanic—for additional study. These regions are defined in Table 1 and outlined on the map in Figure 7. An exhaustive study based on the same analysis methods used in Section 3.1 above turned up very little interesting variability, and so we briefly summarize the results here.

Convective frequency has been related to UTH at both the regional (*Chung et al.*, 2004) and global (*Soden and Fu*, 1995) level in the tropics. The positive relationship reported by these and other studies is often cited as an indication that the moist area of the tropical UT would expand with increased convection, potentially amplifying the water vapor feedback; however, such conclusions are founded primarily on conjecture and remain controversial.

The results of this study also indicate a slightly positive correlation, statistically significant in χ^2 and robust throughout the seasonal cycle 17. Convective frequency is calculated as the ratio of the number distribution of convection (see Figure 7) to the time over which the number distribution is integrated multiplied by the area of the region, for a unit of events km^{-2} month^{-1}. It is compared to the mean AIRS water vapor matched to all trajectories

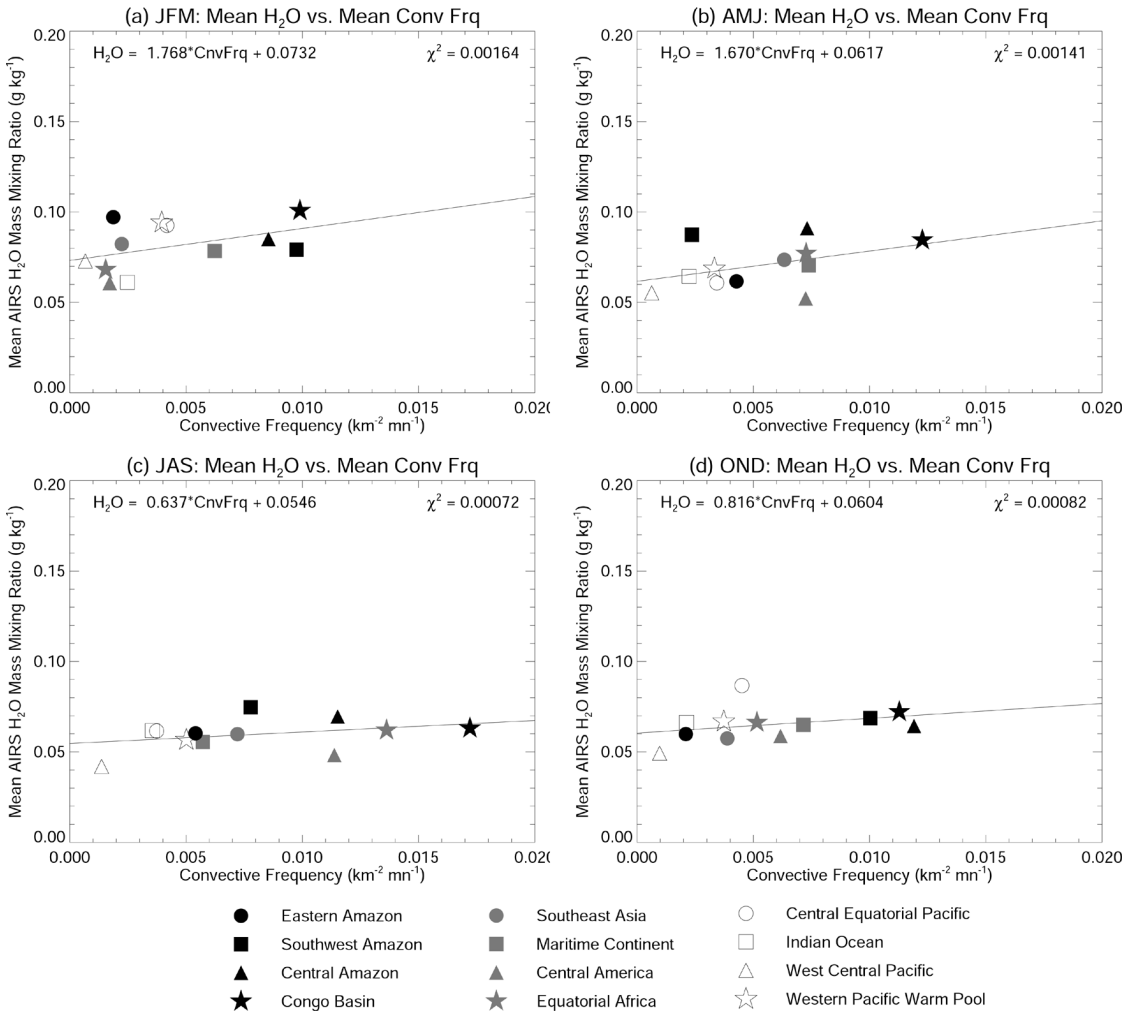

Figure 17: Regional breakdown of relationships between regional convective frequency [events km^{-2} h^{-1}] and mean downstream AIRS water vapor within 24 hours of convection for (a) January-March; (b) April-June; (c) July-September; and (d) October-December

originating in the region.

The slope of the positive relationship is least during JAS, when the typical continental convective events are most intense (cf. Figure 7c). This suggests the positive correlation is more closely related to the areal coverage and breadth of convection, rather than to the intensity or depth of the convective penetration. This result is broadly consistent with the hypothesis presented in Section 3.1 to explain the relative dryness of convective detrainment in boreal summer compared to the other seasons. As convection becomes deeper and more intense, it lofts additional precipitation ice into the anvil. As this ice precipitates, it induces stronger unsaturated downdrafts, thus limiting the overall effectiveness of this convection

as a moisture source in the UT.

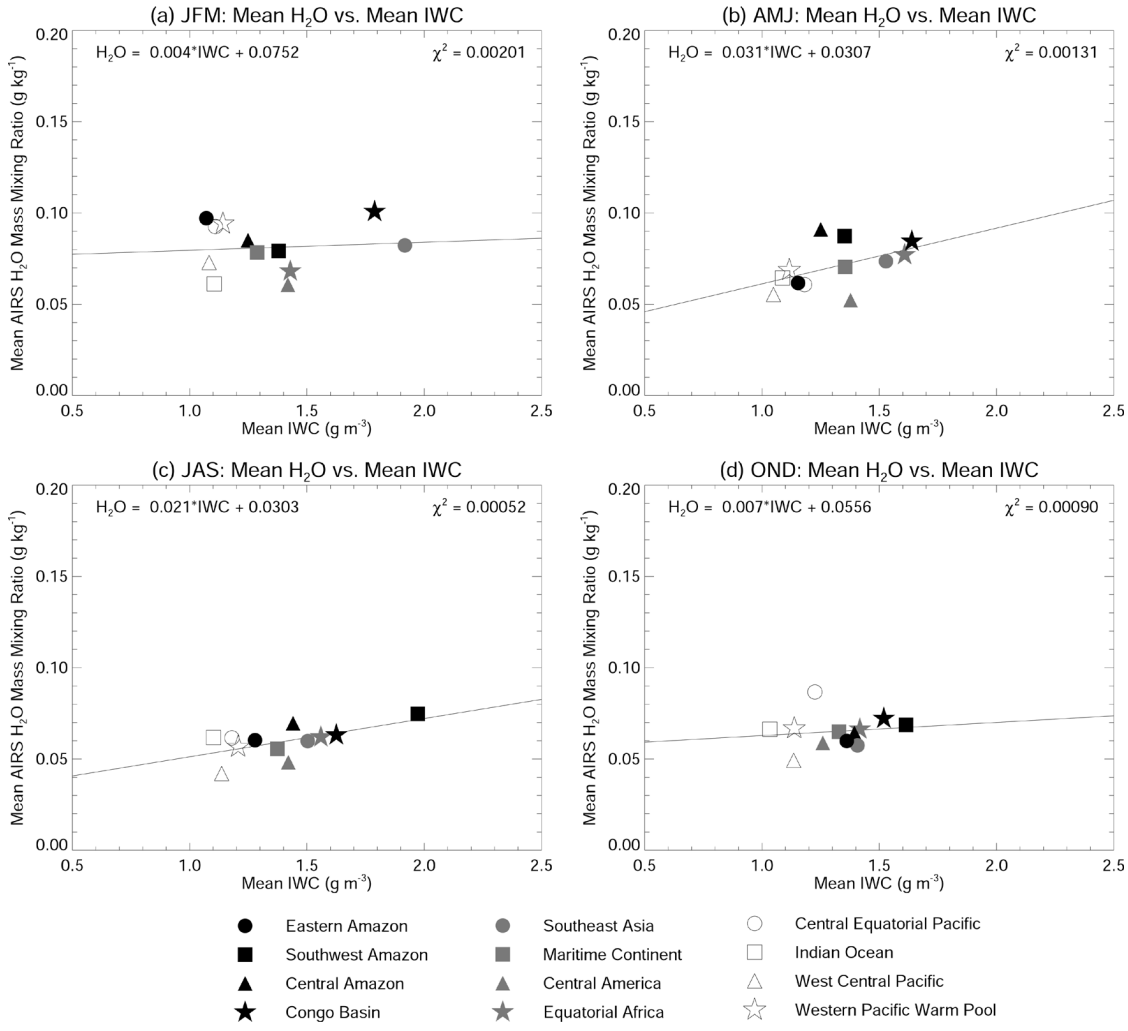

Figure 18: As in Figure 17, but for mean IWC in place of convective frequency.

Figure 18, in which mean water vapor along trajectories originating in each region is related to mean IWC, also shows a slightly positive correlation. Again, the regressions are statistically significant in χ^2 and relatively robust to seasonal variations; again, the strength of the relationship is slight. The positive nature of this relationship suggests that the IWC at the source does indeed exert an influence on humidity along the trajectory, and not only in terms of dehydration.

Unlike the previous two parameters, the relationship between regional mean ice cloud effective radius and mean downstream water vapor is not robust, and is characterized by two barely negative slopes and two barely positive slopes. This result is perhaps unsurprising

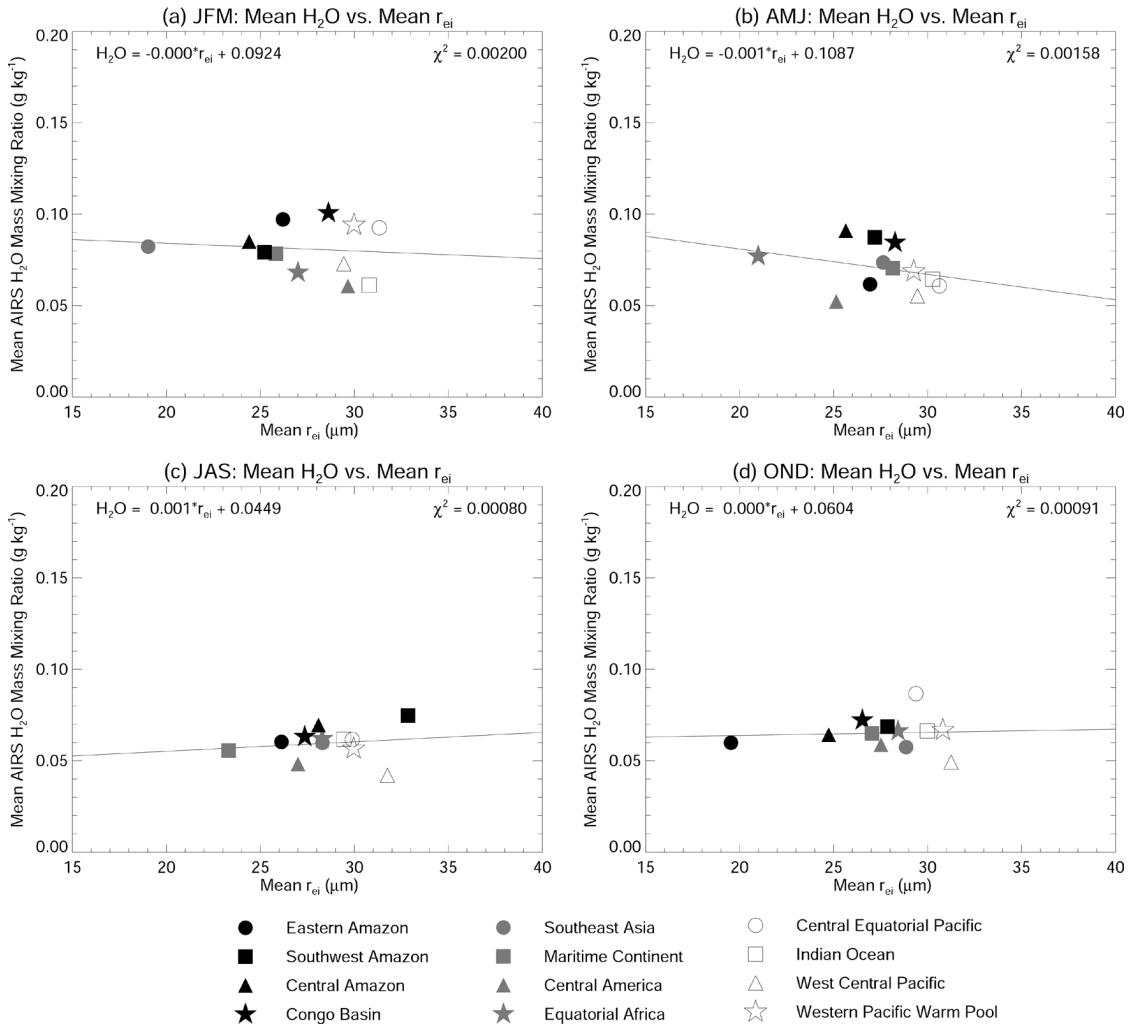

Figure 19: As in Figure 17, but with MODIS mean ice cloud effective radius in place of convective frequency.

given the apparent nonlinear nature of the relationship between r_{ei} and downstream water vapor.

In each of the three figures presented here, we also observe a clustering of the isolated oceanic regions according to cloud parameter, typically near a relatively large effective radius and a relatively small IWC and convective frequency. Continental and coastal events, however, are much more difficult to characterize and exhibit a stronger seasonality. This relatively monolithic nature of isolated oceanic convective regimes was noted also in *Petersen and Rutledge* (2001) for radar reflectivity, which relates directly to our IWC. These results indicate that the prototypical oceanic convective regime is fairly well characterized for

convective frequency and ice effective radius as well.

CHAPTER IV

THE ROLE OF AMBIENT RELATIVE HUMIDITY

As noted in the previous chapter, the role of ice is likely to be strongly modulated by the ambient relative humidity. On one hand, ice cannot sublimate unless the vapor mixing ratio is sufficiently below saturation; on the other hand, if the water vapor mixing ratio is supersaturated, water vapor may be removed through condensation onto existing ice crystals and precipitation out of the local system. This relationship implies that the influence of convective detrainment of water vapor and ice on the local specific humidity may be intrinsically dependent upon the local ambient relative humidity. In particular, the introduction of ice into subsaturated environments through either convection or advection from convective towers may be a particularly efficient mechanism for moistening the upper troposphere. In this chapter we examine the role of ambient relative humidity in regulating water vapor changes along trajectories originating from tropical deep convection during January 2004, and investigate the spatial and temporal limits of this control (Section 4.1). The results are placed into context with the background relationship (Section 4.3), and potential applications to climate modeling are discussed (Section 4.4).

4.1 Water Vapor Changes With Trajectory Passage

As in Chapter 3, we focus on convective events between 15°S and 15°N; however, this analysis is limited only to January 2004, and seasonal and regional variability is not examined. Furthermore, whereas in Chapter 3 we track the evolution of a parcel in a Lagrangian framework, here we examine the evolution of humidity in a set volume as the trajectory passes through it.

The figures show empirical non-parametric probability density functions, generated according to the method described in Section 2.4. The filled contours indicate the probability that air at a specified relative humidity with respect to ice (RH_i) has undergone a certain

change in water vapor mixing ratio (Δw; abscissa). Ambient RH_i and water vapor mixing ratio prior to trajectory passage are determined by matching each trajectory point to orbital AIRS observations within the previous 24 hours. Water vapor mixing ratio after trajectory passage is determined via an identical matching mechanism, but the time window is shortened to only one hour. Δw is then calculated by subtracting the "before" water vapor mixing ratio from the "after" water vapor mixing ratio. Normalized mixing ratio changes are derived by dividing Δw by the "before" value. Only trajectory points with matched observations both before and after trajectory passage are considered in this analysis.

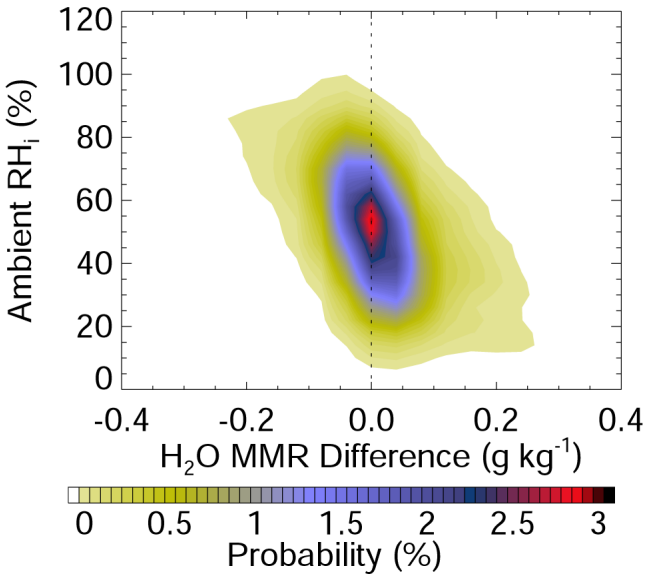

Figure 20: PDF of AIRS ambient RH_i vs. change in AIRS mass mixing ratio along trajectories detraining from deep convection during January 2004 for the global tropics.

Figure 20 demonstrates that the qualitative relationship anticipated by *Dessler and Sherwood* (2004) is indeed reproduced by the observations. In particular, the bulk of the distribution is arranged on a slightly negative slope (m $\sim$ -.14 g kg^{-1}). This slightly negative slope is overlain by a steeper negative slope (m $\sim$ -.7 g kg^{-1}) that defines two lobes: one hydrates the ambient air ($\Delta w \geq$ 0.1 g kg^{-1}), while the other has a net drying effect ($\Delta w \leq$ -0.1 g kg^{-1}). The moistening lobe exists primarily below $RH_i = 70\%$, and encompasses 8.3% of the total cases studied, while the drying lobe consists primarily of instances with $RH_i \geq$ 50%, and encompasses 4.2% of the total cases. Despite the existence of the dehydration lobe, deep convective detrainment still represents a net source of moisture in the tropical

UT.

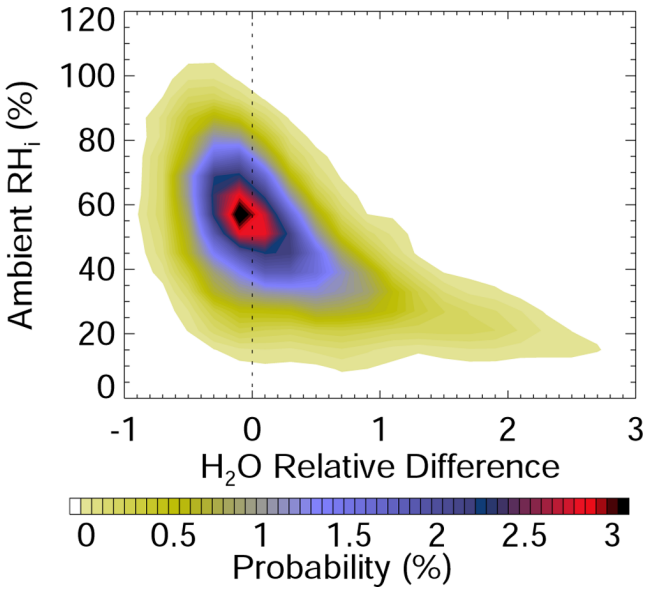

Figure 21: As in Figure 20, but for normalized changes in AIRS water vapor mass mixing ratio.

Additional insight can be gained by viewing the change in water vapor mass mixing ratio normalized by its value before trajectory passage (Figure 21). This process removes the artifacts that result from the temperature dependence of saturation mass mixing ratio. In this case we define the lobes of positive and negative change as those in which mixing ratio changes by ±50% of it's previous value (±.5 along the abscissa). Again the moistening lobe consists of RH$_i$ ≤70%, but now it comprises 15.1% of the total cases, compared to 8.3% before. The drying lobe expands to include cases between RH$_i$ ≃ 20% and RH$_i$ ≃ 100%, but only accounts for 2% of the total cases. These results indicate that the moistening lobe prevails for not only low RH$_i$, but for low w as well. That is, the moistening lobe applies to areas for which 0.1 g kg^{-1} is significantly more than 50% of w prior to trajectory passage. Conversely, a little more than half of the significant drying observed in Figure 20 occurs in areas for which 0.1 g kg^{-1} is less than 50% of w. The greenhouse effect of water vapor is especially sensitive to changes in dry areas, as the water vapor greenhouse parameter is logarithmic in vapor concentration (see Appendix A). Figure 21 indicates relative changes of nearly 300% as the trajectory passes for ambient RH$_i$ ≃20%. As a result, changes in the frequency of occurrence or areal coverage of deep convective detrainment in areas of low

RH_i could have a relatively large impact on the magnitude of the water vapor feedback.

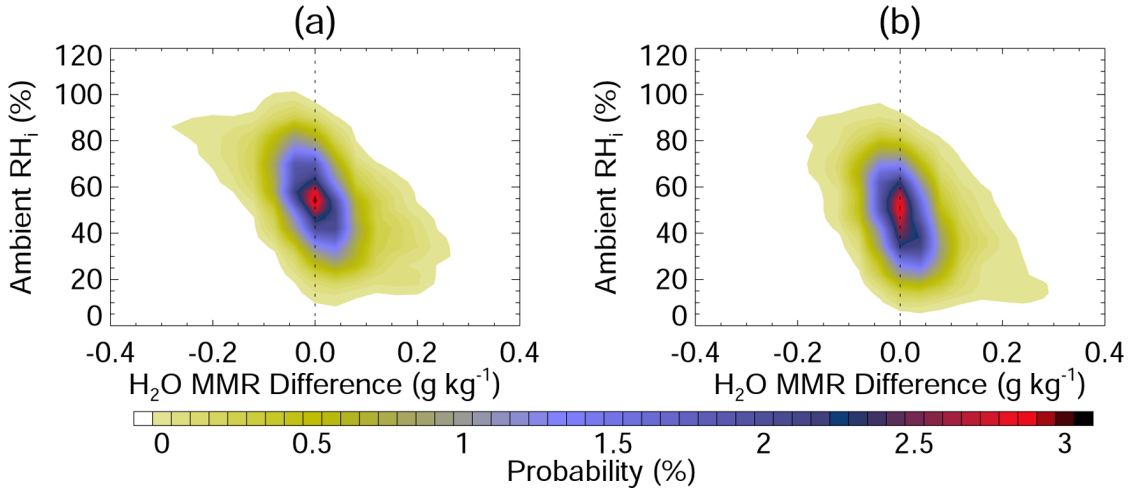

Figure 22: PDF for (a) detrainment from continental convection; (b) detrainment from oceanic convection.

Figure 22 separates the PDF shown in Figure 20 into continental (Figure 22a) and maritime (Figure 22b) convective regimes. While the general distribution is similar to that noted for all tropical convection, a few notable differences are apparent. In particular, the dehydration lobe is more pronounced for trajectories detraining from continental convection (5.2% of cases) than for those originating in maritime convection (3.4%), and continental convection appears to be primarily responsible for the extent of the drying lobe in Figure 20. The moistening lobe is comparable, but also slightly larger for continental convection (8.7% compared to 8%).

This latter relationship is reversed for the normalized PDFs (Figure 23). While the drying lobe is still more expansive for continental convection (2.4% to 1.8%), the hydration lobe is now larger for oceanic convection (15.5% to 14.4%). This relationship indicates that oceanic convection detrains into a generally drier UT, a result that is supported by the relative positions of the PDFs along the ordinate in both Figures 22 and 23, and consistent with the large-scale circulation. Tropical oceanic regions tend to be located within the subsiding branches of the Walker circulation, while continental regimes typically comprise the rising branches. Furthermore, continental convection is typically both deeper and more frequent than oceanic convection (*Petersen and Rutledge*, 2001), which may tend

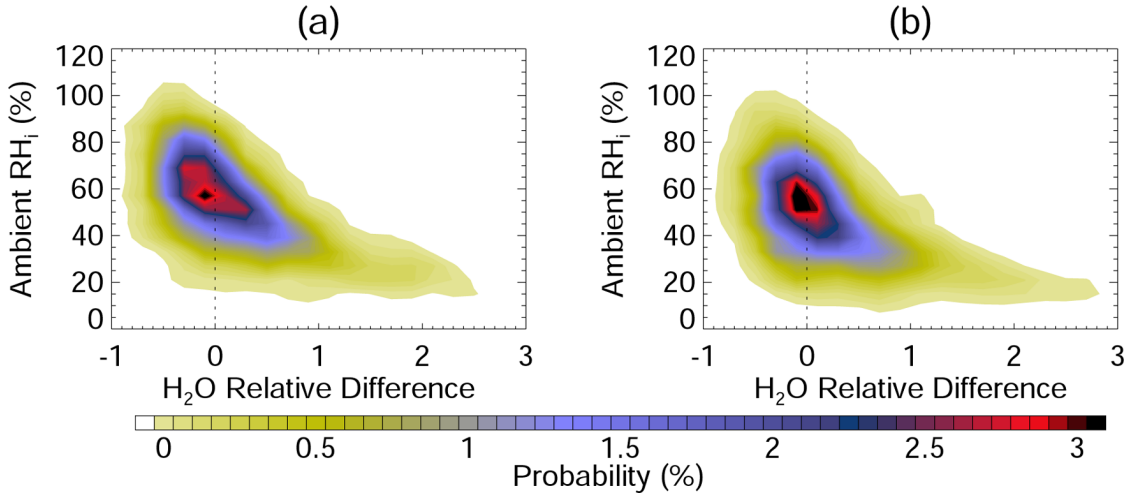

Figure 23: PDF for (a) detrainment from continental convection; (b) detrainment from oceanic convection.

to maintain a higher UTH above the continents.

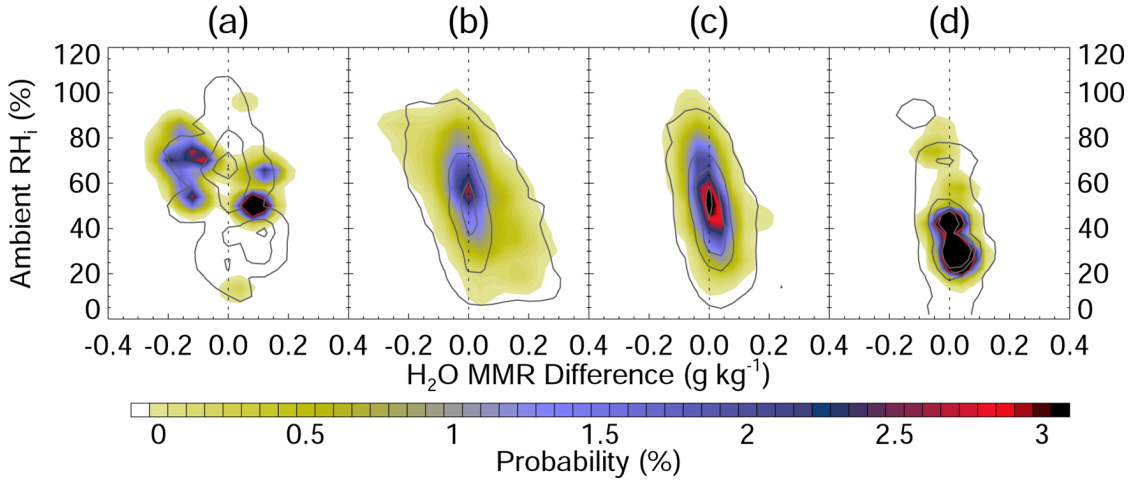

Figure 24: PDFs for trajectories originating with continental convection (filled contours) and oceanic convection (solid gray contours) detraining at (a) $\theta_{det} < 340$ K; (b) 340 K $\leq \theta_{det} < 345$ K; (c) 345 K $\leq \theta_{det} < 350$ K; (d) $\theta_{det} \geq 350$ K. Gray contours are plotted at probabilities of 0.06%, 1%, 2%, and 3%.

The PDFs for continental and oceanic convection are further classified by the potential temperature of detrainment (θ_{det}) in Figure 24 and 25. Figure 24 indicates that the bulk of the lobe structure in Figures 20 and 22 is attributable to detrainment at $\theta_{det} < 345$ K (Figure 24a-b). This result is logical, since saturation mixing ratios decrease by about one order of magnitude with altitude across the 300-200 hPa layer. For continental convection

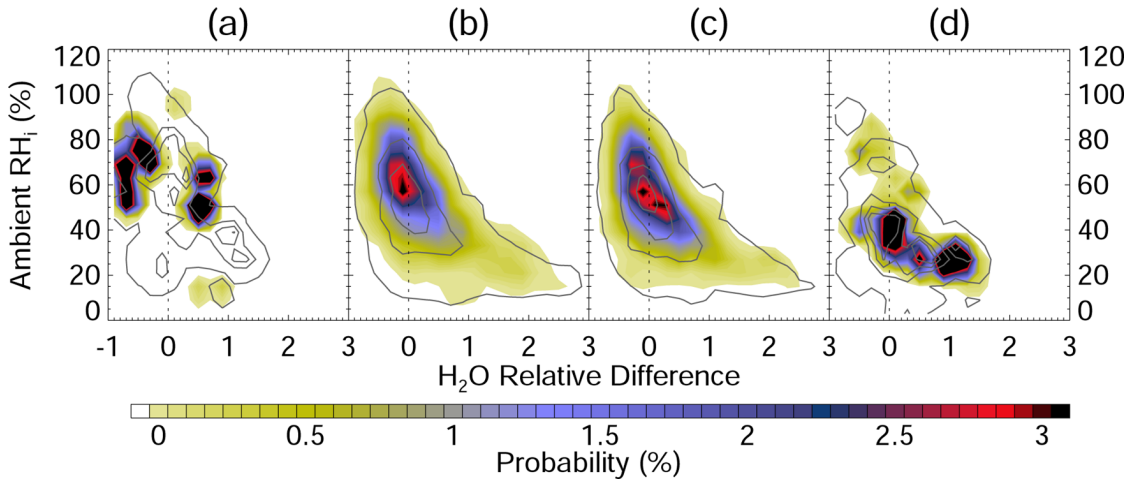

Figure 25: PDFs for trajectories originating with continental convection and detraining at (a) $\theta < 240$ K; (b) 240 K $\leq \theta < 245$ K; (c) 245 K $\leq \theta < 250$ K; (d) $\theta \geq 250$ K.

(filled contours), 43% of cases with $\theta_{det} < 340$ K (Figure 24a) dehydrate by more than 0.1 g kg^{-1}, while 18% hydrate by more than that amount. The absolute influence of oceanic convection (solid gray contours) at this detrainment level is much less (4.6% and 13.9%, respectively).

The normalization of the abscissa for the PDFs in Figure 25 controls for the temperature dependence of saturation mixing ratio with height. Continental convection that detrains into the 300-200 hPa level at higher altitudes ($\theta_{det} \geq 350$ K; Figure 25d) constitutes a significant moisture source, with 36.8% of the total events leading to a water vapor increase of more than 50%, primarily in air with a low ambient RH$_i$, and only 0.6% leading to a decrease of more than 50%. Conversely, continental convection detraining at lower altitudes ($\theta_{det} < 340$ K; Figure 25a) represents a net moisture sink (28.8% dehydrate; 13.3% hydrate). Both levels in between are net moisture sources, with approximately 14% of cases leading to hydration and about 1-3% leading to dehydration. Oceanic convection constitutes a net moisture source throughout the analyzed detrainment profile, with the hydration lobe between 15-23%, and the dehydration lobe between 1-4%. All of the PDFs shown in Figure 25 have essentially the same qualitative shape except for the continental PDF in panel (a).

The exact mechanism responsible to the observed strong dehydration due to detrainment from $\theta_{det} < 340$ K remains in doubt; however, we propose that the explanation first

presented in Section 3.1 also fits here. To recap, the melting or evaporation of ice during precipitation results in latent cooling, which in turn leads to the formation of significant unsaturated downdrafts (*Squires*, 1958; *Emanuel*, 1994). These downdrafts could swiftly dehydrate the air detraining from convection (*Tompkins and Emanuel*, 2000; *Held and Soden*, 2000), and could lead to dehydration such as that observed in Figure 24a. In order for this mechanism to be relevant in the 300-200 hPa layer, sufficient phase changes must be occurring in precipitation as it falls through these levels. This requires that large quantities of precipitation-sized hydrometeors must exist in the anvil cloud above the detraining layer; that is, above $\theta = 340$ K. Continental convection is usually deeper and more vigorous than oceanic convection, and frequently exhibits larger radar reflectivities at altitudes of 12-15 km and above (cf. Figure 7; *Petersen and Rutledge*, 2001), potentially priming the environment for such downdrafts.

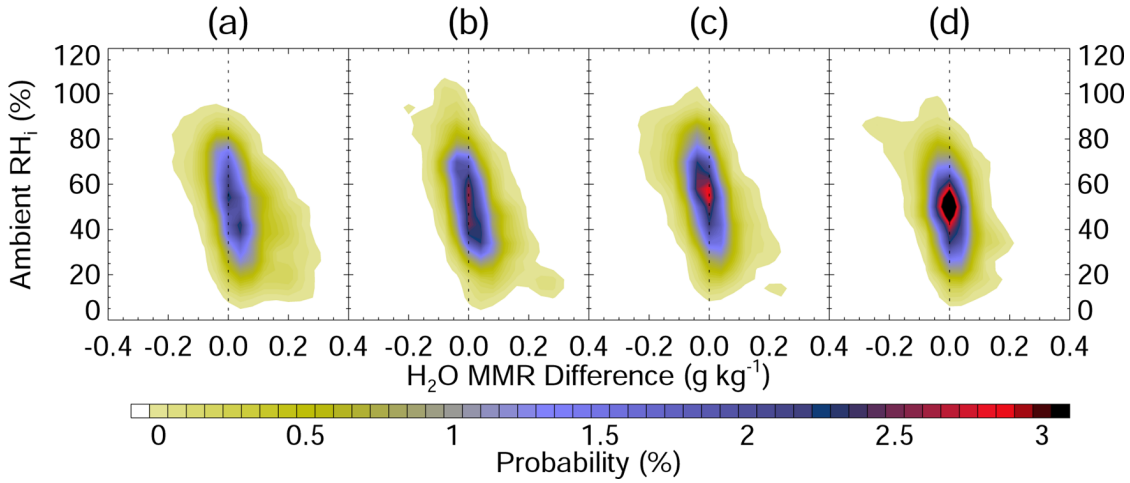

Figure 26: As in Figure 20, but for lag time following convection of (a) 0-12 hours, (b) 12-18 hours, (c) 18-24 hours, and (d) 24-36 hours.

The time evolution of the RH$_i$-Δw relationship is investigated in Figure 26. The moistening lobe is maximized ($\sim$16.8%) shortly following convection (within 0-12 hours; Figure 26a). and then decreases in size monotonically through hour 36 (4%; Figure 26d). The drying lobe is at a minimum in close temporal proximity to convection (0.6%), and appears to maximize at a lag time of about 18-24 hours following convection (3.2%; Figure 26c). Since both the hydration and dehydration lobes decrease between the 18-24 hour PDF and

the 24-36 hour PDF (Figure 26c-d), and essentially disappear afterward (not shown), we identify 36 hours as the approximate limit of the RH_i-Δw relationship.

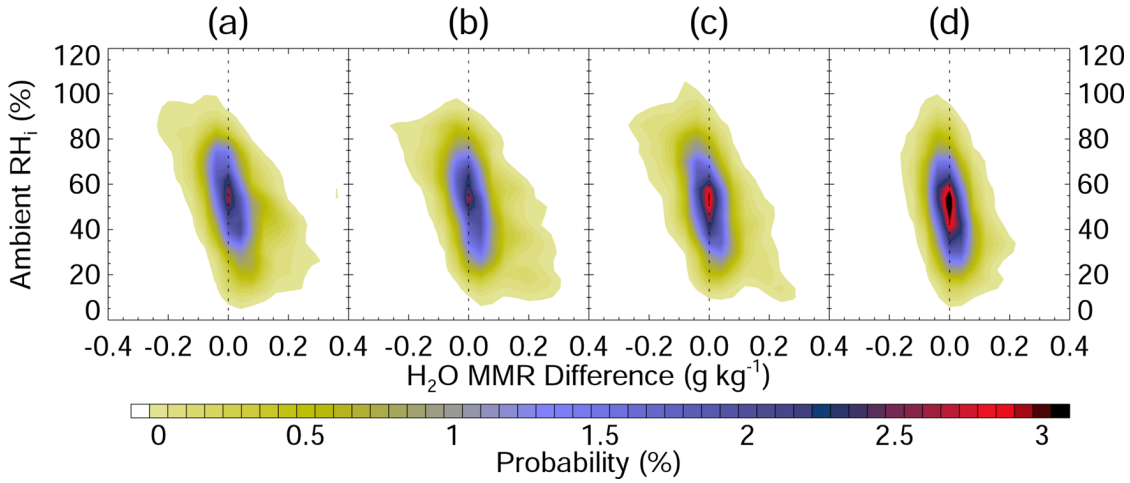

Figure 27: As in Figure 20, but for travel distances from convection of (a) 100-200 km, (b) 200-400 km, (c) 400-600 km, (d) greater then 600 km.

PDFs arranged by increasing distance from convection (Figure 27) evolve similarly. Here we do not show the first PDF (0-100 km), but begin at a travel distance of 100-200 km from the convective origin (Figure 27a). We then proceed through travel distance bins of 200-400 km, 400-600 km, and $\geq$ 600 km. Distance along the trajectory is calculated by iterating Vincenty's inverse formula (see Appendix B *Vincenty*, 1975), and is integrated piecewise by timestep. As in Figure 26, the hydrating lobe shrinks monotonically with distance from convection, and the drying lobe peaks at around 400-600 km. For distances greater than 600 km, the distribution is fairly neutral, with the hydrating and dehydrating lobes comprising 4.6% and 2.5%, respectively. As we will show in Section 4.3, the size of the hydrating lobe is comparable to that of the global tropics, regardless of whether the observation is linked to convection. Accordingly, we estimate the spatial limit of the RH_i-Δw relationship to be about 600 km.

4.2 Impact of Ice

The two limiting thresholds identified in Section 4.1 have some basis in the existing literature. In particular, *Luo and Rossow* (2004) identified the lifetimes of detrainment cirrus at about 19-30 $\pm$ 16 hours, and estimate that they can advect up to 1000 km during their

lifetime. These results further characterize the relationship between the detrainment of condensate from convective towers and the water vapor distribution. In particular, convective detrainment is observed to be a net source through nearly all of the conditions presented here, although the magnitude of the source wanes with time and distance from convection. Furthermore, the dehydrating impact of the detrainment appears to maximize at a lag time of about 18-24 hours following convection. It is not possible to distinguish precisely which aspects of the relationship presented here are due to water vapor advection, and which are due to the presence of ice; however, we can examine how the relationship is modified when we classify the convective source according to the estimated ice water content (IWC) and ice cloud effective radius r_{ei}.

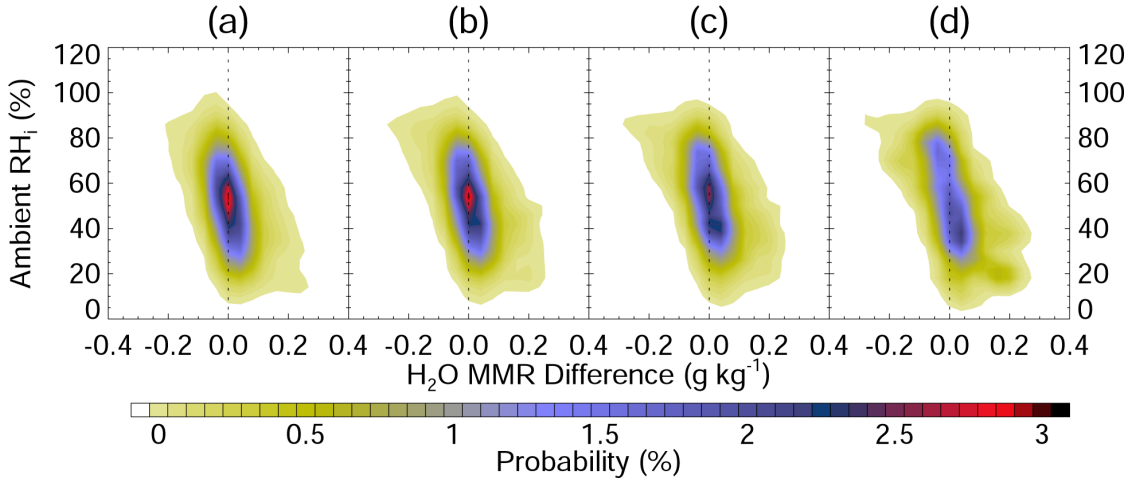

Figure 28: As in Figure 20, but for (a) IWC $\leq$ 2 g m^{-3}; (b) 2 g m^{-3} $<$ IWC $\leq$ 3 g m^{-3}; (c) 3 g m^{-3} $<$ IWC $\leq$ 4 g m^{-3}; and (d) IWC $>$ 4 g m^{-3}

Figure 28 shows PDFs for convective IWC bins ranging from relatively small (IWC $\leq$ 2 g m^{-3}; Figure 28a) to large (IWC $\geq$ 4 g m^{-3}; Figure 28d). The sizes of both lobes increase monotonically with IWC (8.1%-12.9% for the hydration lobe; 4%-6.5% for the dehydration lobe), and the ratio of hydration lobe to dehydration lobe remains relatively constant at around 2. This result highlights the competition between the moistening and drying roles of ice as discussed in Chapter 3, which we will now recap. At low RH_i, ice can sublimate and moisten the ambient environment; conversely, at high RH_i, ice particles

serve as condensation nuclei, lowering the microscale saturation vapor pressure and condensing water vapor out of the ambient environment (*Emanuel*, 1994). The reduction of ice water content due to sedimentation along a trajectory can be modeled using an e-folding time (*Dessler and Sherwood*, 2000; *Gettelman et al.*, 2002). If we assume that this e-folding time is constant across the range of IWCs considered here, which essentially amounts to an assumption that the particle size distributions are identical, an assumption that has already been incorporated into the calculation of IWC via equation (1), then a larger IWC at the source corresponds to a larger IWC downstream. A larger IWC downstream means more ice to either hydrate or dehydrate the ambient environment, thus the constant e-folding time assumption is supported by the results that are summarized in Figure 28.

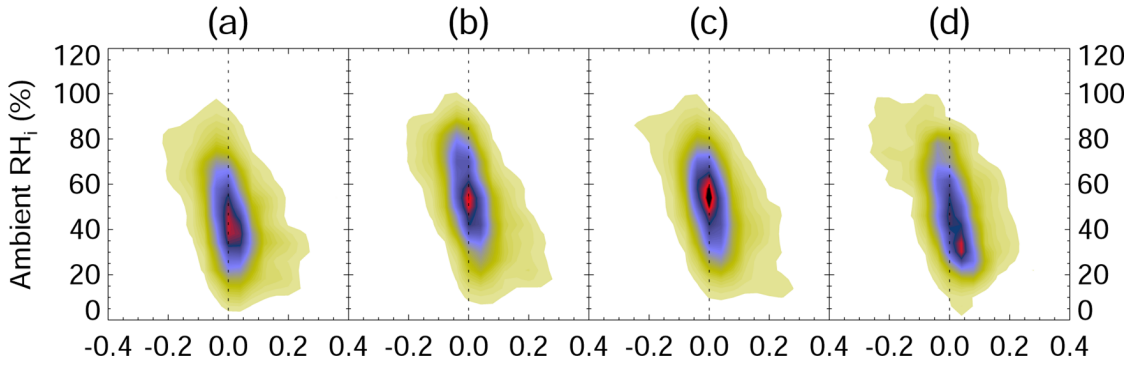

Figure 29: As in Figure 20, but for (a) $r_{ei} \leq 15$ μm; (b) 15 μm $< r_{ei} \leq 25$ μm; (c) 25 μm $< r_{ei} \leq 35$ μm; and (d) $r_{ei} > 35$ μm

Figure 28 shows PDFs for r_{ei} bins ranging from relatively small ($r_{ei} \leq 15$ μm; Figure 29a) to relatively large ($r_{ei} \geq 35$ μm; Figure 28d). The results indicate generally good agreement with the relationships presented in Chapter 3. The dehydration lobe is observed to be largest for $r_{ei} \geq 35$ μm (5%), and nearly as extensive for 15 μm $< r_{ei} \leq 25$ μm (4.7%; Figure 28b). We note that the moistening lobe is largest for the smallest size bin (9.1% of the total cases, compared to about 8% for the other three size bins). The moistening lobe for all tropical convective detrainment (Figure 20) is also approximately 8%, suggesting that detrainment particle size distributions that are skewed toward very small ice may have a net moistening effect on the downstream environment. This result is not overly surprising, as a growing body of literature suggests that this relationship exists in both the physical

atmosphere and global climate models (e.g., *Sherwood*, 2002; *Del Genio et al.*, 2005).

4.3 Comparison with the Global Tropics

In order to interpret these results, it is helpful to have some knowledge of the reference atmosphere; that is, what is the relative role of convective detrainment in determining water vapor changes in the entire global tropical UT, not solely in the convective areas? This is accomplished by aggregating RH_i and w into 1°× 1° bins and computing the daily means. We then identify every gridbox in the tropics (15°S- 15°N) for which we have data on successive days between January 1 and January 31, 2004, The ambient relative humidity is considered to be the mean RH_i on the first day, and Δw is the change in w between day 1 and day 2. For instance, if data exists in a given gridpoint for both January 1 and January 2, then the ambient relative humidity is RH_i on January 1, while Δw is the difference between the mixing ratio on January 2 and the mixing ratio on January 1.

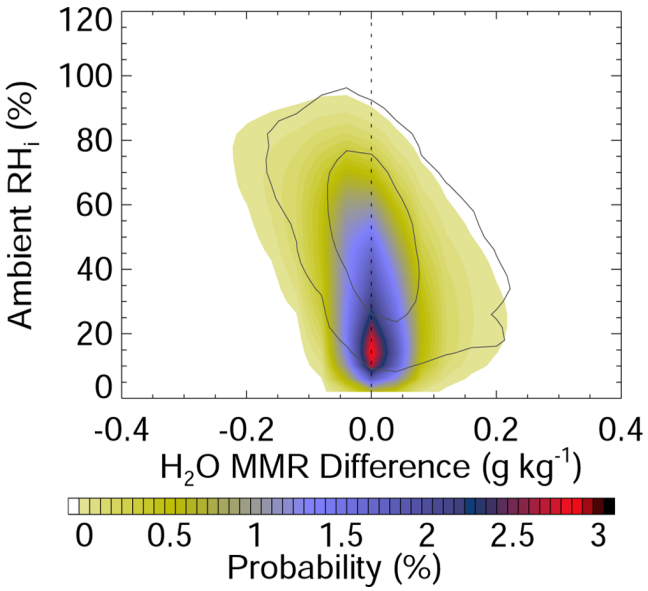

Figure 30: As in Figure 20, but for the global tropics regardless of whether or not convection has occurred. .1% and 1% probabilities from Figure 20 are overplotted as gray contours.

Figure 30 displays the PDF of the RH_i-Δw relationship for the global tropics (filled contours), and plots the PDF when the parcel is linked to convection (Figure 20) as an overlay (solid gray contours). In this case the strong hydration and strong dehydration lobes exhibit nearly identical probability, although the dehydration lobe is slightly more

extensive than the hydration lobe. Specifically, 5.9% of cases dehydrate by more than 0.1 g kg^{-1} while 5.4% of cases hydrate by more than that amount.

The shift toward additional drying relative to the cases that are linked to convection can be understood in terms of the simple conceptual model of UTH presented in Chapter 1. To recap, deep convection constitutes the source of water vapor, and subsidence provides the sink. The rightward shift of the PDF when only convective cases are considered represents the moistening of the UT through the convective detrainment of water vapor and ice. The leftward shift when all cases are considered then represents the sink, as water vapor subsides out of the 300-200 hPa layer and is replaced by relatively dry air from above. In other words, if the location we observe has been influenced by convective detrainment within the previous day or so, it is more likely to fall in the rightmost portion of the PDF, and the converse is true for air that has not recently been influenced by convective detrainment.

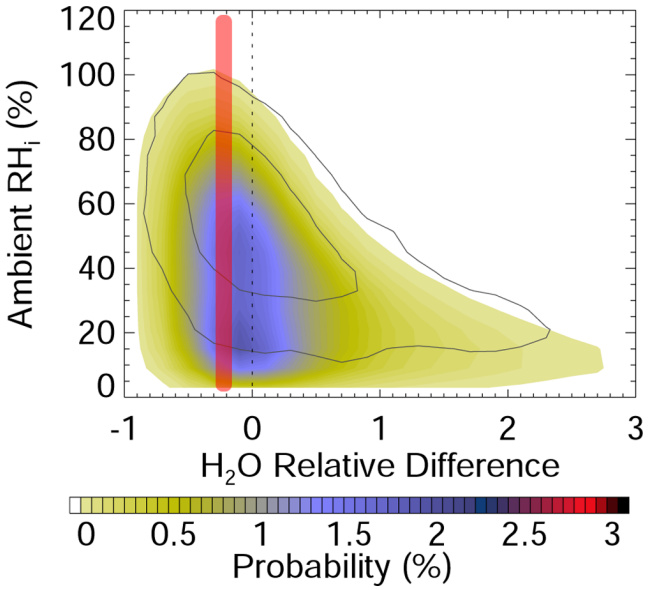

Figure 31: As in Figure 21, but unlinked to convection. The translucent red area depicts the relative change in mixing ratio that would be expected from a subsidence rate of 10 hPa day^{-1} and a constant RH_i throughout the layer.

This can be further understood by examining the PDF derived from the normalized Δw (Figure 31). Again, the convective lobe is visible via the overlay. Outside of that lobe, we see a tendency for a decrease in water vapor mass mixing ratio of about 10-30%. For reference, this is roughly consistent with assuming a constant vertical distribution of relative humidity

and a subsidence rate of about 10 hPa day^{-1} at the lapse rate suggested by Figure 9 ($\Gamma \sim$0.25 K hPa^{-1}). The relative change in mixing ratio according to these assumptions is depicted by the translucent red area. These results are generally in accordance with the analysis of *Mapes* (2001), who showed that radiative cooling alone can account for humidity in the 300-200 hPa layer decreasing by up to 50% in one day.

4.4 Potential Applications

Most current climate models do not parameterize the evolution and microphysics of convective detrainment, and the impact of detrained ice on the water vapor distribution is largely unaccounted for. The results presented in this chapter provide the potential framework for a probabilistic and prognostic assessment of the change in water vapor downstream from tropical convection. With additional investigation of the joint probability densities and seasonal variability, the method could be developed to provide a useful observational constraint on climate model parameterizations of convective detrainment. In particular, a comparison of observed and simulated PDFs of downstream water vapor change could assist with the identification of specific sources of error through a range of convective vertical and microphysical variability. The results have been developed using a data set that appears to be well characterized (*Gettelman et al.*, 2004; *Hagan et al.*, 2004; *Fetzer et al.*, 2005), and evaluation against the background relationship (cf. Figures 20 and 30) indicates that the derivation is robust.

CHAPTER V

EVALUATION OF AN ADVECTION-CONDENSATION MODEL

The term advection-condensation model refers to a class of simple models in which the humidity at a given location is assumed to be a function of its last previous saturation. These models have recently gained widespread use for modeling the water vapor distribution in the tropical and subtropical UT (e.g., *Yang and Pierrehumbert*, 1994; *Sherwood*, 1996b; *Salathè and Hartmann*, 1997; *Pierrehumbert*, 1998; *Pierrehumbert and Roca*, 1998; *Dessler and Sherwood*, 2000, 2004; *Minschwaner and Dessler*, 2004; *Pierrehumbert et al.*, 2006), and have also been adapted to non-Lagrangian frameworks (*Galewsky et al.*, 2005). The clear dependence of UTH downstream from convection on detrainment and trajectory temperature, and the relatively small influence of cloud ice properties observed in Chapters 3 and 4 suggest that such a model should capture well the evolution of convective detrainment in the global tropics. Here, we examine how water vapor observations along the trajectory compare to contemporaneous humidity estimated using an advection-condensation model, and investigate the source and solutions to the observed discrepancies.

5.1 Comparison with Observations

A large part of the attraction of advection-condensation models is their ability to characterize the horizontal distribution of UTH in a qualitatively accurate way with minimal computational expense. The formulation of the model used here is exceedingly simple, and is described in Section 2.2.3. As in previous sections, all analyses are conducted only for trajectory points that have both observational and modeled humidities.

As in previous works (e.g., *Yang and Pierrehumbert*, 1994; *Pierrehumbert and Roca*, 1998; *Dessler and Sherwood*, 2004; *Minschwaner and Dessler*, 2004, and others), we find that our model adequately captures the qualitative nature of the general UTH distribution

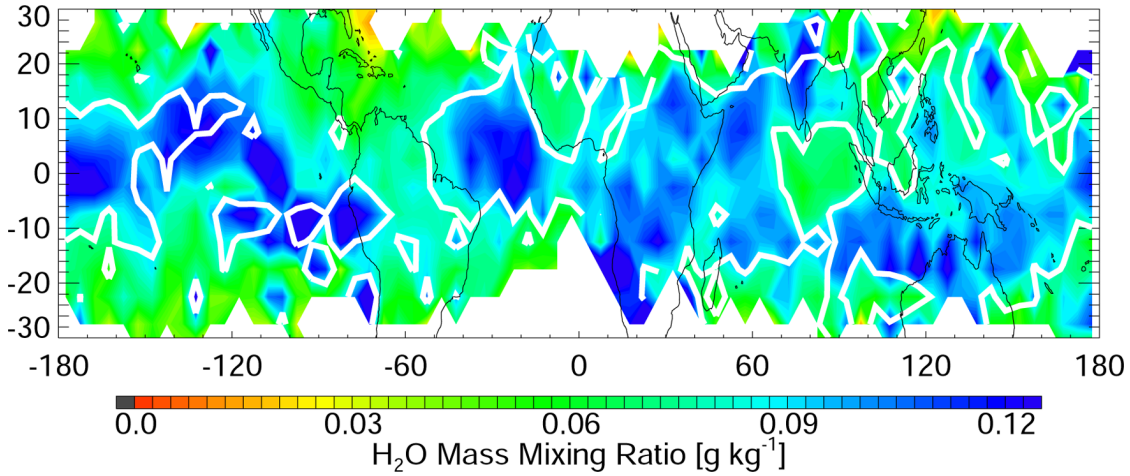

Figure 32: Composite map of AIRS observations connected via trajectory integration to TRMM PR (filled contours) and 0.2 g kg^{-1} contour calculated by the advection-condensation model (thick white contour).

(Figure 32). A closer examination, however, reveals that the 0.2 g kg^{-1} contour from the model composite mean roughly corresponds to the 0.09-0.1 g kg^{-1} contour in the observational composite mean, suggesting that the model is overestimating the humidity by about 100%.

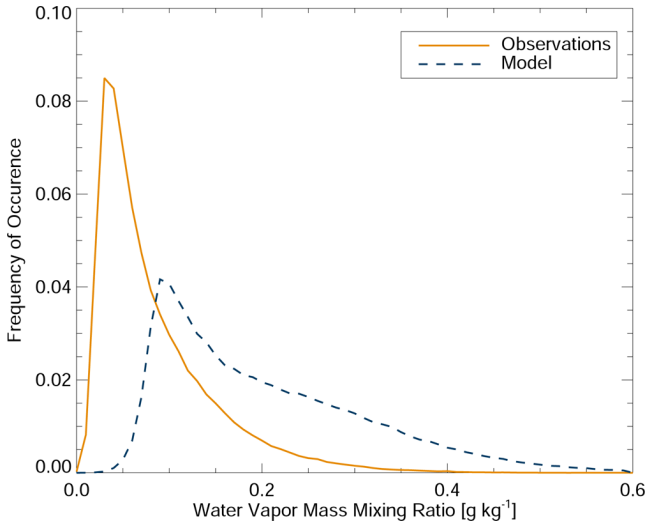

Figure 33: Histograms of water vapor mass mixing ratio for both AIRS observations (solid orange curve) and the advection-condensation model (dashed blue curve).

The model overprediction is further examined in Figure 33, which depicts histograms of water vapor mixing ratio for both the observations (solid orange curve) and model (dashed blue curve). A comparison of these two curves clearly shows that the model is consistently

overpredicting the humidity by a considerable margin. This overprediction is consistent throughout the trajectory evolution (Figure 34), and in fact the discrepancy between the histogram peaks grows slightly with lag time. This latter result implies that the model is inadequately characterizing the processes that control dehydration.

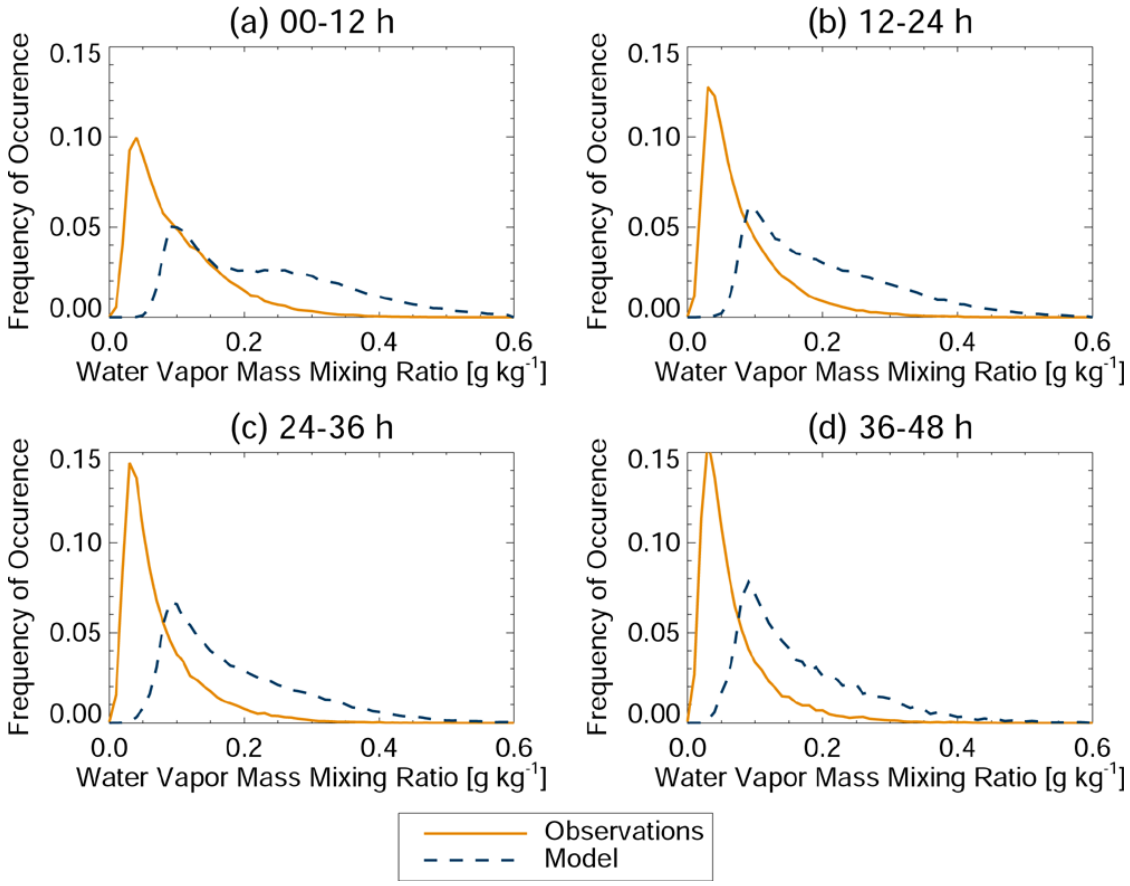

Figure 34: As in Figure 33.

The discrepancy noted above could result from several factors. First, the observations could be too dry. We suspect that this is not the case, based on the existing validation (*Gettelman et al.*, 2004; *Hagan et al.*, 2004; *Fetzer et al.*, 2005). Second, we have not accounted for any mixing that may take place along the trajectory. Such processes were investigated along Lagrangian trajectories by (*Pierrehumbert and Yang*, 1993), but for the time scales of this trajectory integration (∼48 hours) we consider them to be relatively inconsequential. Third, we have assumed in this model formulation that condensation only takes place once

the water vapor mixing ratio exceeds the saturation mixing ratio—that is, that condensation takes place at $RH_i \geq 100\%$. This assumption is questionable for two reasons: i) it does not take into account the fact that microphysics operate on a microscale, and that condensation may in fact be taking place in our parcel even when the RH_i of the observed volume is significantly less than 100%; and ii) it does not consider the possibility that detrainment may exit convection at subsaturated levels (*Tompkins and Emanuel*, 2000). Furthermore, we have neglected the potential role of ice in hydrating or dehydrating the parcel. Although we have shown in Chapters 3 and 4 that this influence is of higher order, our results do indicate that the relationships are observable. Finally, the model can only be as accurate as the temperature field that drives it. Anomalously warm temperatures have been noted in reanalyses near the tropical tropopause (*Stendel and Arpe*, 1997; *Trenberth et al.*, 2001; *Randel et al.*, 2000). In addition, convection is known to excite internal gravity waves in the UT (e.g., *Lane and Reeder*, 2001), which would perturb the temperature field at scales smaller than those resolvable by the reanalysis model.

In the following sections, we first investigate the agreement between the model and the observations according to detrainment temperature, detrainment ice water content, and ice cloud effective radius. These latter comparisons provide a stepping point from which to examine the sensitivity of the model to condensation levels and variations in the temperature field.

5.1.1 Detrainment Temperature

Figure 35 illustrates the probability of finding a certain water vapor mixing ratio downstream from convection (abscissa) given a detrainment temperature (ordinate) at lag times of (a) 0-12 hours, (b) 12-24 hours, (c) 24-36 hours, and (d) 36-48 hours. PDFs are shown for AIRS observations (filled contours) and model (solid gray contours), and are computed as described in Section 2.4. The qualitative agreement between the model and observation PDFs illustrates the benefits of using AIRS water vapor at the support product levels for this analysis and that presented in Chapter 3. If water vapor is used on the standard product levels instead, this distribution appears as a formless blob (not shown).

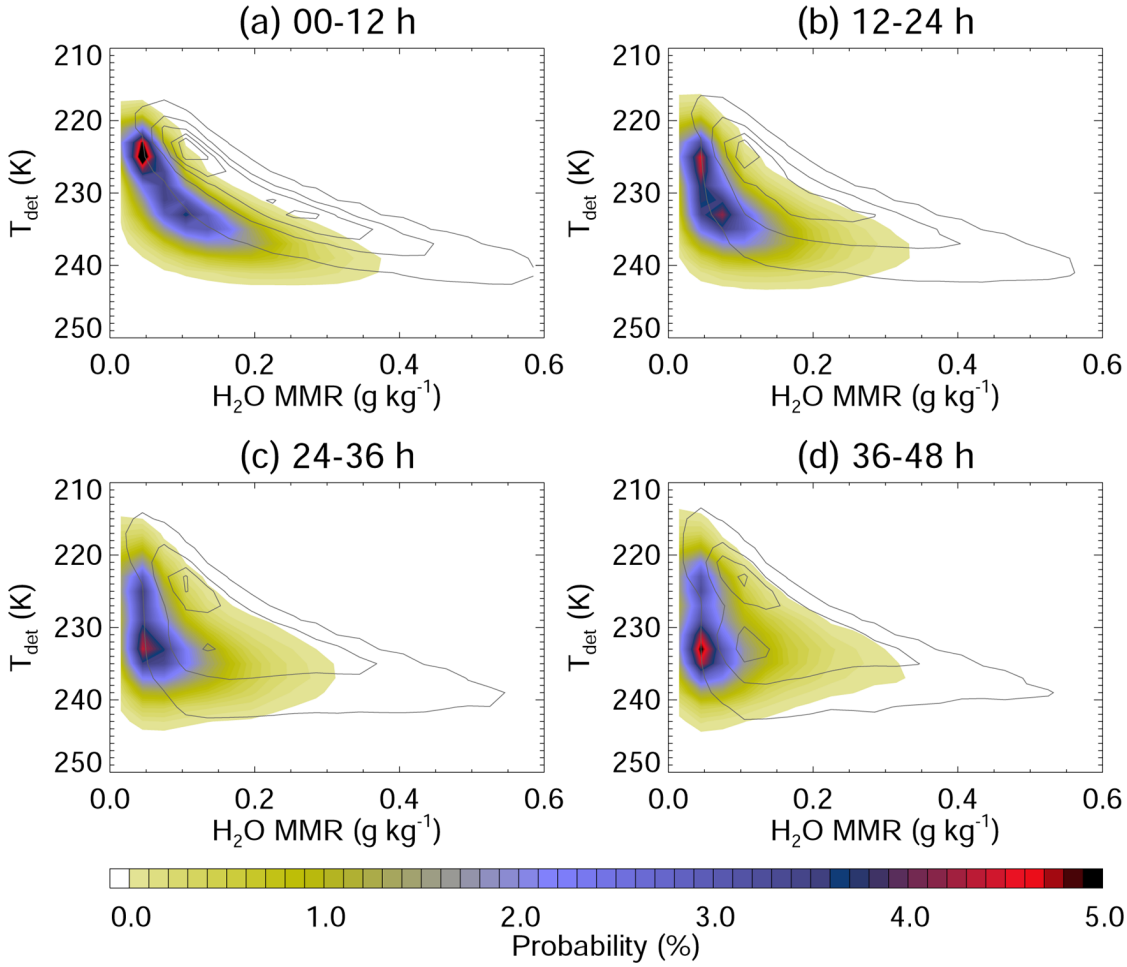

Figure 35: PDFs of detrainment temperature vs. water vapor mass mixing ratio for AIRS observations (filled contours) and model simulations (solid gray contours) for lag times of (a) 0-12 hours; (b) 12-24 hours; (c) 24-36 hours; and (d) 36-48 hours. Model simulation contours are plotted at 0.1%, 1%, 2% and so on up to a maximum of 5%.

In addition, we find that the model overprediction of humidity persists throughout the detrainment profile, While the disagreement is fairly equally distributed in detrainment temperature near the beginning of the trajectory (0-12 hours; Figure 35a), the bulk of the discrepancy further into the trajectory (Figures 35b-d) is attributable to air detraining at higher (lower) detrainment temperatures (altitudes), while the agreement between model and observations at lower (higher) detrainment temperatures (altitudes) improves with lag time from convection. This allows us to further pinpoint the primary source of the discrepancy, since it indicates that the model is less adept at characterizing the processes

controlling dehydration at lower detrainment altitudes. Furthermore, it suggests that large-scale temperature along the trajectory plays a dominant role in determining the downstream water vapor at higher detrainment altitudes (∼250-200 hPa).

5.1.2 Cloud Ice Parameters

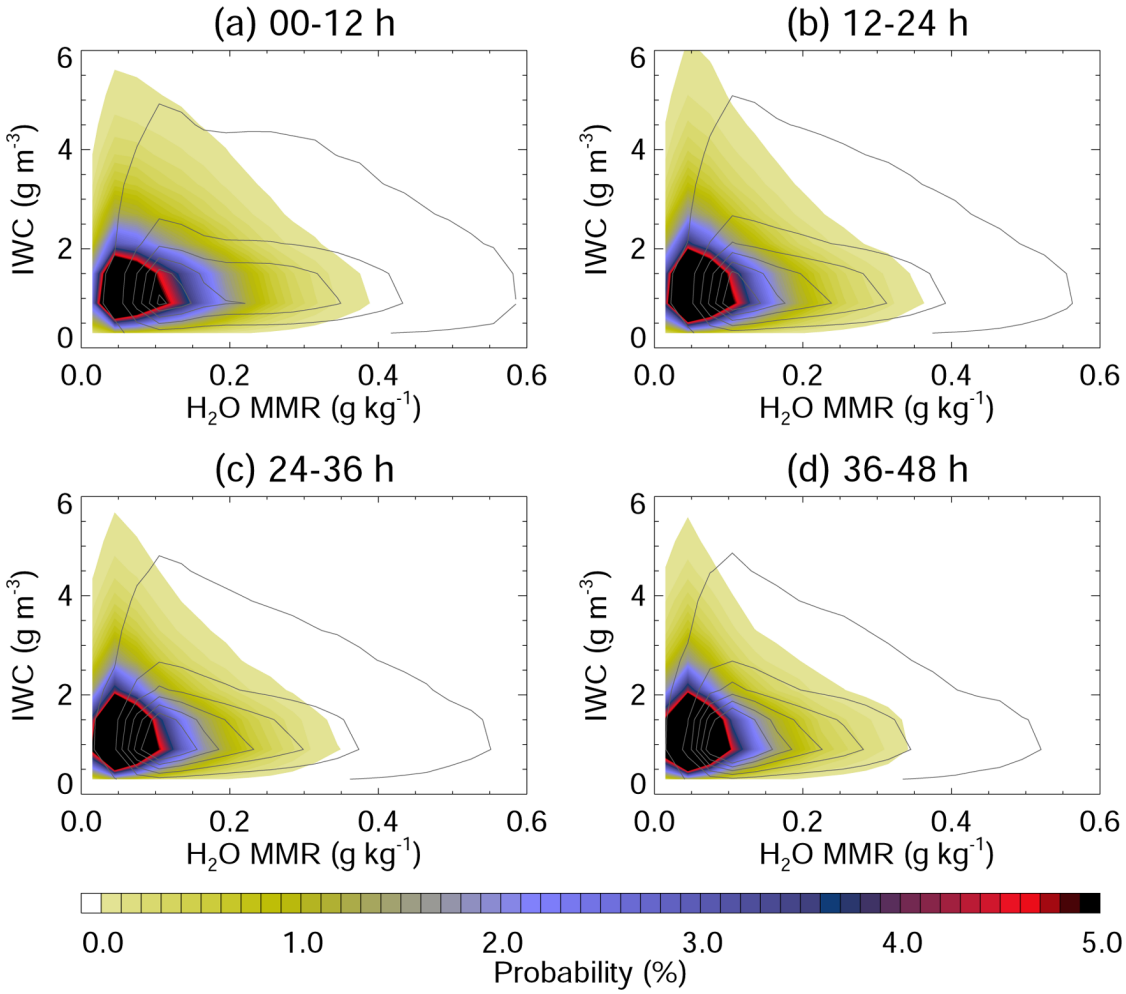

Figure 36: As in Figure 35, but for IWC rather than detrainment temperature.

Figures 36 and 37 show the PDFs of downstream water vapor for IWC and r_{ei}, respectively. PDFs based on AIRS observations are again depicted as filled contours, while PDFs based on model simulated humidity are shown as solid gray contours. The bulk of the discrepancy in Figure 36 is observed at low IWC; however, we find that as the trajectory evolves, the agreement between model and data grows at these IWCs, while the converse is

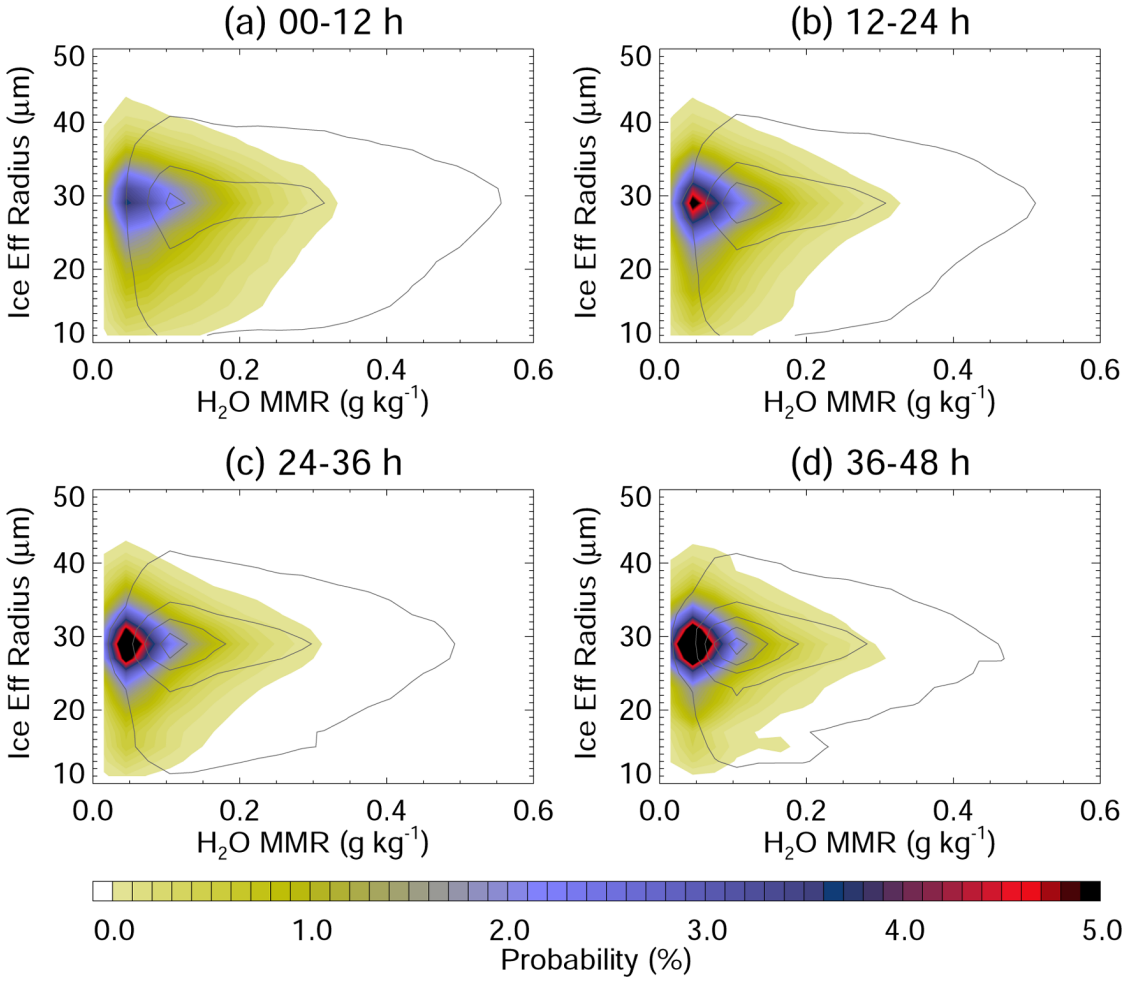

Figure 37: As in Figure 35, but for ice cloud effective radius rather than detrainment temperature.

true for high IWCs. Together with the conclusion of Section 5.1 that the bulk of the discrepancy is due to inadequate characterization of dehydration processes, this result indicates that at least a portion of the discrepancy between the data and the model is attributable to the neglect of the dehydrating influence of ice in the model. A similar conclusion is drawn by examining Figure 37. In Section 3.1.2, normalized dehydration rates were observed to be minimum for middle ($\sim$28 μm), and highest for r_{ei} at the high and low ends of the spectrum (r_{ei} $\leq$20 μm and r_{ei} $\geq$35 μm. Accordingly, the discrepancy between the model and the data is observed to grow with lag time from convection at the high and low ends of the r_{ei} spectrum, while agreement appears to remain relatively constant in the middle of the spectrum.

As in Section 5.1.1, the similarity of the qualitative shapes of the distributions is remarkable. As the model knows nothing of about ice except for whatever representation filters through in the large-scale temperature field, this further underscores the higher-order nature of the relationship between these two ice cloud properties and downstream humidity. In addition, it indicates that the biases in the model are relatively independent of if IWC and r_{ei}, suggesting that the lack of accurate microphysics is not the primary root of the discrepancy.

5.1.3 Sensitivity to Condensation Threshold

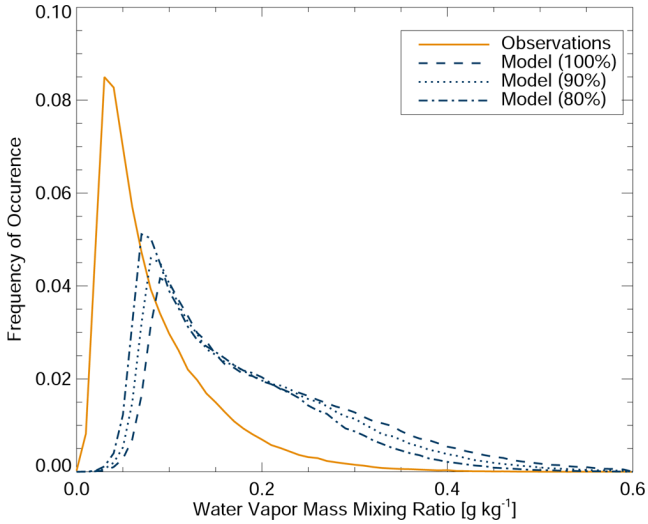

Figure 38: As in Figure 33, but adding histograms for the model using condensation levels of 90% (blue dotted curve) and 80% (blue dash-dot-dot-dot curve) of saturation.

The model operates based on condensation, a microscale process, while the observations are retrieved for a volume on order of 10^3 km^3 and the large-scale temperature distribution for a volume on order of 10^5 km^3. Therefore, we must account for the possibility that saturation may be taking place somewhere in the represented volume, even though the precise trajectory point is subsaturated. Typically, this is accounted for by reducing the condensation threshold of the model from 100% to 90% (e.g., *Sherwood*, 1996b; *Galewsky et al.*, 2005). Figure 38 illustrates how the histograms for model condensation thresholds at 100% (blue dashed curve), 90% (blue dotted curve), and 80% (blue dash-dot-dot-dot curve) correspond to the observational values (orange solid curve). Although the distributions

can be seen to converge slightly to the observed histogram as the condensation threshold is lowered, this factor does not appear able to account for much of the discrepancy by itself. In fact, the condensation threshold would have to be lowered to 50% (Figure 39), a physically unreasonable assumption, in order to achieve a good quantitative agreement between the model and the data.

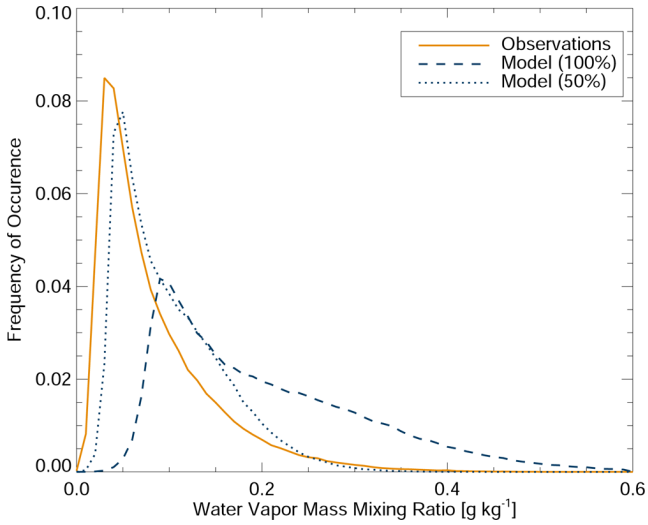

Figure 39: As in Figure 38 but for a condensation level at 50% of saturation.

5.2 Temperature Distribution

To summarize, a portion of the discrepancy may be attributable to the role of ice, and a portion to the physical realism of the condensation threshold. Neither of these effects seems adequate to explain the entire discrepancy, however. As a result, we examine the whether the temperature field is inadequate to the task at hand. Possible errors in the large-scale temperature distribution are explored, and the impact of imposing a small-scale temperature perturbation generally consistent with convectively generated gravity waves is explored.

5.2.1 Impact of Assimilating AIRS Temperatures

Several studies have shown that reanalysis temperatures near the tropopause may be systematically too warm (*Stendel and Arpe*, 1997; *Trenberth et al.*, 2001; *Randel et al.*, 2000). The AIRS instrument appears to be able to retrieve temperature to good accuracy in the

UT (*Gettelman et al.*, 2004; *Fetzer et al.*, 2005), and thus provides a useful tool for comparison with the UKMO reanalysis temperature field. Here we use the gridded and averaged Level 3 Standard Product, which is reported on a 1°×1° grid on time scales ranging from one day to one month. The annual mean AIRS temperature is computed by combining the monthly mean products for the whole of 2004, while the annual mean UKMO temperature is calculated by averaging the daily reanalysis product for 2004.

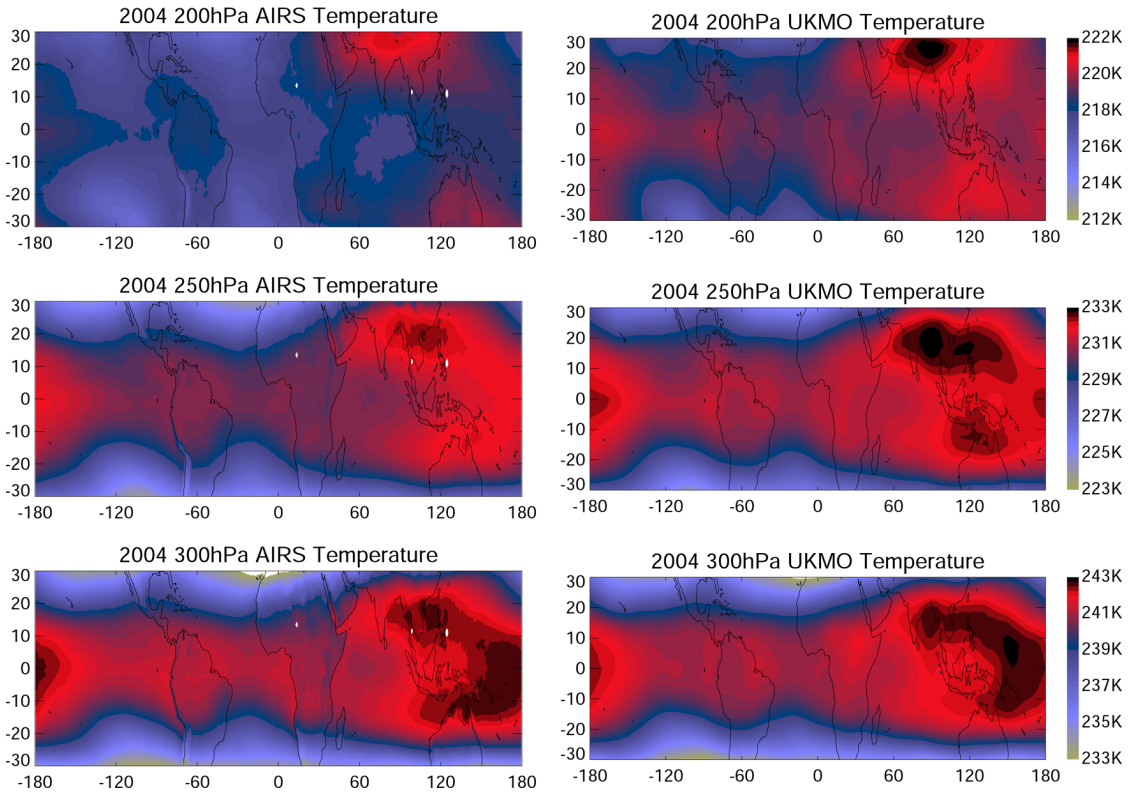

Figure 40: Comparison of UKMO and AIRS annual mean temperature fields.

Figure 40 shows a comparison of the annual mean temperatures at 200 hPa, 250 hPa, and 300 hPa in the tropics. The UKMO temperature is generally warmer than the AIRS temperature. We thus choose to investigate the sensitivity of the model simulation to a crude temperature assimilation. If the AIRS Level 3 daily mean temperature is available for the gridbox containing the trajectory point, we interpolate the AIRS temperature vertically to the trajectory point and store it in place of the UKMO value. If the AIRS temperature is unavailable or does not pass quality control, then we retain the UKMO temperature at that trajectory point. The vertical resolution of AIRS in the UT is similar to that of the

UKMO reanalysis, and the horizontal resolution is improved.

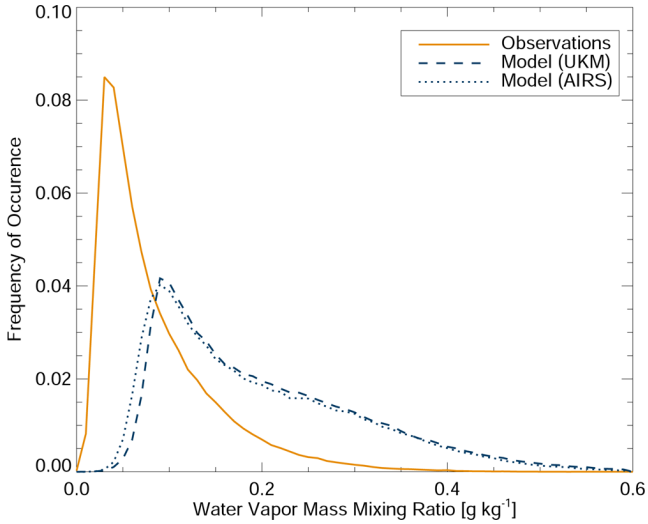

Figure 41: As in Figure 33, but adding the water vapor mass mixing ratio histogram computed by the model after AIRS temperatures are assimilated.

The water vapor mixing ratio histogram calculated from the resulting model is shown in Figure 41 (blue dotted line). As in Figure 38, the model shows some small improvement, but not enough to account for the discrepancy.

5.2.2 Impact of Imposing Sub-Scale Temperature Fluctuations

Convectively forced internal gravity waves can exert a strong influence on the convective environment (e.g., *Mapes*, 1993; *Lane and Reeder*, 2001), and are likely to induce fluctuations in the temperature and vertical velocity fields. Similar perturbations have been shown to be an important prerequisite to accurate simulations of the dehydration of air in the extratropical UT and tropical tropopause layer (e.g., *Jensen and Pfister*, 2004; *Hoyle et al.*, 2005). These perturbations are thought to have less impact in the tropical UT, since the static stability parameter in this region is typically near zero, providing a damping parameter on buoyancy oscillations. However, convection provides a heating source, a dynamical forcing, and a large amount of water vapor, the totality of which is sufficient to overcome this damping.

We apply a general temperature perturbation broadly consistent with the observed properties of convectively generated internal gravity waves. The formulation is given in

Section 2.2.4. The resulting model simulation of humidity is only a slightly better fit (Figure 42). It is entirely possible that our formulation does not realistically consider the temperature perturbation due to convectively excited buoyancy oscillations; however, even if we are underestimating the temperature perturbation by 2 or 3 K, it is unlikely that we will be able to make up the difference using a temperature perturbation alone.

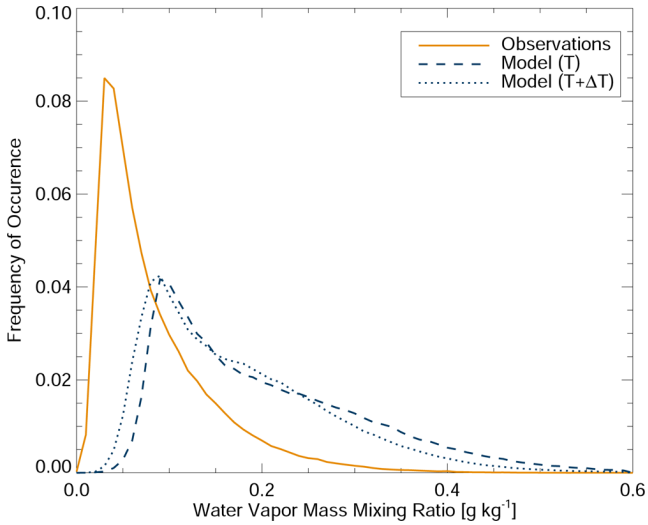

Figure 42: As in Figure 33, but adding the water vapor mass mixing ratio histogram computed by the model after AIRS temperatures are assimilated.

CHAPTER VI

CONCLUSIONS AND FUTURE WORK

This study has examined the relative roles of detrainment temperature, convective ice water content, ice cloud effective radius, and ambient relative humidity in regulating the efficiency of convective moistening in the tropical upper troposphere. The spatial and temporal limits of these interactions are investigated for both continental and maritime convection between 15°S and 15°N using observational data from the Tropical Rainfall Measuring Mission, Terra, and Aqua satellite missions together with simple model studies. The results help to characterize the distribution of upper tropospheric water vapor in the tropics and its relation to convective vertical and microphysical structure.

The general relationships between convection and downstream water vapor are consistent with previous results. Moistening from convection is maximized at 6-12 hours lag time from the convective event, and appears to be largely depleted beyond about 24-36 hours lag time. Detrainment from altitudes nearer to 200 hPa reaches a relatively steady state more quickly (∼18 hours) than does detrainment from altitudes nearer to 300 hPa (∼30 hours). In addition, moistening by convection appears to be at a minimum in boreal summer and maximum in austral summer, particularly for lower detrainment altitudes; however, there is essentially no noticable seasonal cycle in the middle of the 300-200 hPa range, and this relationship is reversed for detrainment from high altitudes (moister for boreal summer than austral summer).

The influence of ice water content (IWC) on downstream water vapor mixing ratios is minimal near the convective source, but does appear to grow with lag time from convection. This result is consistent with an exponential decay model of IWC along trajectory paths originating with convection where the e-folding time is assumed to be constant. This assumption is analogous to assuming consistent particle size distributions across the range of IWC observable by the TRMM Precipitation Radar.

The dehydration rate along trajectories generally grows with detrainment IWC, a relationship that is observed to be consistent throughout all four seasons. This results from the microscale nature of condensation, which generally takes place at the interface of an existing hydrometeor. In particular, ice and mixed phase particles lower the saturation vapor pressure in their immediate environment, allowing condensation to take place at observed relative humidities significantly below 100%. The saturation vapor pressure at the droplet surface is inversely related to the droplet radius (*Emanuel*, 1994). A larger IWC corresponds to either larger number densities of ice particles or larger ice particles, and perhaps both. Larger ice particle number densities would provide more surfaces for water vapor to condense upon, effectively spreading the lowered saturation vapor pressure through a broader volume; larger ice particles would further lower saturation vapor pressure at each individual surface. Thus, either interpretation of IWC supports the observed relationship between IWC and dehydration rate.

Ice effective radius appears to play a more influential role in determining downstream water vapor than ice water content; however, this influence does not appear to be monotonic in effective radius. In particular, the trajectories downstream are most humid for middle values of ice effective radius ($\sim$22-32 μm), and driest for large values ($\geq 40\mu$m). There is some evidence that stronger moistening occurs associated with the lowest observed values of effective radius ($\sim$8-15 μm), but the general trend suggests that water vapor downstream from small ice particles is lower than from medium, but higher than from large. These relationships are mirrored for dehydration rate. The lowest dehydration rates are found in the medium range of effective radius, the highest rates are found in the large range, and the rates in the small range fall between the two.

These results can be put into some context by considering the spectrum of MODIS daily mean effective radii as a spectrum of particle size distributions (PSDs). PSDs that are skewed toward large ice will be more efficient at both dehydrating the surrounding air and precipitating out. PSDs that are skewed toward small ice may have insufficient water content to maintain moisture, or may also promote condensation by virtue of large number densities. PSDs that fall in the middle range may have sufficient water content to

significantly affect water vapor along the trajectory, and may stay aloft for long enough to do so. The MODIS spectral algorithm for cloud retrievals does appear to have some problems retrieving smaller ice particle effective radii, particularly in land fields of view (*Brèon et al.*, 2002), a limitation that may affect these results. Ice particles are more likely to be small over land due to pollution from anthropogenic cloud condensation nuclei, and small ice is expected to moisten the UT most effectively (e.g., *Sherwood*, 2002; *Del Genio et al.*, 2005). If the retrieved effective radius is significantly too large over land but not over ocean, then the interpretation of these results may need to be revised. We note, however, that at the time of this writing, no demonstrably better source exists for ice effective radius in global tropical deep convective clouds. Further, the discrepancies noted by *Brèon et al.* (2002) were in lower (water) stratocumulus, where the spectral signal may be more difficult to distinguish from the land surface, and the statistics of the droplet size distribution were found to be well characterized by MODIS.

An analysis of twelve tropical regions chosen to encompass disparate convective regimes reveals slight positive linear correlations between convective frequency and mean water vapor downstream, and between mean IWC and mean water vapor downstream. These relationships are observed to have some seasonal variability; in particular, the correlation for convective frequency is lowest during boreal summer, when the contributions from intense continental convection are at their apex. It is emphasized that the slope for each of these correlations is small, indicating that these variables do not exert a first-order impact on water vapor. No robust correlation is observed for mean ice effective radius at all, which might be expected due to the apparently nonlinear relationship between ice effective radius and downstream water vapor.

Ambient relative humidity with respect to ice (RH_i) along the trajectory path is found to exert a regulatory role on the change in water vapor mixing ratio, both in absolute and in normalized terms. In particular, the change in water vapor mass mixing ratio (Δw) is inversely related to RH_i: net moistening dominates at small RH_i while net drying dominates at large RH_i. More specifically, strong hydration ($\Delta w \geq +0.1$ g kg^{-1}) is found to occur only for ambient $RH_i \leq 70\%$, while strong dehydration ($\Delta w \leq -0.1$ g kg^{-1}) only occurs at

$RH_i \geq 50\%$. Relative increases of nearly 300% are observed at low values of RH_i, suggesting that changes in the frequency or location of convection reaching to especially dry areas in the UT and LS could have a significant influence on the water vapor feedback.

This last result implies the potential importance of convection penetrating beyond the tropopause. Relative humidities are typically quite low in the lower stratosphere (cf. *Kley et al.*, 1982; *Holton et al.*, 1995), theoretically allowing ice to sublimate and moisten the ambient air (e.g., *Vömel et al.*, 1995). In the tropics, however, this effect may be canceled out or even overcome by the negative buoyancy prevalent in the lower stratosphere, which tends to accelerate particles downward across the tropopause quickly (*Knollenberg et al.*, 1993). *Danielsen* (1982) and *Danielsen* (1993) indicate that tropical deep convection actually dehydrates the lower stratosphere by promoting condensation of ambient vapor and sedimentation of the resulting ice. *Dessler and Sherwood* (2004) conclude that the RH_i-Δw relationship is likely to be more influential in the extratropical lower stratosphere, a contention that is supported by the results of *Fu et al.* (2006).

The limits of the RH_i-Δw relationship in time and space are found to be about 36 hours and 600 km, consistent with the lifetimes and advection scales of tropical detrainment cirrus (*Luo and Rossow*, 2004). Further, this relationship is characterized for the global tropics regardless of when and where convection has taken place. The results reflect the balance between convective moistening and subsidence drying in the tropical UT, and are consistent with a subsidence rate of about 10 hPa day^{-1}.

In this context it appears that the probability densities derived in this study can qualitatively characterize the distribution of tropical humidity. Current climate models have difficulty simulating the effects of convectively detrained condensate (*Del Genio et al.*, 2005); this method could provide a useful observational constraint to help address this issue. In particular, the comparison of observational and model simulated PDFs of water vapor change associated with convective detrainment as a function of convective vertical and microphysical structure should help to identify the key sources of error and constrain the convective and cloud parameters. Further characterization of the joint probability densities, how they evolve, and how they vary in time and space is necessary as a next step; however,

the method shows promise and the data appear to be well-characterized (*Gettelman et al.*, 2004; *Hagan et al.*, 2004; *Fetzer et al.*, 2005).

An advection-condensation model is defined, in which a saturated parcel detraining from convection is advected through the large-scale circulation and temperature field using a Lagrangian trajectory model. If the temperature reaches the dewpoint at any time and place along the trajectory integration, the water vapor content of the parcel is assumed to condense, the condensate is removed, and the humidity is reset to the new saturation mixing ratio. Previous studies have shown that the large-scale humidity distribution can be largely reproduced in this way without any explicit parameterization of convection or cloud microphysics (*Sherwood*, 1996b; *Salathè and Hartmann*, 1997; *Pierrehumbert and Roca*, 1998; *Dessler and Sherwood*, 2000, 2004).

Comparisons of our model with coincident AIRS observations of water vapor reveal that, while the model is able to capture the general horizontal distribution of UTH, it overestimates the observed humidity by about 100%. This bias is shown to persist at least through 48 hours removed from convection, and even appears to grow some. Essentially, this suggests that the model is missing a dehydration mechanism or mechanisms that have an impact approximately equal to that of the large-scale temperature field.

Observational and model probability densities for the expected water vapor based on detrainment ice water content and ice effective radius are compared, and a small amount of the discrepancy appears to be due to the exclusion of microphysical dehydration processes. In addition, we note a remarkable similarity between the qualitative shapes of the modeled and observed probability densities. As the model knows essentially nothing of ice, this result underscores the higher order nature of the relationship between these two ice parameters and the downstream water vapor content and further suggests that the primary source of the model bias is unlikely to be microphysical.

The model as originally formulated assumes that air condenses at 100% saturation; however, there are several reasons that this assumption may be physically unrealistic. First, condensation is a microscale process, and the trajectory is integrated using large-scale temperature fields. This means that condensation may be taking place at some saturated point

within the advected volume even though the volume itself is not at saturation. Second, the air that detrains from convection may be substantially subsaturated (*Tompkins and Emanuel*, 2000; *Pierrehumbert et al.*, 2006). Previous studies have accounted for these concerns by assuming a condensation threshold of 90% of saturation rather than 100% (*Sherwood*, 1996b; *Galewsky et al.*, 2005). Assuming a similar threshold for our model, and then assuming an even more restrictive threshold, indicates that the modeled humidity converges toward the observed humidity; however, in order to reproduce the observations we would have to apply a condensation threshold of about 50% of saturation, an assumption that would be physically unrealistic.

The role of the assumed temperature field has also been investigated. Temperatures simulated by reanalysis models have been shown to be too warm near the tropopause (*Randel et al.*, 2000; *Trenberth et al.*, 2001), an error that would lead to overestimates of water vapor mixing ratio in a model like ours. AIRS temperature observations are indeed found to be slightly cooler than those reported in the UKMO reanalyses, and we assimilate daily mean $1^\circ \times 1^\circ$ AIRS temperature wherever we are able. This is shown to have only a minimal effect, however, far less than is required to explain the discrepancy. Finally, convection is known to excite gravity waves that perturb its environment, including the temperature field (*Lane and Reeder*, 2001). These perturbations are of a scale too small to be resolved in the reanalysis. We therefore impose a randomly defined perturbation within confines consistent with a convectively generated gravity wave in the tropical UT on each trajectory. Again the model-observation discrepancy is lessened; again the effect is too small to explain the bias.

In fact, the total contribution of all of the possible dehydration mechanisms studied here does not appear to be sufficient to explain the discrepancy. An analysis of the time evolution of probability densities of downstream water vapor and detrainment temperature indicates that the discrepancy disproportionately affects trajectories detraining at higher temperatures (lower altitudes). Signs of such a mechanism have been observed consistently through all three of the analyses presented here. While the exact mechanism is undetermined, we have proposed a possible candidate.

Many studies of tropical convection have noted the existence of strong unsaturated downdrafts (e.g., *Squires*, 1958, and many others), as well as their potential import for dehydrating convective detrainment (e.g., *Tompkins and Emanuel*, 2000). These downdrafts are formed when falling precipitation melts or evaporates. Such processes require energy, and result in a net latent cooling. The cooling accelerates the air downward, through relatively warm, humid levels. Since the air in the downdraft typically contains much less water vapor than the air it passes through, it tends to remove water vapor from the ambient air as it continues its descent.

Such downdrafts are typically thought to be more prevalent at lower levels in the convective tower, and are not often considered to be an important dehydration mechanism between 300 hPa and 200 hPa. We are unable to show conclusively that this is the mechanism at work here, but we do find that the preponderance of evidence is consistent with such an explanation. In particular:

- *Petersen and Rutledge* (2001) reported that deep convection is observable by the TRMM PR to altitudes of 19 km, and showed that significant amounts of precipitation ice exist at levels above 12 km, particularly for convection occurring over continents. This means that precipitation ice exists at the necessary altitudes.

- The dehydrated air has typically been detrained closer to 300 hPa, the lower level of our analysis domain, allowing room for the anvil to precipitate and the downdraft to form. This is observed consistently among all three analyses.

- Anomalously humid air is seen in trajectories detraining near 200 hPa at lag times of 6-12 hours from convection, and is most prevalent during boreal summer when the occurrence of intense continental convection is at its apex. This peculiar moistening may be explained by the evaporation of precipitation from the anvil cloud overlaying this layer, which may in turn trigger an unsaturated downdraft.

- The smallest slope in the convective frequency-mean downstream water vapor regional linear regression is also observed during boreal summer. Moreover, this reduction in

slope appears to be largely due to lower than expected mean water vapor in the Congo, Equatorial Africa, and Central America regions, where intense continental-type convection would be expected.

- Significant differences are observed in the RH_i-Δw relationship between continental and oceanic convection; particularly, significant drying appears to be more prevalent in continental convection. This discrepancy is traced to fundamental differences in the typical detrainment profile, and appears to be almost entirely due to differences in the trajectories that correspond to detrainment levels below $\theta = 340$ K.

Taken in tandem, these items tend to support the contention that unsaturated downdrafts could produce the observed dehydration patterns that we are otherwise unable to explain. This issue requires future work, and we are currently considering the possibility of modeling the mechanism we suspect (unsaturated downdrafts), and comparing the simulated effect to the observations that lead us to this suspicion (very deep continental convection).

Beyond the role of unsaturated downdrafts, significant questions remain about how much of the lack of relationship between ice cloud parameters and downstream water vapor is determined by persistent uncertainties in IWC and ice cloud effective radius. These questions may be best addressed through the use of aircraft and satellite observations together in an analysis similar to this but more focused in scope. Aircraft measurements of particle size distributions, ice water contents, and other cloud parameters would help to evaluate the utility of ice products derived from MODIS and TRMM and more accurately assess the significance of these results. Furthermore, the Aura Microwave Limb Sounder (MLS) provides satellite observations of IWC (*Wu et al.*, 2006). These observations could be used to evaluate various functional algorithms for computing IWC from the TRMM PR, provided careful assessment of the matching mechanism is performed.

Continuous data collection for nearly two years by the Aura MLS provides tremendous potential for the extension and evolution of this study into the tropical tropopause layer and lower stratosphere (*Waters*, 2006). Water vapor in the lower stratosphere has recently been characterized by an unexplained trend that may (or may not) have reversed (*Rosenlof*

et al., 2001). The tropical tropopause layer refers to the transition zone between the upper troposphere and lower stratosphere and remains a relatively young area of study. The potential application of Aura MLS and the general ideas that formed the basis for this dissertation will be explored for these two regions. Two specifically oriented studies are well into the planning stages.

Finally, subtropical upper tropospheric water vapor is expected to exert a great deal of influence on the water vapor feedback, as some of the driest regions on the globe are located there (*Pierrehumbert*, 1998, 1999). In fact, halving the subtropical relative humidity is expected to lead to a 2.5 K cooling in the tropics, while doubling it would lead to a 3 K warming (*Pierrehumbert*, 1999). The AIRS instrument appears to be uniquely suited for diagnosing water vapor in the subtropical troposphere, as it provides water vapor profiles that are generally within 10% of radiosonde observations from the surface to 200 hPa at good vertical and horizontal resolutions. We will explore the potential for applying these and other methods to studies of subtropical water vapor using AIRS.

APPENDIX A

RADIATIVE PROPERTIES OF UPPER TROPOSPHERIC WATER VAPOR

Water vapor is radiatively active throughout the visible, infrared, and microwave portions of the spectrum, and its radiative characteristics are important in the atmospheric sciences for a number of reasons. This study is primarily concerned with three of these: first, water vapor absorption bands in the infrared comprise the bulk of the atmospheric greenhouse effect; second, the temperature dependence of water vapor saturation mixing ratio implies a positive feedback to radiative warming trends; third, water vapor absorption and emission serve as both a tool and an obstacle for satellite remote sensing of the Earth's atmosphere.

The radiative properties of water vapor are characterized by three vibrational modes, three rotational modes, and the water vapor continuum, which is comprised of residuals from distant lines and broadening due to molecular collisions in the atmosphere. The radiative signature of water vapor in the UT is dominated by two vibrational modes in the near infrared, a vibration-rotation transition centered at a wavelength of 6.3μm, pure rotational lines at wavelengths greater than 10 μm, and continuum absorption throughout the infrared and microwave spectrum.

The spectroscopy of the atmosphere is shown in Figure 43. The contribution of water vapor to the atmospheric greenhouse effect can be seen by comparing the bottom and top panels: water vapor is relatively translucent to incoming solar radiation (leftmost black-body curve in the top panel), but largely opaque to outgoing longwave radiation from the surface (rightmost black-body curve). Absorption due to the water vapor continuum can be observed in the atmospheric window near 10μm, where the absorptivity remains non-zero. The water vapor continuum results from the residuals of distant bands, primarily through pressure broadening due to molecular collisions, and represents the primary source

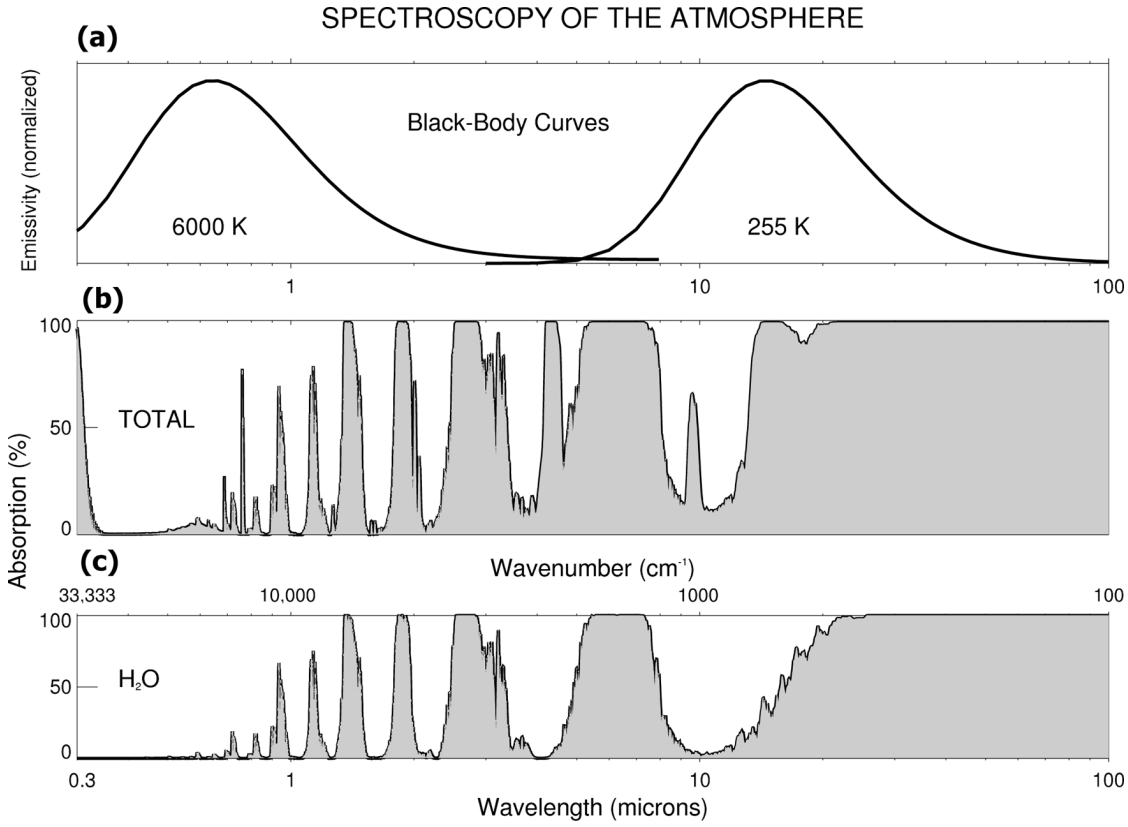

Figure 43: Spectroscopy of the atmosphere. Black-body curves in panel (a) correspond to incoming solar radiation (left) and outgoing terrestrial radiation (right). Absorption spectra are shown for (b) the total atmosphere and (c) water vapor. Courtesy of J. Bates, B. Soden, and R. Fu.

of uncertainty in atmospheric radiative transfer (*Held and Soden*, 2000).

The impact of upper tropospheric humidity on greenhouse warming in the atmosphere is shown via a Clough diagram in Figure 44. The tropical dry profile is chosen to be broadly representative of the subtropics, while the tropical wet profile (b) is typical of the deep tropics. The diagram is arranged to show the influence of water vapor on radiative cooling rate as a function of altitude and wavenumber. The units of this diagram are K d^{-1} cm^{-1}, such that a higher value means that more outgoing longwave radiation is trapped per unit increase in water vapor at that altitude and for that wavenumber. Upper tropospheric water vapor is shown to be most sensitive to radiation in the microwave portion of the spectrum (wavenumber $\leq$ 500 cm^{-1}) and in the 1500 cm^{-1} (6.7μm) range of the infrared portion of the spectrum.

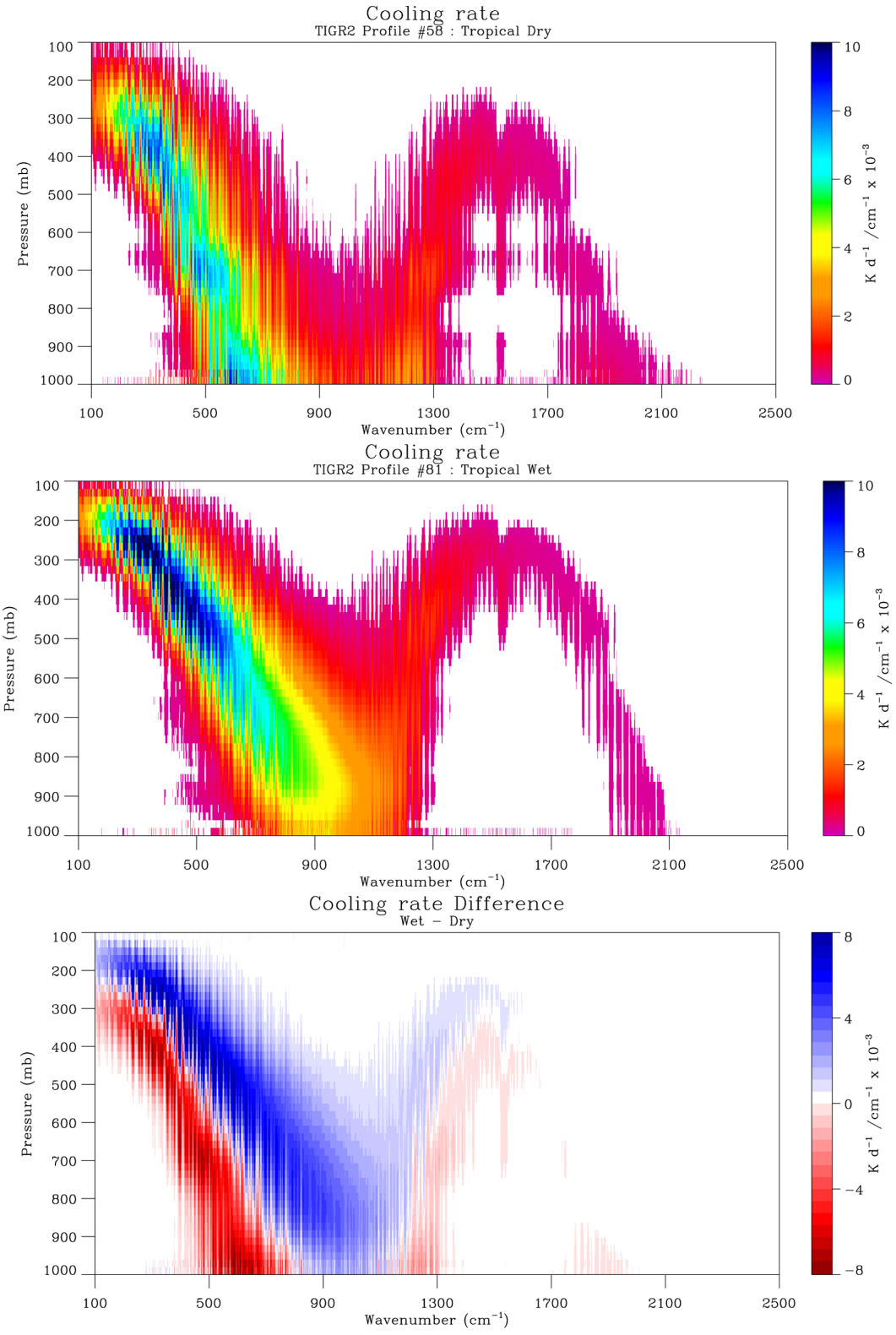

Figure 44: Clough diagrams for (a) tropical dry atmosphere; (b) tropical wet atmosphere; and (c) difference wet-dry. Courtesy of J. Bates, B. Soden, and R. Fu.

Both of these spectral ranges are used in the remote sensing of water vapor. For instance, most geostationary satellites and some polar orbiting satellites characterize upper tropospheric water vapor (500-150 hPa) using the 6.7μm absorption band (*Soden and Bretherton*, 1993), and several instruments have been developed to take advantage of water vapor's radiative signal (and the relative lack of ice signal) in the microwave (e.g., *Saunders et al.*, 1972; *Read et al.*, 2001). Generally speaking, the former technique is limited by a broad weighting function and essentially no vertical resolution, while the latter is limited by low horizontal resolution. The Atmospheric Infrared Sounder data used in this study synthesizes information from 66 individual water vapor channels in the infrared region and 3 channels in the microwave to obtain water vapor profiles at high resolution in the presence of clouds.

The temperature of the Earth is determined by the difference between the amount of incoming solar radiation absorbed by the surface and the amount of outgoing longwave radiation emitted by the surface. In the absence of any greenhouse effect, the Earth's surface temperature would be about 255 K, or -18°C. The bulk of this greenhouse effect is due to water vapor (*Warren and Thompson*, 1983). Furthermore, temperature sensitivity is strongest to changes in water vapor in the tropical UT *Shine and Sinha* (1991); *Spencer and Braswell* (1997). This relationship can also be observed in Figure 44, as the largest cooling rate sensitivity is observed for UTH at wavenumbers in the microwave portion of the spectrum, particularly for the tropical wet profile.

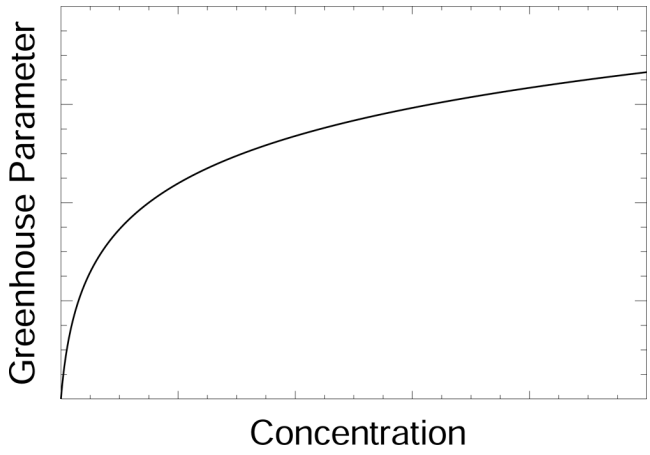

Figure 45: A schematic depiction of the logarithmic dependence of water vapor greenhouse parameter on water vapor concentration. For relationships derived using a line by line radiative transfer algorithm, see *Chou et al.* (1993)

Like most greenhouse gases, the greenhouse parameter of water vapor is approximately logarithmic in concentration (*Chou et al.*, 1993; *Pierrehumbert et al.*, 2006). The consequences of this relationship for UTH are apparent in the schematic diagram shown in Figure 45. At small ambient concentrations of water vapor, such as exist in the UT, small absolute changes in water vapor change the greenhouse parameter by a disproportionately large amount. The tendency of the greenhouse parameter to change relatively little with changes in water vapor amount at high ambient water vapor concentrations is often referred to as signal saturation.

APPENDIX B

VINCENTY'S FORMULAE

The notation in the following description of Vincenty's formulae follows that given in (*Vincenty*, 1975). A more complete explanation of the equations and the associated error can be found in that reference.

B.1 Direct Formula

The point on a sphere a certain distance s and azimuthal direction α_1 away from a given point P_1 is calculated by first computing

$$\tan \sigma_1 = \tan(U_1 / \cos \alpha_1), \tag{10}$$

$$\sin \alpha = \cos U_1 \sin \alpha, \tag{11}$$

$$A = 1 + \frac{u^2}{256}[64 + u^2(-12 + 5u^2)], \tag{12}$$

and

$$B = \frac{u^2}{512}[128 + u^2(-64 + 37u^2)]. \tag{13}$$

where U_1 is given by

$$\tan U_1 = (1 - f) \tan \phi_1, \tag{14}$$

f is the flattening factor given by $(a - b)/a$, σ_1 is the angular distance on the sphere from the equator to P_1, α is the directional azimuth at the equator, and

$$u^2 = \cos^2 \alpha (a^2 - b^2)/b^2 \tag{15}$$

where a and b are the major and minor semiaxes of the earth, 6378 km and 6357 km, respectively. Then the following set of equations are iterated until the change in angular distance σ between P_1 and P_2 is negligible:

$$2\sigma_m = 2\sigma_1 + \sigma \tag{16}$$

$$\Delta\sigma = B\sin\sigma[\cos 2\sigma_m + \frac{1}{4}B\cos\sigma(-1 + 2cos^2 2\sigma_m)] \tag{17}$$

$$\sigma = \frac{s}{bA} + \Delta\sigma. \tag{18}$$

where σ_m is the angular distance on the sphere from the equator to the midpoint of the line between P_1 and P_2. The computation is then finished by calculating

$$\gamma = \sqrt{\sin^2\alpha + (\sin U_1 \sin\sigma - \cos U_1 \cos\sigma \cos\alpha_1)^2} \tag{19}$$

$$\tan\phi_2 = \frac{\sin U_1 \cos\sigma + \cos U_1 \sin\sigma \cos\alpha_1}{(1-f)\gamma} \tag{20}$$

$$\tan\lambda = \frac{\sin\sigma \sin\alpha_1}{\cos U_1 \cos\sigma - \sin U_1 \sin\sigma \cos\alpha_1} \tag{21}$$

$$C = \frac{f}{16}\cos^2\alpha[4 + f(4 - 3\cos^2\alpha)] \tag{22}$$

$$\beta = \sin\sigma[\cos 2\sigma_m + C\cos\sigma(-1 + 2\cos^2 2\sigma_m)] \tag{23}$$

$$L = \lambda - (1-C)f\sin\alpha[\sigma + C\beta] \tag{24}$$

where λ is the difference in longitude on an auxiliary sphere, ϕ_2 is the latitude of P_2, and L is the difference in longitude between P_1 and P_2.

B.2 Inverse Method

The distance between two points on a sphere is determined using a first approximation of $\lambda = L$ and then iterating until the change in λ is negligible.

$$\sin^2 \sigma = (\cos U_2 \sin \lambda)^2 + (\cos U_1 \sin U_2 - \sin U_1 \cos U_2 \cos \lambda)^2 \tag{25}$$

$$\cos \sigma = \sin U_1 \sin U_2 + \cos U_1 \cos U_2 \cos \lambda \tag{26}$$

$$\tan \sigma = \sin \sigma / \cos \sigma \tag{27}$$

$$\sin \alpha = \cos U_1 \cos U_2 \sin \lambda / \sin \sigma \tag{28}$$

$$\cos 2\sigma_m = \cos \sigma - 2 \sin U_1 \sin U_2 / \cos^2 \alpha \tag{29}$$

where U_2 is calculated as in equation 2. The calculation is then finished with

$$s = bA(\sigma - \Delta\sigma) \tag{30}$$

where $\Delta\sigma$ is calculated from equations (10), (11), and (17).

REFERENCES

Alcala, C. M., and A. E. Dessler (2002), Observations of deep convection in the tropics using the Tropical Rainfall Measuring Mission (TRMM) precipitation radar, *J. Geophys. Res.*, *107*.

Aumann, H. H., M. T. Chahine, C. Gautier, M. D. Goldberg, E. Kalnay, L. M. McMillin, H. Revercomb, P. W. Rosenkranz, W. L. Smith, D. H. Staelin, L. L. Strow, and J. Susskind (2003), AIRS/AMSU/HSB on the Aqua mission: design, science objectives, data products, and processing systems, *IEEE Trans. Geosci. Remote Sensing*, *41*, 253–264.

Betts, A. K. (1990), Greenhouse warming and the tropical water budget, *Bull. Amer. Meteor. Soc.*, *71*, 1464–1465.

Boehm, M. T., and J. Verlinde (2000), Stratospheric influence on upper tropospheric tropical cirrus, *Geophys. Res. Lett.*, *27*, 3209–3212.

Bortz, S. E., M. J. Prather, J.-P. Cammas, V. Thouret, and H. Smit (2006), Ozone, water vapor and temperature in the upper tropical troposphere: Variations over a decade of MOZAIC measurements, *J. Geophys. Res.*, *111*, D05305, doi:10.1029/2005JD006512.

Brèon, F.-M., and M. Doutriaux-Boucher (2005), Comparison of cloud droplet radii measured from space, *IEEE Trans. Geosci. Remote Sensing*, *43*, 1796–1805.

Brèon, F.-M., D. Tanrè, and S. Generoso (2002), Aerosol effect on cloud droplet size monitored from satellite, *Science*, *295*, 834–838.

Brooks, H. E., C. A. Doswell III, and M. P. Kay (2003), Climatological estimates of local daily tornado probability for the United States, *Weather and Forecasting*, *18*, 626–640.

Chen, M., R. B. Rood, and W. G. Read (1999), Seasonal variations of upper tropospheric water vapor and high clouds observed from satellites, *J. Geophys. Res.*, *104*, 6193–6197.

Chou, M.-D., W. L. Ridgway, and M. M.-H. Yan (1993), One-parameter scaling and exponential-sum fitting for water vapor and CO_2 infrared transmission functions, *J. Atmos. Sci.*, *50*, 2294–2303.

Chung, E. S., B. J. Sohn, and V. Ramanathan (2004), Moistening processes in the upper troposphere by deep convection: A case study over the tropical Indian Ocean, *J. Meteorol. Soc. Jpn.*, *82*, 959–965.

Danielsen, E. F. (1982), A dehydration mechanism for the stratosphere, *Geophys. Res. Lett.*, *9*, 605–608.

Danielsen, E. F. (1993), In situ evidence of rapid, vertical, irreversible transport of lower tropospheric air into the lower stratosphere by convective cloud turrets and by larger-scale upwelling in tropical cyclones, *J. Geophys. Res.*, *98*, 8665–8681.

Del Genio, A. D., W. Kovari, M.-S. Yao, and J. Jonas (2005), Cumulus microphysics and climate sensitivity, *J. Clim.*, *18*, 2376–2386.

Dessler, A. E., and S. C. Sherwood (2000), Simulations of tropical upper tropospheric humidity, *J. Geophys. Res.*, *105*, 20,155–20,163.

Dessler, A. E., and S. C. Sherwood (2004), Effect of convection on the summertime extratropical lower stratosphere, *J. Geophys. Res.*, *109*, doi:10.1029/2004JD005,209.

Dopplick, T. G. (1972), Radiative heating of the global atmosphere, *J. Atmos. Sci.*, *29*, 1278–1294.

Emanuel, K. (1994), *Atmospheric Convection*, Oxford University Press, New York.

Fetzer, E., A. Eldering, E. F. Fishbein, T. Hearty, W. F. Irion, and B. Kahn (2005), Validation of AIRS/AMSU/HSB core products for data release version 4.0, *Tech. Rep. JPL D-31448*, Jet Propulsion Laboratory, Pasadena, CA.

Folkins, I., M. Loewenstein, J. Podolske, S. J. Oltmans, and M. Proffitt (1999), A barrier to vertical mixing at 14 km in the tropics: evidence from ozonesondes and aircraft measurements, *J. Geophys. Res.*, *104*, 22,095–22,102.

Folkins, I., K. K. Kelly, and E. M. Weinstock (2002), A simple explanation for the increase in relative humidity between 11 and 14 km in the tropics, *J. Geophys. Res.*, *107*, doi:10.1029/2002JD002,185.

Fu, R., Y. Hu, J. S. Wright, J. H. Jiang, R. E. Dickinson, M. Chen, M. Filipiak, W. G. Read, J. W. Waters, and D. L. Wu (2006), Convective transport over the tibetan plateau - a short-circuit of water vapor and polluted air to the global stratosphere, *Proc. Natl. Acad. Sci. USA*, *103*, 5664–5669, doi:10.1073/pnas.060158410.

Galewsky, J., A. Sobel, and I. Held (2005), Diagnosis of subtropical humidity dynamics using tracers of last simulation, *J. Atmos. Sci.*, *62*, 3353–3367.

Gettelman, A., W. J. Randel, F. Wu, and S. T. Massie (2002), Transport of water vapor in the tropical tropopause layer, *Geophys. Res. Lett.*, *29*, doi:10.1029/2001GL013818.

Gettelman, A., E. M. Weinstock, E. J. Fetzer, F. W. Irion, A. E. Eldering, E. C. Richard, K. H. Rosenlof, T. L. Thompson, J. V. Pittman, C. R. Webster, and R. L. Herman (2004), Validation of Aqua satellite data in the upper troposphere and lower stratosphere with in situ aircraft instruments, *Geophys. Res. Lett.*, *31*, L22107, doi:10.1029/2004GL020730.

Hagan, D. E., C. R. Webster, C. B. Farmer, R. D. May, R. L. Herman, E. M. Weinstock, L. E. Christensen, L. R. Lait, and P. A. Newman (2004), Validating AIRS upper atmosphere water vapor retrievals using aircraft and balloon in situ measurements, *Geophys. Res. Lett.*, *31*, L21103, doi:10.1029/2004GL020302.

Held, I., and B. J. Soden (2000), Water vapor feedback and global warming, *Annu. Rev. Energy Environ.*, *25*, 441–475.

Heymsfield, A. J., and J. L. Parrish (1978), A computational technique for increasing the effective sampling volume of the PMS 2-D particle size spectrometer, *J. Appl. Meteor.*, *17*, 1566–1572.

Heymsfield, A. J., A. Bansemer, C. Schmitt, C. Twohy, and M. R. Poellot (2004), Effective ice particle densities derived from aircraft data, *J. Atmos. Sci.*, *61*, 982–1003.

Heymsfield, A. J., Z. Wang, and S. Matrosov (2005), Improved radar ice water content retrieval algorithms using coincident microphysical and radar measurements, *J. Appl. Meteor.*, *44*, 1391–1412, doi:10.1175/JAM2282.1.

Heymsfield, A. J., A. Bansemer, S. L. Durden, R. L. Herman, and T. Bui (2006), Ice microphysics observations in hurricane Humberto: Comparison with non-hurricane-generated ice cloud layers, *J. Atmos. Sci.*, *63*, 288–308, doi:10.1175/JAS3603.1.

Heymsfield, G. M., B. Geerts, and L. Tian (2003), TRMM precipitation radar reflectivity profiles compared to high-resolution airborne and ground-based measurements, *J. Appl. Meteor.*, *42*, 769–774.

Highwood, E. J., and B. J. Hoskins (1998), The tropical tropopause, *Q. J. R. Meteorol. Soc.*, *124*, 1579–1604.

Holton, J. R., P. H. Haynes, M. E. McIntyre, A. R. Douglass, R. B. Rood, and L. Pfister (1995), Stratosphere-to-troposphere exchange, *Rev. Geophys.*, *33*, 403–439.

Hoyle, C. R., B. P. Luo, and T. Peter (2005), The origin of high ice crystal number densities in cirrus clouds, *J. Atmos. Sci.*, *62*, 2568–2579.

Jensen, E. J., and L. Pfister (2004), Transport and freeze-drying in the tropical tropopause layer, *J. Geophys. Res.*, *109*, D02207, doi:10.1029/2003JD004022.

Jordan, C. (1958), Mean soundings for the West Indies area, *J. Meteor.*, *15*, 52–53.

Kaufman, Y. J., and T. Nakajima (1993), Effect of Amazon smoke on cloud microphysics and albedo-analysis from satellite imagery, *J. Appl. Meteor.*, *32*, 729–744, doi: 10.1175/1520-0450(1993)032¡0729:EOASOC¿2.0.CO;2.

King, M. D., W. P. Menzel, Y. J. Kaufman, D. Tanré, B.-C. Gao, S. Platnick, S. A. Ackerman, L. A. Remer, R. Pincus, and P. A. Hubanks (2003), Cloud and aerosol properties, precipitable water, and profiles of temperature and water vapor from MODIS, *IEEE Trans. Geosci. Remote Sensing*, *41*, doi:10.1109/TGRS.2002.808226.

Kley, D., A. L. Schmeltekopf, K. Kelly, R. H. Winkler, T. L. Thompson, and M. McFarland (1982), Transport of water vapor through the tropical tropopause, *Geophys. Res. Lett.*, *9*, 617–620.

Knollenberg, R. G., K. Kelly, and J. C. Wilson (1993), Measurements of high number densities of ice crystals in the tops of tropical cumulonimbus, *J. Geophys. Res.*, *98*, 8639–8664.

Kummerow, C., W. Barnes, T. Kozu, J. Shuie, and J. Simpson (1998), The Tropical Rainfall Measuring Mission (TRMM) sensor package, *J. Atmos. Oceanic Technol.*, *15*, 809–817.

Kummerow, C., J. Simpson, O. Thiele, W. Barnes, A. T. C. Chang, E. Stocker, R. F. Adler, A. Hou, R. Kakar, F. Wentz, P. Ashcroft, T. Kozu, Y. Hong, K. Okamoto, T. Iguchi, H. Kuroiwa, E. Im, Z. Haddad, G. Huffman, B. Ferrier, W. S. Olson, E. Zipser, E. A. Smith, T. T. Wilheit, G. North, T. Krishnamurthi, and K. Nakamura (2000), The status of the Tropical Rainfall Measuring Mission (TRMM) after two years in orbit, *J. Appl. Meteor.*, *39*, 1965–1982.

Lane, T. P., and M. J. Reeder (2001), Convectively generated gravity waves and their effect on the cloud environment, *J. Atmos. Sci.*, *58*, 2427–2440.

Lindzen, R. S. (1990), Some coolness concerning global warming, *Bull. Am. Meteorol. Soc.*, *71*, 288–299.

Lindzen, R. S., M.-D. Chou, and A. Y. Hou (2001), Does the earth have an adaptive infrared iris?, *Bull. Am. Meteorol. Soc.*, *82*, 417–432.

Luo, Z., and W. B. Rossow (2004), Characterizing tropical cirrus life cycle, evolution and interaction with upper-tropospheric water vapor using Lagrangian trajectory analysis of satellite observations, *J. Clim.*, *17*, 4541–4563.

Manabe, S., and R. T. Wetherald (1967), Thermal equilibrium of the atmosphere with a given distribution of relative humidity, *J. Atmos. Sci.*, *24*, 241–259.

Mapes, B. E. (1993), Gregarious tropical convection, *J. Atmos. Sci.*, *50*, 2026–2037.

Mapes, B. E. (2001), Water's two height scales: The moist adiabat and the radiative troposphere, *Q. J. R. Meteorol. Soc.*, *127*, 2353–2366, doi:10.1256/smsqj.57707.

McCormack, J. P., R. Fu, and W. G. Read (2000), The influence of convective outflow on mixing ratios in the tropical upper troposphere: and analysis based on UARS MLS measurements, *J. Atmos. Sci.*, *24*, 241–259.

Minschwaner, K., and A. E. Dessler (2004), Water vapor feedback in the tropical upper troposphere: model results and observations, *J. Clim.*, *17*, 1272–1282.

Moller, F. (1963), On the influence of changes in CO_2 concentration in air on the radiation balance of Earth's surface and on climate, *J. Geophys. Res.*, *68*, 3877–3886.

Morris, G. A., J. E. Rosenfield, M. R. Schoeberl, and C. H. Jackman (2003), Potential impact of subsonic and supersonic aircraft exhaust on water vapor in the lower stratosphere assessed via a trajectory model, *J. Geophys. Res.*, *108*, doi:10.1029/2002JD002,614.

Nakajima, T., M. D. King, J. D. Spinhirne, and L. F. Radke (1991), Determination of the optical thickness and effective particle radius of clouds from reflected solar radiation measurements. Part II: Marine stratocumulus observations, *J. Atmos. Sci.*, *48*, 728–751, doi:10.1175/1520-0469(1991)048¡0728:DOTOTA¿2.0.CO;2.

Petersen, W. A., and S. A. Rutledge (2001), Regional variability in tropical convection: Observations from TRMM, *J. Clim.*, *14*, 3566–3586.

Pierrehumbert, R. T. (1998), Lateral mixing as a source of subtropical water vapor, *Geophys. Res. Lett.*, *25*, 151–154.

Pierrehumbert, R. T. (1999), Subtropical water vapor as a mediator of rapid global climate change, in *Mechanisms of Global Change at Millenial Time Scales*, edited by P. U. Clark, R. S. Webb, and L. D. Keigwin, American Geophysical Union, Washington, D. C.

Pierrehumbert, R. T., and R. Roca (1998), Evidence for control of Atlantic subtropical humidity by large scale advection, *Geophys. Res. Lett.*, *25*, 4537–4540.

Pierrehumbert, R. T., and H. Yang (1993), Global chaotic mixing on isentropic surfaces, *J. Atmos. Sci.*, *50*, 2462–2480.

Pierrehumbert, R. T., H. Brogniez, and R. Roca (2006), On the relative humidity of the Earth's atmosphere, in *The Global Circulation of the Earth's Atmosphere*, edited by T. Schneider and A. Sobel, Princeton Univ. Press.

Platnick, S., M. D. King, S. A. Ackerman, W. P. Menzel, B. A. Baum, J. C. Riédi, and R. A. Frey (2003), The MODIS cloud products: Algorithms and examples from Terra, *IEEE Trans. Geosci. Remote Sensing*, *41*, doi:10.1109/TGRS.2002.808,301.

Price, C. (2000), Evidence for a link between global lightning activity and upper tropospheric water vapour, *Nature*, *406*, 290–293.

Ramanathan, V., and W. Collins (1991), Thermodynamic regulation of ocean warming by cirrus clouds deduced from observations of the 1987 El Niño, *Nature*, *351*, 27–32.

Randel, W. J., F. Wu, and D. J. Gaffen (2000), Interannual variability of the tropical tropopause derived from radiosonde data and NCEP reanalyses, *J. Geophys. Res.*, *105*, 15,509–15,523.

Rawlins, F., and J. S. Foot (1990), Remotely sensed measurements of stratocumulus properties during FIRE using the C130 aircraft multi-channel radiometer, *J. Atmos. Sci.*, *47*, 2488–2504, doi:10.1029/1520-0469(1990)047¡2488:RSMOSP¿2.0.CO;2.

Read, W. G., J. W. Waters, D. L. Wu, E. M. Stone, Z. Shippony, A. C. Smedley, C. C. Smallcomb, S. Oltmans, D. Kley, H. G. J. Smit, J. L. Mergenthaler, and M. K. Karki (2001), UARS microwave limb sounder upper-troposphere humidity measurement: method and validation, *J. Geophys. Res.*, *106*, 32,207–32,258.

Reid, J. S., P. V. Hobbs, A. L. Rangno, and D. A. Hegg (1999), Relationships between cloud droplet effective radius, liquid water content, and droplet concentration for warm clouds in Brazil embedded in biomass smoke, *J. Geophys. Res.*, *104*, 6145–6154, doi: 10.1029/1998JD200119.

Riehl, H. (1979), *Climate and Weather in the Tropics*, 611 pp., Academic Press, London.

Rosenfield, J. E., P. A. Newman, and M. R. Schoeberl (1994), Computations of diabatic descent in the stratospheric polar vortex, *J. Geophys. Res.*, *99*, 16,677–16,689.

Rosenlof, K. H., S. J. Oltmans, D. Kley, J. M. Russell III, E.-W. Chiou, W. P. Chu, D. G. Johnson, K. K. Kelly, H. A. Michelsen, G. E. Nedoluha, E. E. Remsberg, G. C. Toon, and M. P. McCormick (2001), Stratospheric water vapor increases over the past half-century, *Geophys. Res. Lett.*, *28*, 1195–1198.

Salathè, E. P., and D. L. Hartmann (1997), A trajectory analysis of tropical upper-tropospheric moisture and convection, *J. Clim.*, *10*, 2533–2547.

Sassi, F., M. Salby, and W. G. Read (2001), Relationship between upper-tropospheric humidity and deep convection, *J. Geophys. Res.*, *106*, 17,133–17,146.

Saunders, R. W., T. J. Hewison, S. J. String, and N. C. Atkinson (1972), The radiometric characterization of AMSU-B, *IEEE Trans. Geosci. Remote Sensing*, *29*, 1413–1422.

Schneider, S. H. (1972), Cloudiness as a global climate feedback mechanism: the effects on the radiation balance and surface temperature of variations in cloudiness, *J. Atmos. Sci.*, *29*, 1413–1422.

Schoeberl, M. R., and G. A. Morris (2000), A Langrangian simulation of supersonic and subsonic aircraft exhaust emissions, *J. Geophys. Res.*, *105*, 11,833–11,839.

Schoeberl, M. R., and L. Sparling (1995), Trajectory modeling, in *Diagnostic Tools in Atmospheric Physics, vol. 124, Proceedings of the International School of Physics Enrico Fermi*, edited by G. Fiocco and G. Visconti, pp. 289–306, IOS Press, Amsterdam.

Selkirk, H. B. (1993), The tropopause cold trap in the Australian monsoon during STEP AMEX 1987, *J. Geophys. Res.*, *98*, 8591–9610.

Sherwood, S. (2002), A microphysical connection among biomass burning, cumulus clouds, and stratospheric moisture, *Science*, *295*, 1272–1275.

Sherwood, S. C. (1996a), Maintenance of the free-tropospheric tropical water vapor distribution. part i: Clear regime budget, *J. Clim.*, *9*, 2903–2918.

Sherwood, S. C. (1996b), Maintenance of the free-tropospheric tropical water vapor distribution. part ii: Simulation by large-scale advection, *J. Clim.*, *9*, 2919–2934.

Sherwood, S. C. (1999), On moistening of the tropical troposphere by cirrus clouds, *J. Geophys. Res.*, *104*, 11,949–11,960.

Sherwood, S. C., and A. E. Dessler (2000), On the control of stratospheric humidity, *Geophys. Res. Lett.*, *27*, 2513–2516.

Shine, K. P., and A. Sinha (1991), Sensitivity of the Earth's climate to height-dependent changes in the water vapour mixing ratio, *Nature*, *354*, 382–384, doi:10.1038/354382a0.

Soden, B. J. (1998), Tracking upper tropospheric water vapor radiances: a satellite perspective, *J. Geophys. Res.*, *103*, 17,069–17,081.

Soden, B. J. (2000), The diurnal cycle of convection, clouds, and water vapor in the tropical upper troposphere, *Geophys. Res. Lett.*, *27*, 2173–2176.

Soden, B. J., and F. P. Bretherton (1993), Upper tropospheric relative humidity from the GOES 6.7 μm channel: Method and climatology for July 1987, *J. Geophys. Res.*, *98*, 16,669–16,688.

Soden, B. J., and R. Fu (1995), A seasonal analysis of deep convection, upper-tropospheric humidity, and the greenhouse effect, *J. Clim.*, *8*, 2333–2351.

Spencer, R. W., and W. D. Braswell (1997), How dry is the tropical free troposphere? implications for global warming theory, *Bull. Am. Meteor. Soc.*, *78*, 1097–1106.

Squires, P. (1958), Penetrative downdrafts in cumuli, *Tellus*, *10*, 382–389.

Stendel, M., and K. Arpe (1997), Evaluation of the hydrological cycle in reanalyses and observations, *Tech. Rep. Max Planck Institut für Meteorologie Rep. 228*, Max Planck Institut für Meteorologie, Berlin.

Stephens, G. L., and T. J. Greenwald (1990a), The Earth's radiation budget and its relation to atmospheric hydrology: 1. Observations of the clear sky greenhouse effect, *J. Geophys. Res.*, *96*, 15,311–15,324.

Stephens, G. L., and T. J. Greenwald (1990b), The Earth's radiation budget and its relation to atmospheric hydrology: 2. Observations of cloud effects, *J. Geophys. Res.*, *96*, 15,325–15,340.

Stocker, T. F., G. K. C. Clarke, H. Le Treut, R. S. Lindzen, V. P. Meleshko, R. K. Mugara, T. N. Palmer, R. T. Pierrehumbert, P. J. Sellers, K. E. Trenberth, and J. Willebrand (2001), Physical climate processes and feedbacks, in *Climate Change 2001: The Scientific Basis. Contribution of Working Group I to the Third Assessment Report of the Intergovernmental Panel on Climate Change*, edited by J. T. Houghton, Y. Ding, D. J. Griggs, M. Nogure, P. J. van der Linden, X. Dai, K. Maskell, and C. A. Johnson, pp. 419–470, Cambridge University Press, Cambridge, UK.

Sun, D.-Z., and R. S. Lindzen (1993), Distribution of tropical tropospheric water vapor, *J. Atmos. Sci.*, *50*, 1643–1660.

Swinbank, R., and A. O Niell (1994), A stratosphere-troposphere data assimilation system, *Mon. Weather Rev.*, *122*, 686–702.

Tian, B., B. J. Soden, and X. Wu (2004), Diurnal cycle of convection, clouds and water vapor in the tropical upper troposphere: satellites versus a general circulation model, *J. Geophys. Res.*, *109*, doi:10.1029/2003JD004,117.

Tompkins, A. M., and K. A. Emanuel (2000), The vertical resolution sensitivity of simulated equilibrium temperature and water vapor profiles, *Q. J. R. Meteorol. Soc.*, *126*, 1219–1237.

Trenberth, K. E., D. P. Stepaniak, and J. W. Hurrell (2001), Quality of reanalyses in the tropics, *J. Clim.*, *14*, 1499–1510.

Udelhofen, P. M., and D. L. Hartmann (1995), Influence of tropical cloud systems on the relative humidity in the upper troposphere, *J. Geophys. Res.*, *100*, 7423–7440.

Vincenty, T. (1975), Direct and inverse solutions of geodesics on the ellipsoid with application of nested equations, *Survey Review*, *176*, 88–93.

Vömel, H., S. J. Oltmans, D. Kley, and Crutzen (1995), New evidence for the stratospheric dehydration mechanism in the equatorial Pacific, *Geophys. Res. Lett.*, *22*, 3235–3238.

Warren, S. G., and S. L. Thompson (1983), The climatological minimum in tropical outgoing infrared radiation: Contributions of humidity and clouds, *Quart. J. Roy. Met. Soc.*, *109*, 169–185.

Waters, J. W. (2006), The Earth Observing System Microwave Limb Sounder (EOS MLS) on the Aura satellite, *IEEE Trans. Geosci. Remote Sensing*, *44*, 1075–1092.

Wilks, D. S. (2006), *Statistical Methods in the Atmospheric Sciences*, Elsevier Academic Press, Amsterdam.

Wu, D. L., J. H. Jiang, and C. P. Davis (2006), EOS MLS cloud ice measurements and cloudy-sky radiative transfer model, *IEEE Trans. Geosci. Remote Sensing*, *44*, 1166–1181.

Yang, H., and R. T. Pierrehumbert (1994), Production of dry air by isentropic mixing, *J. Atmos. Sci.*, *51*, 3437–3454.

Zhu, Y., R. E. Newell, and W. G. Read (2000), Factors controlling upper-troposphere water vapor, *J. Clim.*, *13*, 836–848.